

MICROSTRUCTURE AND MECHANICAL PROPERTIES OF ADDITIVELY
MANUFACTURED PARTS WITH STAIRCASE FEATURE

by

TAHMINA KEYA

Y. KEVIN CHOU, COMMITTEE CHAIR
ALEXEY N. VOLKOV, COMMITTEE CO-CHAIR
MARK L. WEAVER

A THESIS

Submitted in partial fulfillment of the requirements
for the degree of Master of Science in the
Department of Mechanical Engineering
in the Graduate School of
The University of Alabama

TUSCALOOSA, ALABAMA

2017

ABSTRACT

This thesis focuses on a part with staircase feature that is made of Inconel 718 and fabricated by SLM process. The objective of the study was to observe build height effect on the microstructure and mechanical properties of the part. Due to the nature of SLM, there is possibility of different microstructure and mechanical properties in different locations depending on the design of the part. The objective was to compare microstructure and mechanical properties from different location and four comparison groups were considered: 1. Effect of thermal cycle; 2. External and internal surfaces; 3. Build height effect and 4. Bottom surfaces. To achieve the goals of this research, standard metallurgical procedure has been performed to prepare samples. Etching was done to reveal the microstructure of SLM processed Inconel 718 parts. Young's modulus and hardness were measured using nanoindentation technique. FEM analysis was performed to simulate nanoindentation.

The conclusions drawn from this research are: 1. The microstructure of front and side surface of SLM processed Inconel 718 consists of arc shaped cut ends of melt pools with intermetallic phase at the border of the melt pool; 2. On top surface, melted tracks and scanning patterns can be observed and the average width of melted tracks is ~ 100-150 μm ; 3. The microstructure looks similar at different build height; 4. Microstructure on the top of a stair is more defined and organized than the internal surface; 5. The mechanical properties are highest at the bottom. OM images revealed slight difference in microstructure in terms of build height for this specific part, but mechanical properties seem to be vary noticeably. This is something to be kept in mind while designing or determining build orientation. External and internal surfaces of a

stair at the same height showed difference in both microstructure and mechanical properties. To minimize that effect and to make it more uniform, gradual elevation can be considered when suitable as far as design modification is concerned. Above all, this study reveals important information about the pattern of microstructure, thus heat transfer mechanism inside a part which is useful to understand the SLM process.

LIST OF ABBREVIATIONS AND SYMBOLS

AM	Additive Manufacturing
SLM	Selective Laser Melting
EBAM	Electron Beam Additive Manufacturing
ASTM	American Society for Testing and Materials
CAD	Computer Aided Design
STL	STereoLithography
CNC	Computer Numerical Control
UTS	Ultimate Strength
HIP	Hot Isostatic Pressing
SEM	Scanning Electron Microscopy
OM	Optical Microscopy
EBSD	Electron Backscatter Diffraction
XRD	X-Ray Powder Diffraction
E_A, η	Energy Density
U, v	Scanning Velocity
P	Laser Power
SP	Scan spacing
C_c	Machine Compliance
E	Young's modulus
E_r	Reduced Young's modulus
E_0	Young's modulus at 100% density

ν	Poisson's ratio
σ	Stress
σ_y	Yield strength
ϵ_p	Plastic strain
n	Strain hardening exponent
H	Hardness
A_r	Residual Area left by indenter
P	Porosity
a	Material Constant
n	Material Constant

ACKNOWLEDGEMENTS

I would like to thank my advisor, Dr. Y Kevin Chou for guiding me throughout this research.

I thank Dr. Alexey Volkov for being in the committee in spite of being busy and being patient about time constraint I had.

I'm grateful to Dr. Mark L. Weaver for being extremely supportive throughout my graduate studies. He allowed me to use his lab equipment from the very beginning and always helped me whenever I had any issues regarding nanoindentation or MTE labs. Last but not the least, he is serving as one the valuable members of the committee too.

A very special thanks goes to Dr. Paul Allison. At the end of my research when the Hysitron Triboindenter machine was no longer cooperating with me, Dr. Allison trained me in Agilent Technologies Nanoindenter G200 using his tip even during spring break. I also got to learn some theoretical details about nanoindentation from him. He as well as Dr. Luke Brewer held on their own experiments for the sake of my graduation. I thank both of them.

The CAF staffs Mr. Rich Martens, Mr. Johnny Goodwin, Mr. Robert Holler and Mr. Robert Fanning were very supportive in sample cutting and in SEM analysis.

I'm thankful to have some great group members like Dr. Bo Cheng, Mr. Xiaoqing Wang and Mr. Subin Shrestha who helped me from my 1st day in USA. All of them supported me in various ways and are no less than my family.

I thank all the staffs of department of Mechanical Engineering not only for their academic support, but also their personal help in my critical days. I also thank staffs from department of MTE too.

This research is supported by CFD Research Corporation (Huntsville, AL) through a NASA STTR project. Marshall Space Flight Center (Huntsville, AL) fabricated experimental samples.

Last but not the least, I thank my family, my friends and my fiancé Dr. Robert Mitchell Guice without whom I would never be where I am today.

CONTENTS

ABSTRACT	ii
LIST OF ABBREVIATIONS AND SYMBOLS	iv
ACKNOWLEDGEMENTS	vi
LIST OF TABLES	xii
LIST OF FIGURES	xiii
CHAPTER 1: INTRODUCTION	1
1.1 Additive Manufacturing	1
1.2 Selective Laser Melting	5
1.3 Ni alloys and Inconel 718	8
1.4 Motivations and Objectives	11
1.5 Uniqueness of the Present Work	12
1.6 Organization of the Thesis	13
CHAPTER 2: LITERATURE REVIEW	14
2.1 Introduction	14
2.2 Additive Manufacturing: Microstructure and Mechanical Properties	14
2.3 Selective Laser Melting: Microstructure and Mechanical Properties	18
2.4 Selective Laser Melting: Effect of Build Height	25
CHAPTER 3: EXPERIMENTAL DETAILS	27

3.1 Part Fabrication.....	27
3.2 Metallographic Sample Preparation.....	29
3.2.1 Cutting.....	29
3.2.2 Mounting.....	33
3.2.3 Polishing	33
3.2.4 Etching	34
3.3 Microstructure Study	35
3.3.1 Optical Microscopy.....	35
3.3.2 Scanning Electron Microscopy (SEM)	35
3.3.3 Motic Stereoscope.....	36
3.4 Nanindentation	37
3.4.1 Hysitron Triboindenter.....	37
3.4.2 Nanoindenter G200.....	40
3.5 Finite Element Analysis: Nanoindentation	41
CHAPTER 4: RESULTS AND DISCUSSION.....	46
4.1 Microstructure.....	46
4.1.1 Y plane: General Features.....	46
4.1.2 Y plane: Effect of Thermal Cycle	47
4.1.3 Y plane: External and Internal Surface	48
4.1.4 Y plane: Build Height Effect	50
4.1.5 Y plane: Bottom Surfaces	51
4.1.6 Z Plane: General Features	53
4.1.7 Z plane: Effect of Thermal Cycle	54

4.1.8 Z plane: External and Internal Surfaces.....	56
4.1.9 Z plane: Build Height Effect.....	59
4.1.10 Z plane: Bottom Surfaces.....	61
4.1.11 X plane.....	63
4.1.12 Summary: Comparison between X, Y and Z planes.....	67
4.2 Mechanical Properties.....	71
4.2.1 Nanoindentation test: General Discussion.....	71
4.2.2 Y plane: Effect of Thermal Cycle.....	75
4.2.3 Y Plane: External and Internal Surface.....	76
4.2.4 Y plane: Build Height Effect.....	78
4.2.5: Y plane: Bottom Surfaces.....	80
4.2.6 Z plane: Effect of Thermal Cycles.....	81
4.2.7 Z plane: External and Internal surface.....	83
4.2.8 Z plane: Build Height Effect.....	85
4.2.9 Z plane: Bottom surfaces.....	86
4.3 Finite Element Analysis of Nanoindentation.....	87
CHAPTER 5: CONCLUSIONS AND RECOMMENDATIONS.....	90
5.1 Conclusions.....	90
5.1.1 Microstructure: Y plane.....	90
5.1.2 Microstructure: Z plane.....	91
5.1.3 Mechanical Properties.....	92
5.2 Contribution of the Study.....	93
5.3 Recommendations and Future Work.....	94

5.3.1 Microstructure.....	94
5.3.2 Mechanical Properties.....	95
5.3.3 FEM Analysis	95
REFERENCES	96

LIST OF TABLES

Table 1.1: Classification of Additive Manufacturing technologies	5
Table 1.2: Chemical composition of Inconel 718.....	10
Table 3.1: Manufacturing parameters	29
Table 4.1: Example output of Triboindenter.....	73

LIST OF FIGURES

Figure 1.1: Generic steps of additive manufacturing process[6]	3
Figure 1.2: Examples of complex 3d printed objects[8].....	4
Figure 1.3: typical scanning pattern in metal PBF.....	7
Figure 2.1: OM images of cross section after etching	15
Figure 2.2: OM images of microstructure of (a)as built specimen; (b) HIPed specimen	17
Figure 2.3: Tensile curves and room temperature mechanical properties of IN718 superalloy processed by SLM in as-fabricated, SA treated and HSA treated states[14].....	20
Figure 2.4: Microstructure of as deposited Inconel 718	22
Figure 2.5: Young's Modulus for the SLM-processed Inconel 718 alloy	26
Figure 2.6. Nano-hardness of SLM-processed Inconel 718 alloy	26
Figure 3.1: (a) Concept Laser M2 Laser Cusing System, (b) Island scanning strategy[5].....	28
Figure 3.2: As deposited Inconel 718 part	28
Figure 3.3: Struers Discotom-100/-10 Cutting equipment	30
Figure 3.4: Allied High Tech TechCut 4™ Precision Low Speed Saw	30
Figure 3.5: Samples cut from Y plane	31
Figure 3.6: Samples cut from Z plane.....	32
Figure 3.7: Samples cut from X plane	32
Figure 3.8: Struers Metallurgical Mounting - Labopress 3[16].....	33
Figure 3.9: Allied High Tech MetPrep 3™ Grinder/Polisher.....	34

Figure 3.10: OM images of microstructure, (a) etched by HNO ₃ solution, (b) etched by Kalling's reagent.....	35
Figure 3.11: (a) JEOL 7000F machine for SEM; (b) operation panel	36
Figure 3.12: Motic Stereoscope	36
Figure 3.13 : (a) Schematic of nanoindentation and (b) Applied Load Function	37
Figure 3.14: (a)Hysitron Triboindenter; (b) Nanoindentation setup.....	38
Figure 3.15: Machine Compliance chart.....	39
Figure 3.16: Nano indenter G200	41
Figure 3.17: Berkovich tip in 2D analysis	42
Figure 3.18: Tip – sample assembly in 2D analysis	43
Figure 3.19: Meshing in 2D analysis	44
Figure 3.20: Force-displacement diagrams obtained from finite element analysis in literature...	45
Figure 4.1 Microstructure of Y plane	47
Figure 4.2: Effect of thermal cycle on Y plane.....	48
Figure 4.3: Comparison between Y plane microstructure from (a)external and (b)internal location of the part	49
Figure 4.4: Build height effect on Y plane	51
Figure 4.5 : Comparison between microstructures at the bottom of the part.....	52
Figure 4.6: Microstructure of Z plane; (a)X50, (b)X100, (c)X200 and (d)X500	54
Figure 4.7: Effect of thermal Cycle on Z plane	55
Figure 4.8: Microstructure of 2 specimens at (a) external and (b)internal surface.....	57
Figure 4.9: Comparison between SEM images taken at (a)external and (b)internal surfaces	58
Figure 4.10: Comparison of (a) external and (b) internal surfaces at 10X magnification	59
Figure 4.11: Microstructure of top surfaces at different build heights	60
Figure 4.12: Comparison between SEM images taken at different build heights	61
Figure 4.13: Comparison of microstructure at the bottom of the part	62

Figure 4.14: Comparison between Y and X plane at different magnifications	64
Figure 4.15: Comparison between X plane microstructure from different build heights	65
Figure 4.16: SEM images for X plane sample	66
Figure 4.17: Comparison between X, Y and Z plane	68
Figure 4.18: Force-displacement curves from Triboindenter	72
Figure 4.19: Force-displacement curves from Nanoindenter G200.....	73
Figure 4.20: Comparison between curves obtained from two nanoindenters.....	74
Figure 4.21: Comparison between Young’s moduli for different thermal cycles	75
Figure 4.22: Comparison between hardness for different thermal cycles	76
Figure 4.23: Comparison between Young’s moduli of external and internal surface	77
Figure 4.24: Comparison between hardness of external and internal surface	77
Figure 4.25: Comparison between Young’s modulus of external and internal surface.....	78
Figure 4.26: Comparison between hardness of external and internal surface	78
Figure 4.27: Comparison between Young’s moduli of different build heights	79
Figure 4.28: Comparison between hardness of different build heights	79
Figure 4.29: Comparison between Young’s moduli of bottom surfaces	81
Figure 4.30: Comparison between hardness of bottom surfaces	81
Figure 4.31: Effect of thermal cycle on Young’s modulus of Z plane	82
Figure 4.32: Effect of thermal cycles on hardness of Z plane	82
Figure 4.33: Comparison between Young’s modulus of external and internal surfaces	83
Figure 4.34: Comparison between hardness of external and internal surfaces.....	83
Figure 4.35: Comparison between Young’s modulus of external and internal surfaces	84
Figure 4.36: Comparison between hardness of external and internal surfaces.....	84
Figure 4.37: Comparison between Young’s modulus of top surfaces	85
Figure 4.38: Comparison between hardness of top surfaces.....	85

Figure 4.39: Comparison between Young's modulus of bottom surfaces.....	86
Figure 4.40: Comparison between hardness of bottom surfaces	86
Figure 4.41: 2D simulation results for $n=0.08$	87
Figure 4.42: FEM results and experimental results found for SLM Inconel718 [5]	88

CHAPTER 1: INTRODUCTION

1.1 Additive Manufacturing

Additive manufacturing can be defined as the process of manufacturing a part from its three dimensional computer aided design (3D CAD) model by adding layers of material without process planning. Although this definition looks very simple, but additive manufacturing covers a wide span of manufacturing processes these days that use same or similar concept of producing a part. The term ‘additive manufacturing’ is the formal name of the process ‘rapid prototyping’ which is also popularly known as ‘3D printing’. Rapid prototyping used to refer as the manufacturing process where a part is rapidly produced from its CAD design before releasing in the market. So, it is basically presenting the physical prototype of the actual product in its complete 3D form unlike giving an idea just about the design. Even though it started with ‘prototyping’, parts were actually produced in bulk using the additive approach, the ASTM has adopted the new term ‘additive manufacturing’ for this particular type of manufacturing which is now widely being used in general.

Unlike traditional manufacturing processes, additive manufacturing deals with the entire part as a whole instead of looking at details and separating it into segments since the entire part can be fabricated from its 3D model as one single body. But additive manufacturing emphasizes on making the design properly and understanding the manufacturing machine. This gives the freedom of design while making a very intricate object. A part is made by adding layer upon layer, so the layers have to have a finite thickness. Also, the final outcome depends on how the layers melt and bond with each other. This also determines how the post processing is going to

be. So, additive manufacturing has its own requirements and systems to get a perfectly fabricated part.

Additive manufacturing incorporates several steps of producing part and then it goes through the necessary post processing steps before releasing it as the final product. The generic steps of an AM process can be described as follows[6]:

1. Creating the 3D CAD model of the part
2. Converting the CAD file to an STL file which is used to calculate number of slices and other related parameters
3. Sending the STL file to the machine where some modifications can be made regarding the size of the part, orientation etc.
4. Setting up the manufacturing parameters like layer thickness, amount of energy, spot size etc.
5. Fabrication of the part which is automated and does not need any special supervision unless the material runs out or the power shuts off.
6. Removal of the part after the process is completed when the temperature is back to normal and no parts are moving
7. Post processing which involves cleaning up the part and removal of support structure
8. Final treatments before application like painting or assembling with other parts.

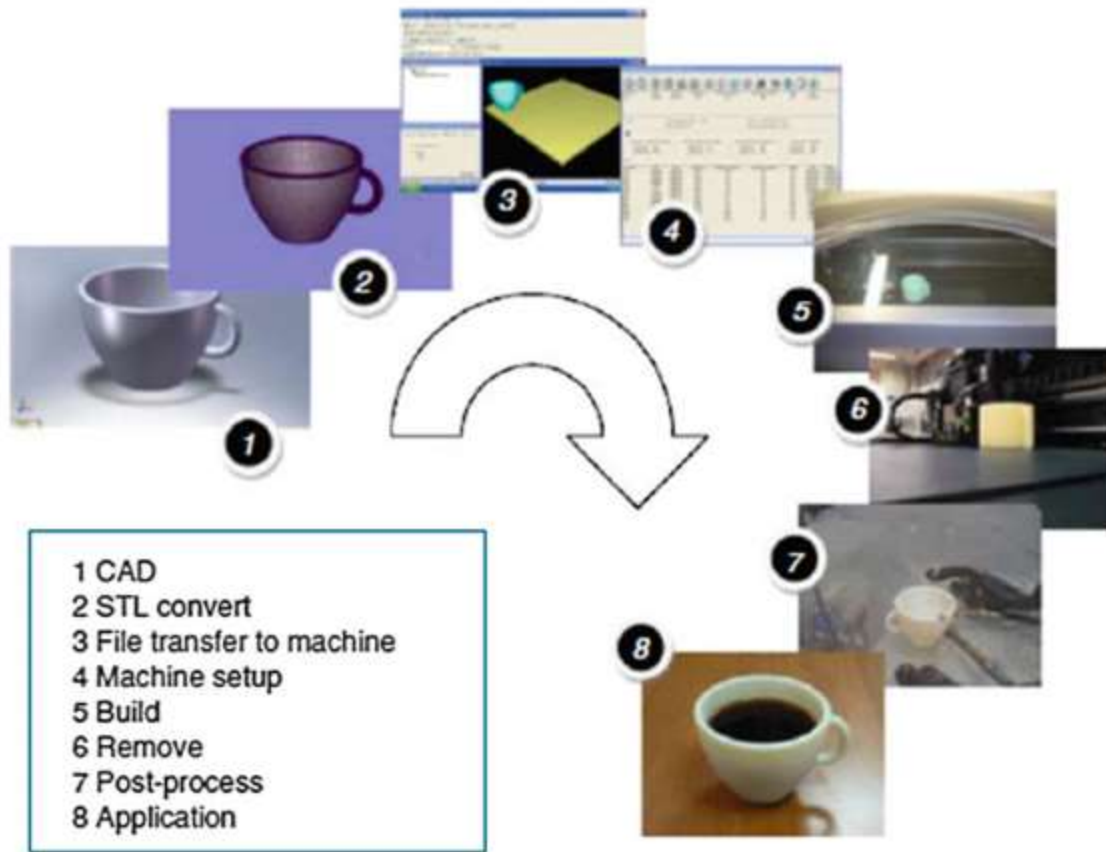


Figure 1.1: Generic steps of additive manufacturing process[6]

There are very strong reasons that justifies the fact that additive manufacturing can be considered as the beginning of third industrial revolution[7]. Some advantages of AM processes are:

1. As the name ‘rapid prototyping’ implies, the process is rapid. Time is a major concern when it comes to business and AM gives speed in manufacturing products. It does not require process management since it is usually done in one step. Even if the design is changed, it will only change some parameters in the process, but not number of steps. So, no matter how complex the design is, it will produce the part in just one single step.
2. Number of processes and resources gets significantly lower for additive manufacturing compared to casting and molding[6]. Several molds may need to be built to produce a single

part in molding. In addition to that, several fixtures may also need to be produced to use in CNC machining. In AM process, since the part is produced directly from its CAD model, no extra mold or fixture is necessary.

3. AM eliminates the requirement of skilled labor. It obviously require someone expert to operate and maintain the machine, but any manual crafting or operating while building the part are not necessary. In those steps in traditional manufacturing, the outcomes are prone to while in AM, it is more true to input.
4. It is possible to use AM technology in conjunction with traditional processes which will make the entire manufacturing process much cleaner and well managed.
5. Freedom of part design complexity is one of the biggest advantage of AM process. The more complex the design is, the more applicable this technology becomes. Because, traditional manufacturing techniques can become tedious and time consuming if the design becomes intricate. But in AM process, complexity of design hardly matters. In figure 1.2, some examples of complex objects are shown.

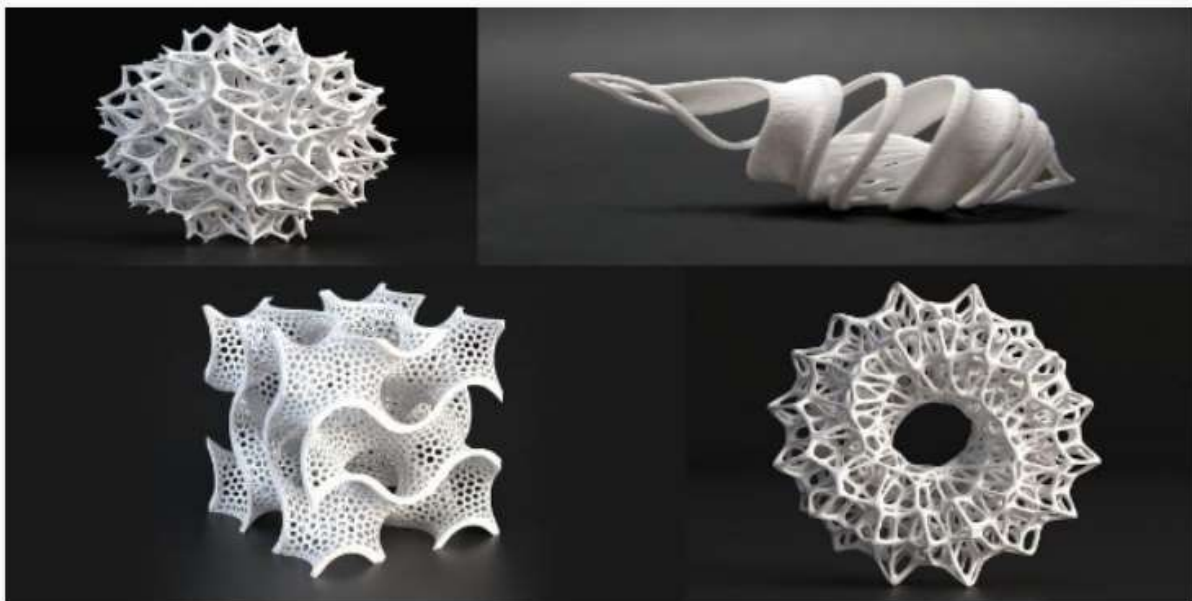


Figure 1.2: Examples of complex 3d printed objects[8]

Additive manufacturing covers a wide span of different processes which share same concept of adding layer upon layers of material from a 3D CAD model of the output object. The most accepted classification is illustrated below[6]:

Table 1.1: Classification of Additive Manufacturing technologies

Name of the process	Material	Technology
Vat photopolymerization	Liquid photopolymer	Energy is delivered selectively to produce part cross section
Powder bed fusion	Powder	Selectively melts powder using laser or electron beam
Material extrusion	Material filament	Extrudes the material from a nozzle that is scanned to produce part cross section
Material jetting	Liquid photopolymer	Similar to inkjet printer
Binder jetting	Binder into powder	Binder is printed into powder bed to produce part cross section
Sheet lamination	Sheet of material	Deposit of material at a time
Direct energy deposition	Powder, wire	Processes material by using energy through single deposition device

1.2 Selective Laser Melting

Among the seven types of classification discussed in section 1.1, selective laser melting falls in the category of powder bed fusion processes. The first commercial AM process was Selective Laser Sintering (SLS) which is a Powder Bed Fusion (PBF) process and was first developed the University of Texas at Austin. Selective laser melting is the type of powder bed

fusion process where laser is used to induce fusion between powder particles in a prescribed region of each layer. Selective laser melting, also known as laser cusing, melts powder layers beyond layer thickness. Also, the high energy of laser causes re-melting of previous layers which makes this process suitable for well bonded and high density metal parts for engineering applications.

The process parameters associated with SLM or any other PBF process can be categorized into 4 different types[6]:

1. Laser-related parameters: laser power, spot size, pulse duration, pulse frequency, etc.
2. Scan related parameters: scan speed, scan spacing, and scan pattern
3. Powder-related parameters: particle shape, size, and distribution, powder bed density, layer thickness, material properties, etc.
4. Temperature-related parameters: powder bed temperature, powder feeder temperature, temperature uniformity, etc.

In a PBF machine regardless of type of process, there are two modes of scanning-contour mode and fill mode. There are also two types of galvanometers for X-axis and Y-axis scanning. The contour mode is for shape definition and accuracy and fill mode is for filling the inside of the contour. For the fill mode, the scanning occurs along one axis incrementally and the other axis just moves back and forth in the entire scanning region. Figure 1.3 shows a typical scanning pattern[6]. Square based scanning pattern is used for metal powder.

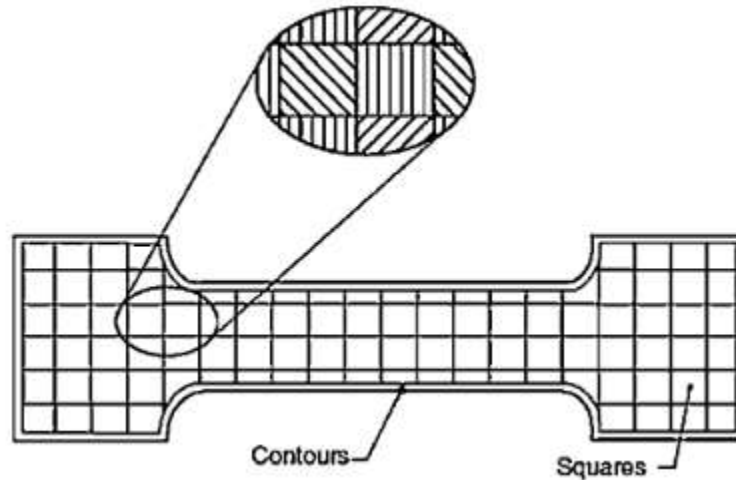


Figure 1.3: typical scanning pattern in metal PBF

Powder properties, laser properties and powder bed temperature individually and combined with each other play vital roles in the accuracy, surface finish and properties of the finished product. Finer powder particle is more desirable than coarse particle since it is more efficient in absorbing the energy than coarse ones. Powder bed temperature should be uniform and constant throughout the process to keep the outcome repetitive. The combination of laser power and powder bed temperature is also needed to be optimized to achieve desired design and mechanical properties. If both are high, it will produce dense parts, but will contribute to part growth, poor recyclability and difficulty in after cleaning. If both are low, the part will come out more accurate, but it will not be dense enough. High laser power and low powder bed temperature will result in shrinkage and residual stress which will cause curling of the part.

Melt pool characteristics highly depend on scanning parameters like speed and spacing. Low speed of scanning causes deeper and larger melt pool. Scanning space should be set the way so that it allows enough width for melt pool overlaps. Melt pool formation is a thermomechanical phenomenon which incorporates several physical, thermal and mechanical relations. It mainly depends on the total amount of energy absorbed by the powder bed. To correlate the density and strength of the finished product with the input parameters, the equation suggested based on a simplified model is[9],

$$E_A = \frac{P}{U \times SP} \quad (1.1)$$

Where E_A is the energy density, P is the laser power, U is the scanning velocity and SP scan spacing between two parallel scan lines.

Selective laser melting is very suitable for any material, especially metals as long as it can be welded. Support structures are often required for this type of manufacturing process, otherwise it causes residual stress build up and warping. This process provides flexibility in feedstock and shapes that makes it more acceptable for many industries[10].

1.3 Ni alloys and Inconel 718

Nickel is one of the most versatile elements and being used for many applications since the beginning of civilization[11]. It is used as a base of many alloys since its wide solubility range makes it easy to form alloys with several other metals like iron, chromium, copper etc. Nickel alloys have wide range of applications due to their following unique properties[12] :

- Nickel-chromium alloys are ideal to be used as electric resistance heating elements due to their high resistivity and heat resistance;
- Nickel-iron alloys have soft magnetic properties which make them suitable for electronic devices;
- Equiatomic nickel-titanium alloys have shape memory characteristics to be used as actuators, hydraulic connectors and eyeglass frames;
- Wrought nickel-beryllium-titanium alloys have high strength at elevated temperature and these are resistant to stress relaxation, so are suitable for electronic applications such as springs subjected to elevated temperatures;
- Cast nickel-beryllium-carbon alloys have high thermal conductivity and wear resistance, so these can be used for tooling in glass forming operations.

Some other applications of nickel and nickel alloys include[12] :

- Aircraft gas turbines

- Steam turbine power plants
- Medical applications
- Nuclear power systems
- Chemical and petrochemical industries

Sometimes nickel is used by itself in pure form or after adding very small amount of other metals for enhanced properties. Some of the important variants of nickel and nickel alloys are discussed here:

- Pure nickel: Nickel 200, Nickel 201, Nickel 205, Nickel 270 and 290, Permanickel Alloy 300, Duranickel Alloy 301 are some examples of commercial nickels where at least 94% nickel is used.
- Nickel-Copper alloys: These alloys have high corrosion resistance, thus making it useful for environment like sea water for nuclear submarines. Alloy 400 (66% Ni, 33% Cu), Alloy R-405, Alloy K-500 are some of the examples of nickel-copper alloys.
- Nickel-chromium-iron alloy: These are known for their high strength at elevated temperature. Some of most used alloys are Alloy 601(61% nickel), Alloy X750, Alloy 718 etc. Alloy 625, Alloy G3/G30 (Ni-22Cr-19Fe-7Mo-2Cu), Alloy C-22 (Ni-22Cr-6Fe-14Mo-4W), Alloy C-276 (17% Mo plus 3.7W), Alloy 690 (27% Cr addition) etc. offer higher corrosion resistance as well.

Inconel 718 is an austenitic nickel-chromium based superalloy. It is used for high temperature application due to its superior strength and corrosion resistance at elevated temperature environments. The chemical composition of Inconel 718 is given in table 1.2[13].

Table 1.2: Chemical composition of Inconel 718

Element	Percentage
Nickel (plus cobalt)	50.00-55.00
Chromium	17.00-21.00
Iron	Balance
Niobium (plus Tantalum)	4.75-5.50
Molybdenum	2.80-3.30
Titanium	0.65-1.15
Aluminium	0.20-0.80
Cobalt	1.00 max
Carbon	0.08 max.
Manganese	0.35 max.
Silicon	0.35 max.
Phosphorus	0.015 max.
Sulfur	0.015 max.
Boron	0.006 max.
Copper	0.30 max.

Superior mechanical properties of Inconel 718 allows it to be used in automotive, aerospace and biomedical industries. Most of the time it is used in extreme environments like in nuclear pressurized water reactors, space shuttles, Formula one exhaust systems etc. The engine combustion chamber of the SpaceX SuperDraco rocket engine was 3D printed and made of Inconel alloy using direct metal laser sintering process [27].

1.4 Motivations and Objectives

Inconel 718 is often chosen for Selective Laser Melting process to fabricate parts for aerospace, defense and biomedical industries. Since the applications are highly sensitive, it is very important to know and analyze the formation, structure and properties of SLM fabricated Inconel 718 parts and compare them with those manufactured in traditional approach. Several studies have been carried out in this field, but there are not a lot of information about the build height effect in SLM process. Due to the nature of this manufacturing technique, a complex thermomechanical phenomena takes place along the building direction while fabricating a part layer by layer. In our previous work[5], effect of build height on microstructure and mechanical properties of SLM fabricated Inconel 718 was investigated. The part used in that research was rectangular in geometry and heat treated to relief the stress. Part geometry can contribute significantly in local microstructure and mechanical properties. In this work, a part is considered which has staircase feature (figure 3.2). It has 3 major steps: at 3 mm, 30 mm and 60 mm height respectively. Each major step has 3 minor steps of 60 μm height from each other. Since the height of each step from the substrate at the bottom and number of layers needed to form each step is different, variation in microstructure and thus mechanical properties are expected. Also, the part did not go through stress relief, so the results are expected to be different than our previous work[5].

The objectives of this study are the following:

- Reveal microstructure in different locations of the part through necessary metallographic sample preparations
- Observe the microstructure using optical microscope (OM) and scanning electron microscope (SEM)

- Compare microstructures between locations
- Obtain mechanical properties namely Young's modulus and hardness using nanoindentation techniques
- Compare between locations and explain using microstructure results obtained

For choosing the locations in the part, 4 comparison groups have been considered:

1. 3 different build height at the same horizontal distance
2. External and internal surface which means top surface of a step and a surface 'inside' the part which is located at same build height with that top surface, respectively
3. Comparison between top surfaces of 3 major steps
4. Bottom surfaces under 3 major steps

1.5 Uniqueness of the Present Work

In this work, effect of build height in SLM fabricated Inconel 718 has been studied. In SLM process, the part has a solid substrate underneath which speeds up the cooling process near the areas at the bottom of the part. Also, as the building process approaches towards top, the number of heating and cooling cycle decreases. So, due to this complex thermos-mechanical phenomena, a variation in properties with increasing build height is expected. There are several works have been done microstructure and mechanical properties of SLM processed Inconel 718. A lot of them focused on effect of varying different parameters, effect of heat treatment etc. But there is hardly any work that presents any analysis on build height effect. A study has been done by our group on similar topic [5] which presented how the microstructure and mechanical properties change with increasing build height. The part used in that study had a simple rectangular geometry and also the residual stress was relieved by heat treatment. In this research, the part has staircase feature and no heat treatment have been done on it. The staircase feature

introduces some unique observations. The number of thermal cycles are different in 3 different steps. So the bottom surfaces of each step go through different number of re-melting and solidification cycles. Also, the surface inside the higher surface which is at the same height with a lower surface has different structure, thus properties than that lower surface. No work has been reported before that emphasizes on staircase feature or the effect of having different geometry. So this work is an approach to put the light on this matter and add some useful observations that may help with future research.

1.6 Organization of the Thesis

The thesis consists of five chapters. Chapter 1 discussed about general idea and background of Additive Manufacturing, its classification, Selective Laser melting process, Nickel alloys and some examples, Inconel 718 and its composition and uses. Literature reviews on additive manufacturing process, Selective Laser Melting process, microstructure and mechanical properties of SLM fabricated parts and specifically Inconel 719 parts has been presented in Chapter 2. Chapter 3 focuses on experimental details such as the entire procedure of preparing the samples right from cutting to polishing, revealing microstructure using etching with different solutions, observing the microstructure using OM and SEM and nanoindentation technique to obtain mechanical properties. Brief description of each equipment used have also been added in this chapter. Chapter 4 discusses the results and discussion. The general description and comparison between microstructure and mechanical properties are presented in this chapter. Finally chapter 5 discusses on conclusion drawn out of the experimental results and also suggests some improvement options and future work recommendations.

CHAPTER 2: LITERATURE REVIEW

2.1 Introduction

For past two decades, additive manufacturing is emerging as an alternative to traditional manufacturing technique. To improve it and get desired characteristics, numerous works have been done on various aspects of additive manufacturing processes. Researchers studied about general features of additive manufacturing processes, effects of varying different process parameters, effect of powder properties and so on. In this chapter, selected literatures on relevant topics have been discussed such as various aspects of SLM process, effect of different process parameters on microstructure and mechanical properties and finally effect of build height.

2.2 Additive Manufacturing: Microstructure and Mechanical Properties

As discussed in chapter 1, there are several types of additive manufacturing process and numerous research works have been done on each of them. In this section, few of those works will be discussed other than SLM and in section 2.3, SLM will be the main focus. Due to superior performance in extreme conditions, Ti-6Al-4V and Inconel 718 have always been a preference for certain industries and thus two of the most used materials in metal AM. So, extensive research works have been done on these materials. Other than the popular classes of metal AM- EBAM and SLM, there are couple other processes like shaped metal deposition (SMD) which utilizes tungsten inert gas welding. SMD process is suitable for expensive materials like Ti64. Baufeld et. al. [28] reported a study on microstructure and mechanical properties of SMD processed Ti64. Flat, dog bone shaped tensile testing specimens were made

using SMD process in Ar gas filled air tight chamber with TIG welding head. In spite of having highly inert atmosphere, a thin oxide layer was formed outside some of the parts. Prior β grains were found on the cross section after etching. Also two distinct regions have also been revealed among which the bottom region has parallel bands as shown in figure 2.1[28]. The microstructure consists of α phase lamellae with β phase matrix which was described as Widmanstätten structure. From the tensile tests, the UTS obtained was in between 929 to 1014 MPa, depending on orientation of the part and testing location. Specimens taken from the top of the part showed higher UTS since these have finer α lamellae, but the bottom portion having coarser lamellae has lower UTS. Also comparing with ASTM standards for cast material, the authors conclude that the SMD processed Ti64 at least meet the minimum requirements as cast materials.

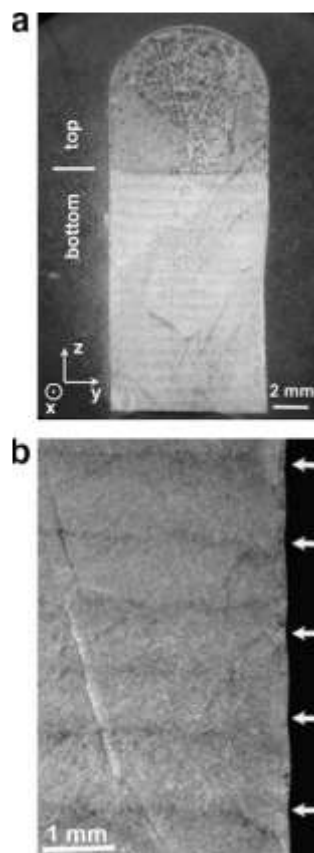


Figure 2.1: OM images of cross section after etching

The authors extended their research further by incorporating one more wire feed fabrication process that uses Nd:YAG laser beam to deposit material and comparing it with SMD process(2011). For the microstructure, it was that found that the laser beam ALM fabricated part has dull and gray surface whereas SMD produces shiny surface with brown and blue color. Elongated columnar β grains growing epitaxially towards deposition direction were found on side surfaces for both cases. The UTS values found to be ~900-1000 MPa for both cases. it was claimed that wire based systems have advantages over powder based systems such as higher deposition rate, less contamination and lower material costs. For laser beam ALM, hardness gradient was visible in the top region with finer α/β lamellar structure. In both cases, the strain at failure was found to be higher in z direction compared to x direction. Also the SMD process showed higher strain at failure than laser beam ALM. Heat treatments were done to observe whether it helps with mechanical properties or not. Heat treatment at 600°C did not affect significantly, however, heat treatment at 843°C increases strain at failure noticeably. SMD processed and heat treated at 843°C Ti64 can be comparable to wrought Ti64. For both processes, the fatigue limit was more than 770 MPa.

The more popular method that deals with Ti64 is electron beam AM. Facchini et. al. [29] presented a thorough study on microstructure and mechanical behavior of EBAM processed Ti64. To improve mechanical properties, HIP was done at 915°C for 2 h at 1,000 bar. Kroll reagent was used to reveal microstructure after polishing. The microstructure is very fine lamellar with α phase in β grain boundaries as shown in figure 2.2[29]. The density was found to be 99.4% of the theoretical one, so the surface was essentially pore free.

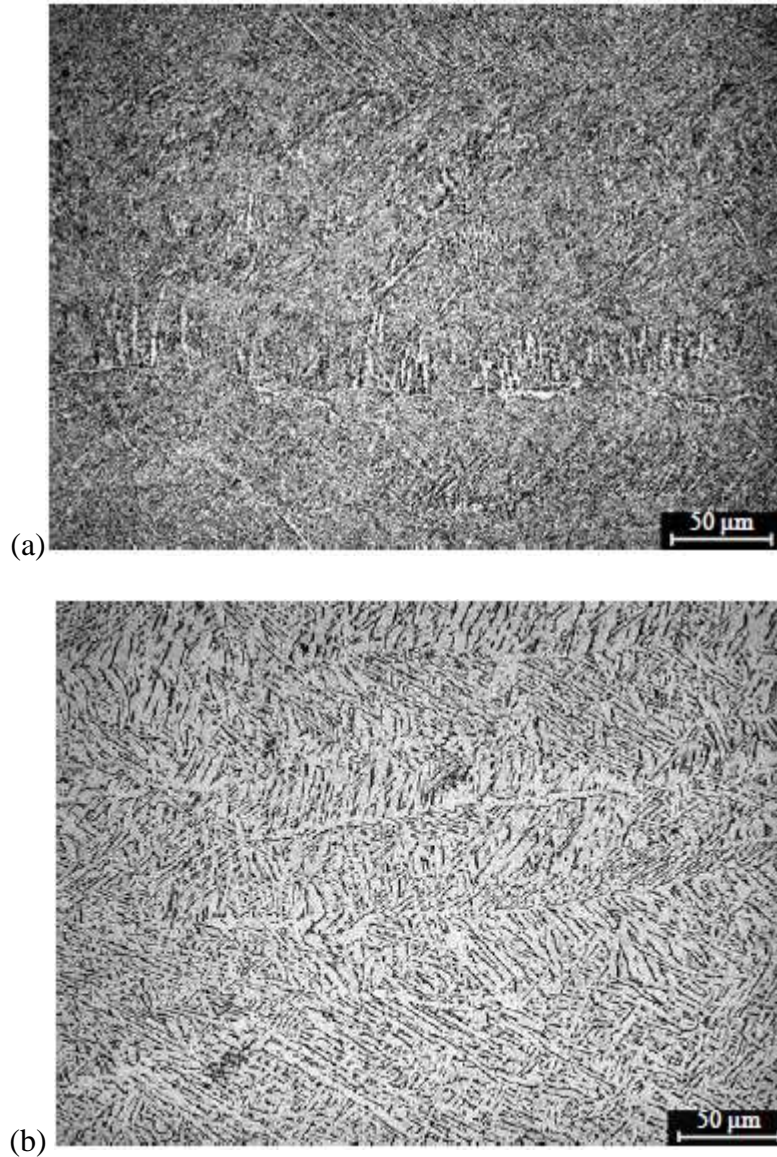


Figure 2.2: OM images of microstructure of (a) as built specimen; (b) HIPed specimen

HIP does not alter the microstructure to a great extent, but it increases the lamellae size almost twice as illustrated in figure 2.2. The stress strain curve followed the same trend as that for wrought material, thus the tensile properties as well. But HIP increases fatigue strength. The authors concluded with revealing the fact that the EBAM can produce materials as good as wrought ones making it suitable for biomedical and other sophisticated applications.

2.3 Selective Laser Melting: Microstructure and Mechanical Properties

Microstructure and mechanical properties of parts fabricated by different AM processes have always been one of the most discussed topics among researchers. Amato et. al. [30] has done similar studies on microstructure and mechanical properties of Inconel 718 fabricated by SLM process. Cylindrical components were fabricated with 1.6 cm diameter and 8.75 cm height using precursor, pre-alloyed atomized Inconel 718 powder. The cylindrical parts were made using two building directions-one with cylinder axis parallel to the beam direction and another with perpendicular. Then the as fabricated cylinders were annealed and hot isostatic pressed. The samples were cut, mounted, polished and electro-etched using a solution of 70 ml phosphoric acid and 30 ml water at room temperature and 5V for 5 to 120 seconds. From OM images of the microstructure of as fabricated x axis oriented cylinders, it was found that the melt pool width~ 75 to 100 μm and the average layer thickness~50 μm . Columnar grains grow in a parallel direction to the build direction on side surface. On Z plane, equiaxed or regular spatial columnar architecture was observed with dimension 0.5 to 1 μm . Samples after being treated with hot isostatic pressure and initial stress relief for 0.5h by annealing at 982°C showed similar architecture but more regular columnar grains. Z axis oriented cylinders also showed similar microstructure. Similar experiments were done using nitrogen gas environment during the fabrication process. Both process produced parts with unusual columnar microstructure with primarily $\langle 200 \rangle$ textured γ' phase precipitate. This type of microstructure is very similar to wrought Inconel 718. The microindentation hardness for x axis oriented as fabricated cylinders was 3.9 GPa whereas the hot isostatic pressed and annealed (at 982°C for 0.5h) samples showed a Vickers' hardness of 5.7 GPa. On the other hand, samples which were treated with HIP and annealing at 1160°C for 4h had a microhardness around 4.6 GPa. The researchers did not find

any specific effect of varying environment (argon or nitrogen) on microstructure or mechanical properties.

Studies have been done on effect of different heat treatment on as fabricated parts as well. Zhang et al. [31] studied on SLM processed parts made of spherical 5-45 μm gas atomized Inconel 718 powders. The as fabricated parts were treated by (1) solution treatment and (2) homogenization treatment + solution treatment + double aging treatment. Standard tensile test bars with 5 mm diameter and 35 mm length were machined out of the as fabricated parts to conduct the experiments. Then the samples were polished using abrasive papers of varying grit sizes and diamond suspension, and etched using Kalling's reagent. The as fabricated samples showed dendritic microstructure with a dendritic arm spacing of around 698 nm. Due to finer dendritic microstructure because of higher cooling rate, SLM processed IN718 has superior tensile properties compared to cast IN718. But also due to the presence of brittle Laves phase, as fabricated parts showed lower tensile properties than wrought IN718. To improve that, the parts were heat treated. Partial recrystallization occurs and the remaining Laves phase and δ phase impede grain growth after standard SA treatment since the solution temperature is not too high. After HAS treatment, full recrystallization occurs and finer and coarse grain size alternate in horizontal section. Also, the microstructure in vertical and horizontal section are different, thus have a possibility of different mechanical properties as well. The strength values increase whereas ductility slightly decreases after SA treatment as shown in figure 2.3. The UTS and hardness are similar in HAS treated samples, but YS slightly decreases. The elongation increases by 22%.

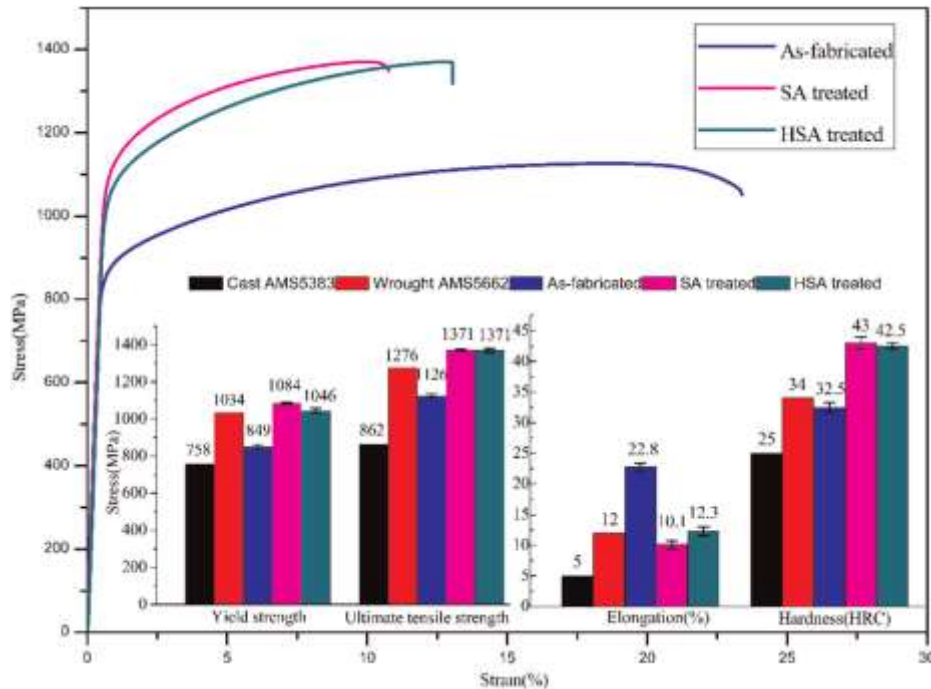


Figure 2.3: Tensile curves and room temperature mechanical properties of IN718 superalloy processed by SLM in as-fabricated, SA treated and HSA treated states[14]

The microstructure and mechanical properties of SLM fabricated IN718 have also been studied by Wang et al. [32]. it was reported that the heat treated SLM IN718 have comparable properties to those of wrought IN718. The powder used to fabricate parts was of 50 μm . The fabricated samples were treated by (1) solution treatment at 980°C for 1h (air cooling) and (2) double aging at 720°C for 8h (furnace cooling) and at 620°C for 8h (air cooling). Standard tensile testing bars were machined to conduct the experiments. All the as fabricated samples found to have nearly 100% density. On the cross section of the as deposited samples, melted tracks are observed in OM caused by alternating x/y raster scanning strategy. On the side and front surfaces, cut ends of the melted tracks form layers of arcs. SEM images reveals fine dendritic structure induced by very high cooling rate. On the cross section, the microstructure is less organized due to the interaction between alternating scanning patterns, whereas the solidification microstructure is more regular on the side surface. On the vertical section (side surface), parallel

dendritic grains grow in the direction of Z axis. After heat treatment, the regular dendritic structure no longer exists. Nb and Mo rich precipitates are found in both sections. Niobium rich precipitates are δ and Laves phase. γ and γ' particles disperse and precipitate further to increase strength in double aging treatment. Tensile properties of as deposited IN718 is lower than wrought IN718 (UTS 1137-1148 MPa), but after heat treatment, both the tensile properties (UTS 1280-1358 MPa) and ductility becomes comparable to wrought IN718 which makes them suitable enough for applications. The elastic modulus of as deposited samples are 204 GPa whereas heat treated samples have 201 GPa.

Similar results have been found by Chlebus et. al. [33] for cylindrical IN718 specimens fabricated by SLM and then treated by homogenization and aging processes. The research was done on two types of specimen-cuboidal and standard tensile test bars. The cuboidal specimens served as control specimens to optimize process parameters and also for heat treatments. The tensile testing bars were made in four groups in terms of different angles of tension axis with building direction and scanning direction. Samples from each group have also been treated with four variants of heat treatment processes. To reveal microstructure, polished samples were etched using 15 ml HCl, 10 ml Glycerol and 5 ml HNO₃ solution. On YZ plane, the columns appeared to be in slight angle with the build direction whereas on XZ plane these are in slightly zigzag direction as shown in figure 2.4[33]. Each individual column consists on γ grains with boundaries. The grains are directionally solidified in $\langle 0\ 0\ 1 \rangle$ direction which is the direction of heat flux. The grains take more like cellular form in rapid solidification which causes rapid cellular/dendritic growth towards build direction. Also the composition is inhomogeneous between two dendritic cells and between two adjacent layers. Small particles of eutectic mixture of γ +Laves phase and MC type carbides were found in the interdendritic regions. Highest

Young's modulus was ~208 GPa which was found in the specimen which had tension axis at 45° to build direction and also at 45° to both scanning directions x and y. The trend was found to be $E(0^\circ) < E(90^\circ) < E(45^\circ)$. After aging process, the hardness increased 48%, from 312 to around 461 HV1. Aging after quenching from 1040°C, hardness increased by 52%. It was also revealed that SLMed and heat treated IN718 has slightly superior mechanical properties than wrought IN718.

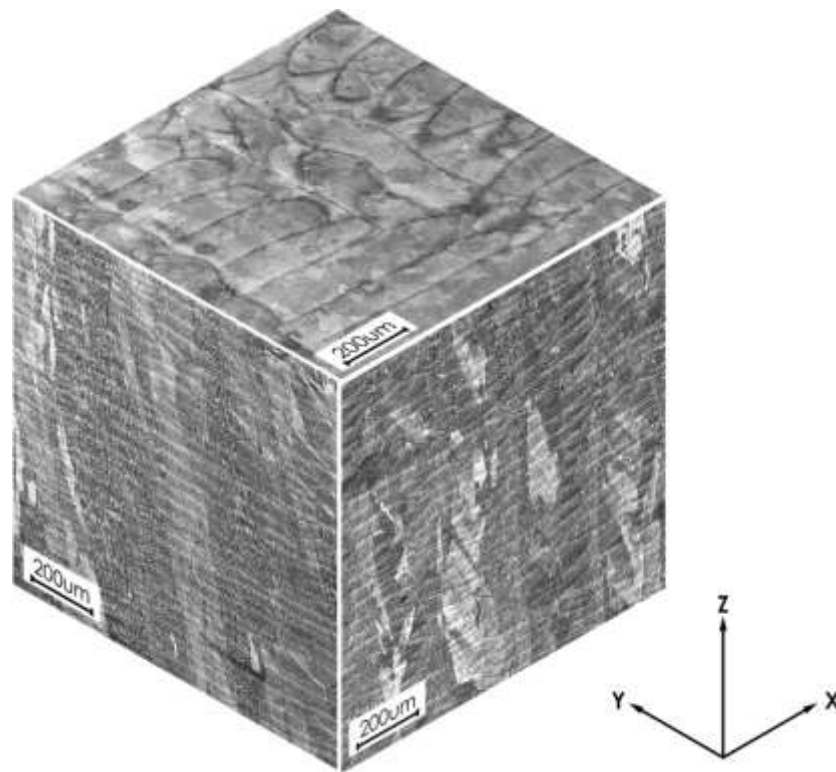


Figure 2.4: Microstructure of as deposited Inconel 718

Even though it is not common to use Ti-6Al-4V in SLM process, but studies have been carried out on this. Thijs et. al. [3] studied microstructural evolution in Ti64 during SLM process. To conduct this research, rectangular samples were produced using 3 different scanning strategy with 2 different scanning vectors namely alternating and unidirectional. To reveal microstructure, the polished samples were etched using 50 ml distilled water, 25 ml HNO₃ and 5

ml HF solution. Acicular martensitic phase was found in as deposited samples. The microstructure of the top surface resembles the scanning pattern as found by other researchers too. The width of the each melted track is almost equal to the hatch spacing. Herringbone type pattern can be observed on samples where alternating scanning vectors were used. Thus the grain direction depends on the local heat conduction direction. Elongated grains are observed on front and side views having heights much larger than layer thickness. The microhardness found to be 409 ± 35.9 Hv. Influence of energy density has also been studied by varying scanning velocity and hatch spacing. A lower velocity with same hatch spacing results in coarser microstructure, more intense dark bands along melt pools and higher hardness. On the other hand, increase in hatch spacing causes decrease in hardness. Effect of various scanning strategy has been observed. With the unidirectional scanning pattern, the herringbone pattern no longer exists. A grid type pattern can be seen on top view for alternating scanning directions. Grains become more equiaxed and the width resembles hatch spacing. The density also improves with this type scanning pattern.

Process parameters play a vital role in densification, microstructure and properties of the finished product. Jia et. al. [10] reported densification behavior, mechanical properties and high temperature oxidation behavior of SLM processed IN718 under various process conditions. Cubic specimens were fabricated using four different energy densities which were obtained by four combinations of laser powers and scanning speed following the equation:

$$\eta = P/v \quad (2.1)$$

where η is energy density, P is laser power and v is scanning speed [10].

The melted tracks become discontinuous with large balls surrounded by pores at an energy density as low as 180J/m. The densification is also very low (73.6%). With increasing

energy density, the scanning tracks become more regular with some occasional shrinkage cavities. The densification also increases. At the properly settled energy density of 330 J/m, the pores or balls are alleviated, the surface becomes smooth and the densification reaches at 98.4%. The increased energy density weakens dynamic viscosity and balling phenomenon, thus creates smooth surface morphology. At a lower energy density with higher scanning speed, coarse columnar γ dendrites are visible with cracks in the center at higher magnification. With higher energy density with higher laser power, the dendrites become more refined, but still disconnected with incomplete precipitates in the inter dendritic regions. With even higher and properly settled energy density, directionally solidified finer columnar dendrites were obtained. As reported in other papers too, the epitaxial growth of slender columnar dendrites is induced by the heat flux towards the substrate or the previous layers. The microhardness was 331.9 HV_{0.2} at 180J/m energy density whereas it increases as high as 395.8 HV_{0.2} at 330 J/m. The intermetallic phase γ' along with the accumulation of Ni with γ matrix contribute to increasing microhardness. The wear rate at 330 J/m is also the lowest which was 4.64×10^{-4} mm³/N m. The high temperature oxidation was measured by mass gain for a specific oxidation time. For 180 N/m, the mass gain is highest and keeps increasing for 70h. For 275, 300 and 330 n/m, the mass gain is almost constant for 70h. However, the mass gain is lowest for 330 N/m, which indicates high oxidation resistance for high energy density. Since the microstructure is highly refined at high energy density, it causes lower mass gain.

2.4 Selective Laser Melting: Effect of Build Height

Even though several works have been done various aspects of SLM process, no work has reported the effect of build height which can be crucial keeping the process nature in mind. In a previous study performed by the same group, Wang et. al. [5] presented the effect of build height in microstructure and mechanical properties of SLM processed Inconel 718. A solid block with dimensions of 40 mm by 40 mm by 6 mm was fabricated for the experiments. 8 specimens were cut and polished to conduct the experiments- 4 on Y plane and 4 on Z plane. To reveal the microstructure, the specimens were etched in 20 ml hydrochloric acid (37 wt. %) and 20 ml (68 wt. %) nitric acid, and 1 g copper chloride solution. For mechanical properties, nanoindentation was done on each sample with 3×4 grid size.

All the samples showed columnar dendrites on Y plane and equiaxed grains on Z plane as reported by many other researchers too. As far as the build height effect is concerned, the bottom sample showed lower columnar structure width which is caused by higher cooling rate. The bottom sample is closest to the substrate, thus heat dissipates quickly towards bottom. The width keeps increasing until a stable value is reached and decreases again for the top sample. The top sample is exposed to lower environment temperature since no other layer is deposited on it, so the cooling rate is higher for the top as well. The highest columnar width was found to be 146.77 μm for the middle-top sample.

Y plane shows a trend in mechanical properties for different build heights as illustrated in figures 2.5 and 2.6[5]. But Z plane does not show any significant results. Other than that, the Young's modulus and nano-hardness values are more or less comparable to wrought materials.

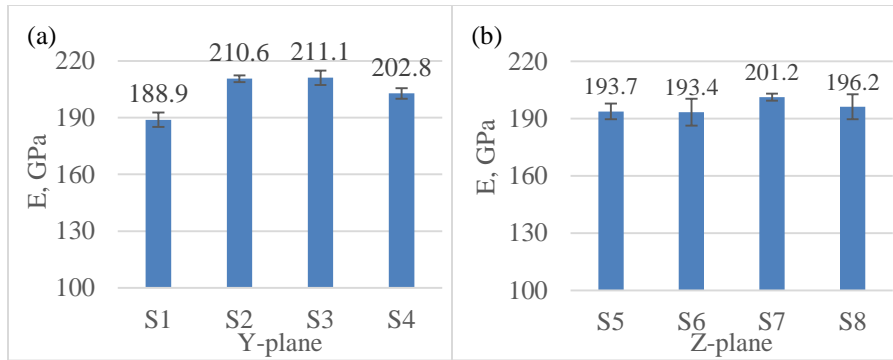


Figure 2.5: Young's Modulus for the SLM-processed Inconel 718 alloy

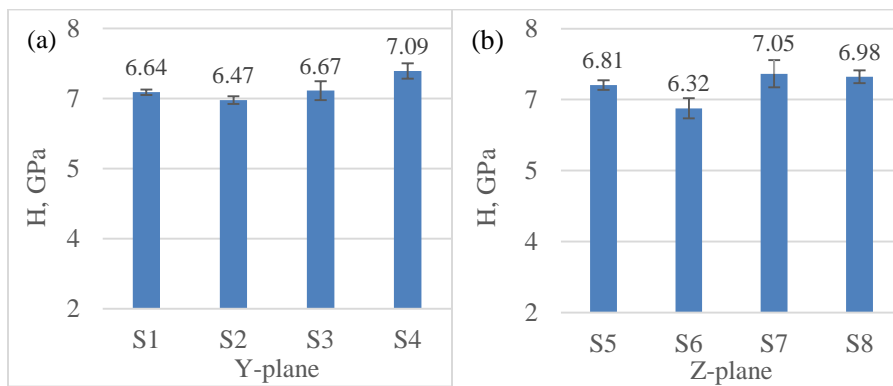


Figure 2.6. Nano-hardness of SLM-processed Inconel 718 alloy

In this current research, a further approach has been made to study the build height effect on SLM processed IN718, but for different geometry which introduces some added complex thermomechanical phenomena with the staircase feature.

CHAPTER 3: EXPERIMENTAL DETAILS

3.1 Part Fabrication

The part used in this research work is made of Inconel 718 and fabricated by Selective Laser Melting using Concept Laser M2 Laser Cusing System at NASA's Marshall Space Flight Center (Huntsville, AL). This machine is suitable for aluminum, titanium and nickel based alloys. The specifications of the machine is given below[15]:

Build envelope LaserCUSING®: $250 \times 250 \times 280 \text{ mm}^3$ (x, y, z)

Layer thickness LaserCUSING®: 20 - 80 μm

Production speed LaserCUSING®: 2 - 20 cm^3/h (depending on material / laser power)

Laser system Fibre laser: 200 W (cw), optional 400 W (cw)

Scanning speed: 7 m/s, 4.5 m/s for variable focus move

Focus diameter: 50 μm , optional variable focus move (50 μm – 500 μm)

Connected loads: Max. power consumption 7.4 kW

Power supply 3/N/PE AC 400 V, 32 A, compressed air 5 bar

Inert gas supply: 2 gas connections provided

N_2 generator external (optional)

Inert gas consumption: $< 1 \text{ m}^3/\text{h}$

Operating conditions: 15 - 35°C

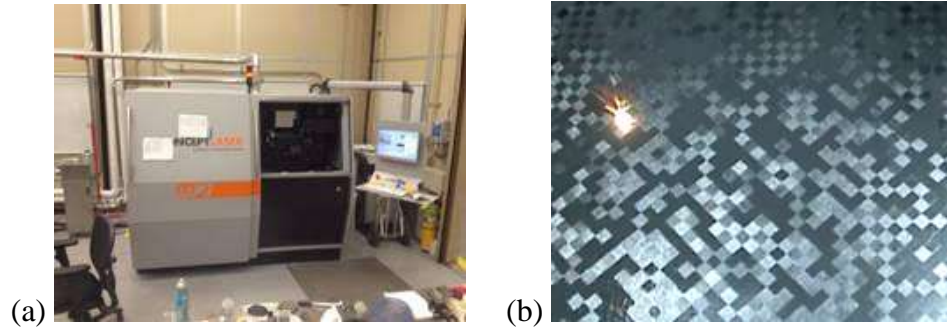


Figure 3.1: (a) Concept Laser M2 Laser Cusing System, (b) Island scanning strategy[5]

The part is shown in figure 3.2. The total height of the part is 60 mm. The height of lowest major step is 3 mm and 2nd major step is 30 mm. Each major step has 2 minor steps on the top surface. The height of each minor step is 60 μ m. The surfaces close to the bottom of the part were studied and compared since the surface under each step has been through different number of thermal cycles due to different height of the steps. The build height effect was studied on the top surfaces of each step. The surfaces under 1st step from different heights were also taken for comparison since they are subjected to different number of thermal cycles too.

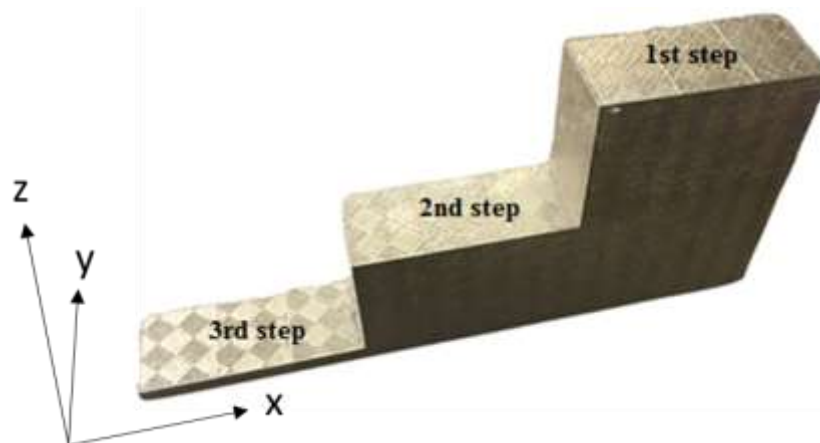


Figure 3.2: As deposited Inconel 718 part

To produce the part, fine pre-alloyed Inconel 718 powder was used. The laser beam of diameter 54 μ m moves across the powder layers to scan the contour first and then to fill the

inside using island scanning strategy. The ‘island’ consists of 5×5 mm squares. The islands were ‘selectively melted’ in random order and simple alternating scan vectors were used. The island patterns are shifted by 1 mm for subsequent layers. The process parameters are given in table 3.1[5].

Table 3.1: Manufacturing parameters

System	Laser Type	Spot size, μm	Power, W	Layer thickness, μm	Hatch spacing, μm	Scanning speed, mm/s	Scanning Pattern
Concept Laser M2	CW Fiber	150	180	30	105	600	Island, 5mm

3.2 Metallographic Sample Preparation

3.2.1 Cutting

Samples were cut using two cutting machines- Struers Discotom-100/-10 Cutting equipment and Allied High Tech TechCut 4™ Precision Low Speed Saw. The first is an abrasive cutter and suitable for faster cutting of very hard materials. For initial cutting when the samples were fairly big, this machine was used. It can cause heating of cutting location, but that is minimized by the coolant. Even though the machine has automatic mode, the samples were cut manually to have better control.



Figure 3.3: Struers Discotom-100/-10 Cutting equipment

For samples which were too thin to be in the abrasive cutter, Allied High Tech TechCut 4™ Precision Low Speed Saw was used which is a diamond cutting tool. This machine is very suitable for precision cutting and it removes minimal material. Since it is low speed compared to the abrasive cutter, it does not create a lot of heat, so there is minimum chance to alter the microstructure. It is automatic and samples were cut using 200-300 rpm speed.



Figure 3.4: Allied High Tech TechCut 4™ Precision Low Speed Saw

Since the study focuses on build height effect, the samples were cut from different height of the part keeping the objective in mind. Figure 3.5 shows the samples cut and mounted for Y plane analysis with their respective codes. There are total 12 specimens cut for Y plane analysis which were mounted in 8 epoxy resin samples. The sample codes can be represented by L.MYN where L is the serial number of step, M is serial number of sub-sections of that step which increases from top to bottom and N is the unique number of the specimen that increases from left to right. Y stands for the plane from which the specimens are taken.

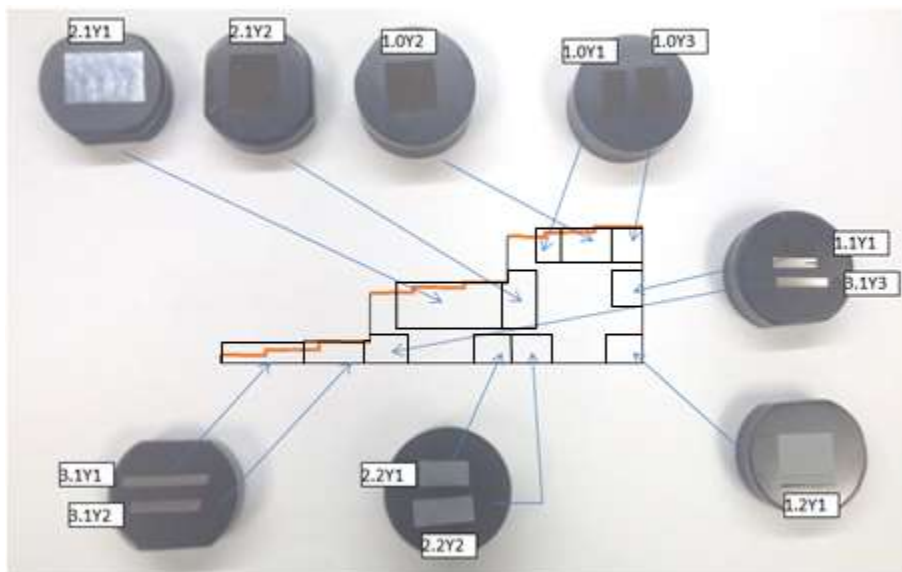


Figure 3.5: Samples cut from Y plane

In figure 3.6, the samples for Z plane analysis have been shown. Here samples were cut from top surface as well as from inside the part. The sample codes can be represented by L.MZN here where Z stands for the plane.

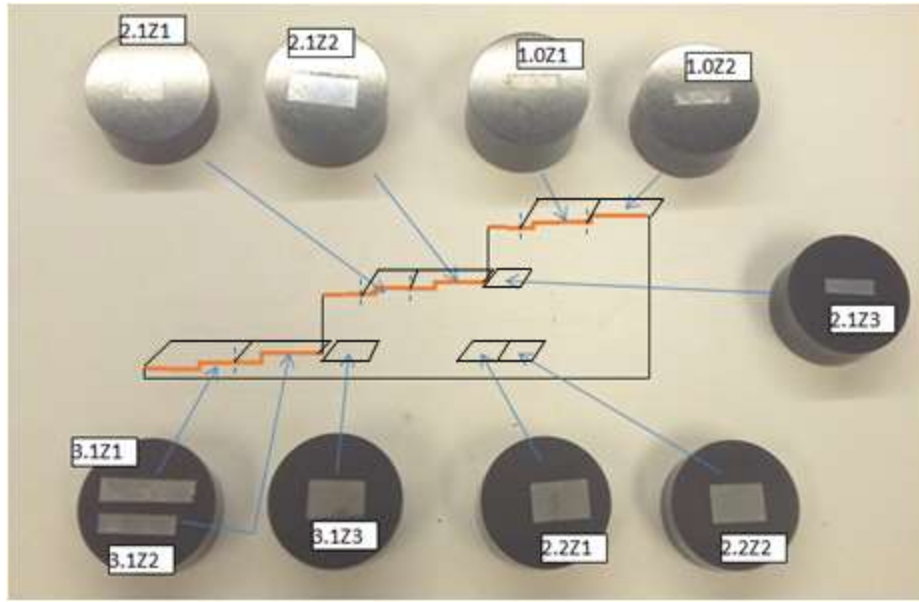


Figure 3.6: Samples cut from Z plane

Figure 3.7 shows the samples cut for X plane analysis. These samples were cut just to compare with those from Y plane and check whether these are same. The sample code system is same as Y and Z plane.

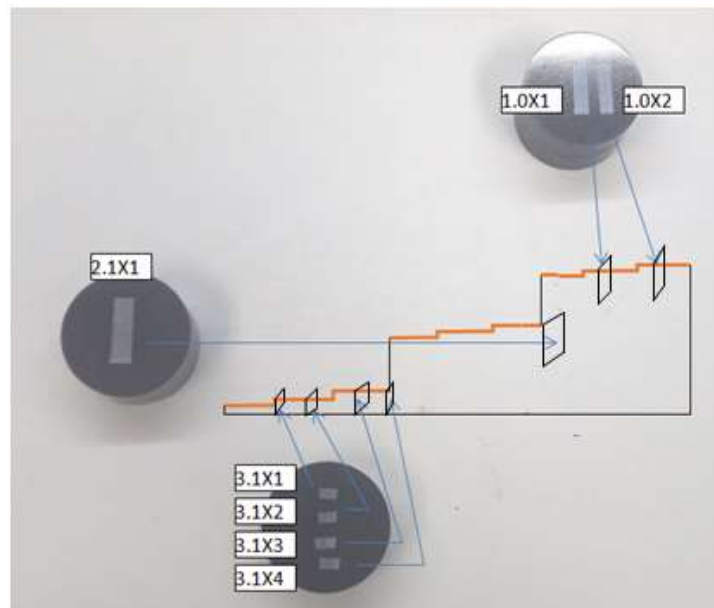


Figure 3.7: Samples cut from X plane

3.2.2 Mounting

All the samples were mounted using hot mounting technique in Struers Metallurgical Mounting - Labopress 3 equipment. Polyfast resin is used as mounting material and 25 kN force was used to press it. The heating time was 4 minutes and the cooling time was 3 minutes.



Figure 3.8: Struers Metallurgical Mounting - Labopress 3

3.2.3 Polishing

To prepare the surface for microstructure study and nanoindentation, samples were ground and polished using Allied High Tech MetPrep 3™ Grinder/Polisher. It is an automatic machine where we can program the polishing steps for specific amount of time. All the samples were polished in several steps. To get the scratch free microstructure results, all the samples from X, Y and inner Z plane were ground using abrasive grinding papers of 180 grit for 10 minutes, 320 grits for 10 minutes, 600 grits for 10 minutes and then polished using 9 μm diamond suspension for 5 minutes, 3 μm diamond suspension for 4 minutes and 1 μm diamond suspension for 1 minutes 30 seconds. The Z plane samples from the very top were ground using abrasive grinding paper of 600 grits for 5 minutes and then polished using 9 μm diamond suspension for 1 minutes, 3 μm diamond suspension for 1 minutes and finally 1 μm diamond suspension for 45 seconds. The Z plane samples from the top surface were polished as less as possible so that only one minor step is polished while keeping the lower step intact.



Figure 3.9: Allied High Tech MetPrep 3™ Grinder/Polisher

3.2.4 Etching

As the final step of metallographic preparation for microstructure study, the samples were etched. Several solutions can be used to etch Inconel718 surface. Initially the samples were etched using 20 ml hydrochloric acid (37 wt. %) and 20 ml (68 wt. %) nitric acid, and 1 g copper chloride solution. But this solution is extremely strong due to the presence of nitric acid, so it can even over etch a sample within 5 seconds which is not convenient. Then another solution is used which is called Kalling's reagent. The composition of this solution is 40 ml HCl+40 ml Ethanol+2.5g CuCl₂ and this solution takes more or less than 50 seconds to properly etch a sample. This method gives better control and result. Also it is a very widely used method for Inconel 718 alloy. A comparison of etched results by both of the solution is shown in figure 3.10.

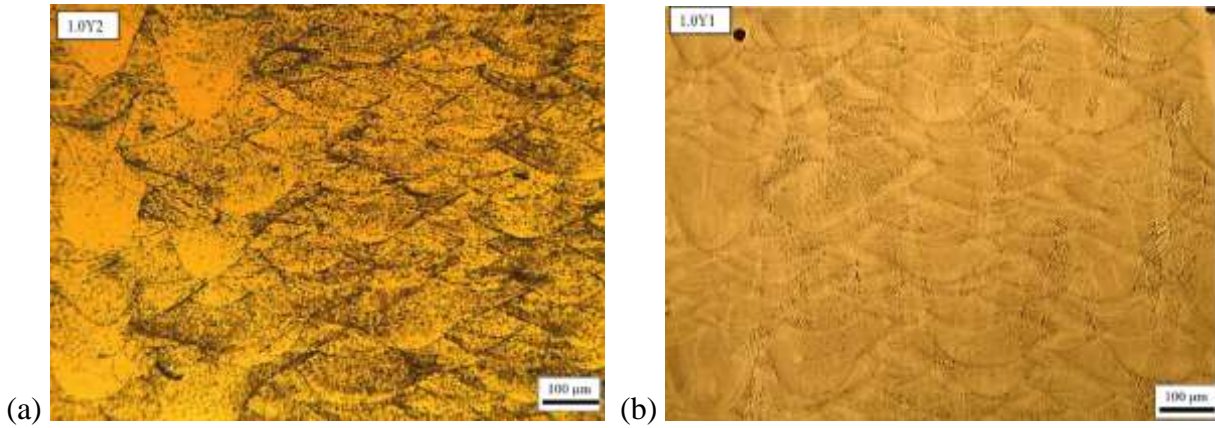


Figure 3.10: OM images of microstructure, (a) etched by HNO₃ solution, (b) etched by Kalling's reagent

3.3 Microstructure Study

3.3.1 Optical Microscopy

After polishing and etching, microstructures were observed using a Leitz optical microscope. The magnifications used were usually 50X, 100X, 200X and 500X.

3.3.2 Scanning Electron Microscopy (SEM)

The microstructures were observed using JEOL 7000F machine. For SEM study, samples were evacuated first using plasma cleaner so that it does not take too long to be evacuated during SEM. After that, the sample is installed inside the machine. When the pressure inside is less than 2×10^{-5} Pa, the session can start. Using the panel in the front, the surface is focused and images are taken at desired location. The surface should be focused at 3 times magnification of the desired magnification as a thumb rule. For example, if we want to take image at 2000X, it is recommended to focus the image at 6000X and then zoom out.

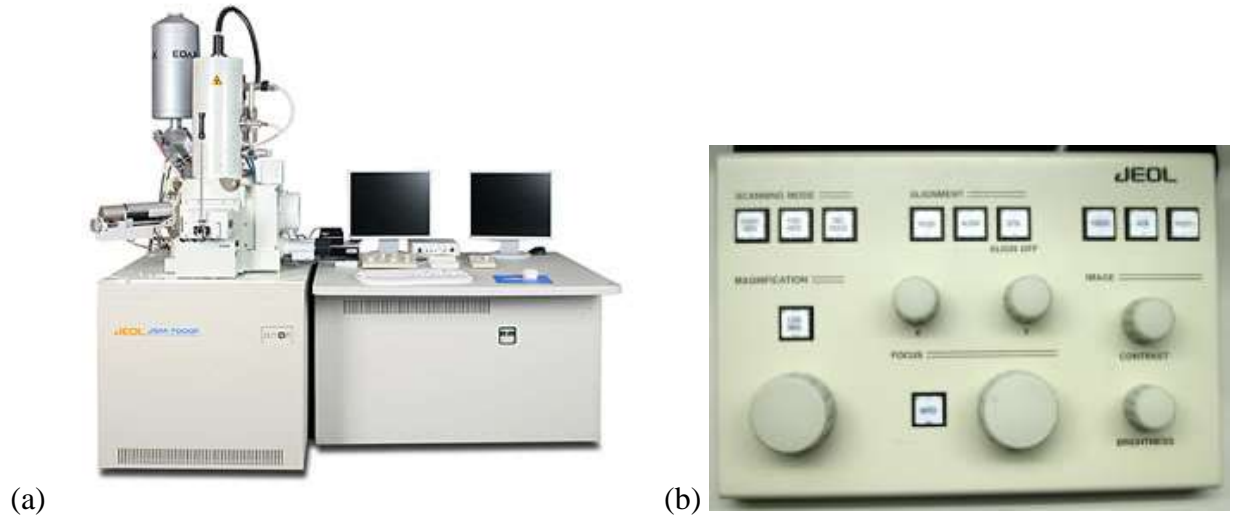


Figure 3.11: (a) JEOL 7000F machine for SEM; (b) operation panel

3.3.3 Motic Stereoscope

To observe microstructure at lower magnification (<50X), Motic stereoscope was used. Images can be taken at as low as 7.5X using this stereoscope. It gives a better idea of the general pattern of the microstructure without much detail which is convenient to relate the features with scanning pattern.



Figure 3.12: Motic Stereoscope

3.4 Nanindentation

Mechanical properties were measured using nanoindentation process with Berkovich tip to obtain Young's modulus and hardness. Also, it shows the force-displacement curves using which the properties are calculated. In Figure 3.13(a), the schematic of nanoindentation is shown where P is the applied load and h is indentation depth. A trapezoidal shaped loading and unloading method is applied with maximum force of $5000 \mu\text{N}$ which is shown in figure 3.13(b). In this method, the loading force goes up to $5000 \mu\text{N}$ in 5 seconds with a constant loading rate, holds it there for 2 seconds and then the unloading force goes back to zero in 5 seconds with a constant rate.

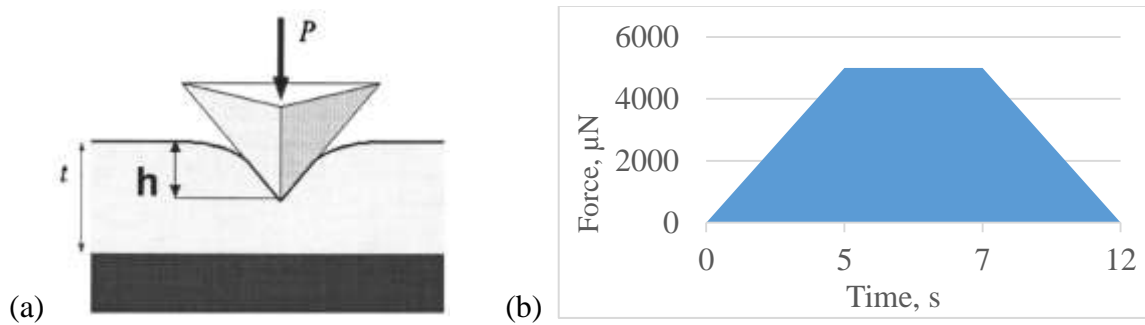


Figure 3.13 : (a) Schematic of nanoindentation and (b) Applied Load Function[5]

3.4.1 Hysitron Triboindenter

Tests on Y plane were run using Hysitron Triboindenter before it started having hardware issues. The tip used for this machine was a Berkovich tip of 100 nm diameter. Tests on one grid can be programmed and run at a time in this machine.

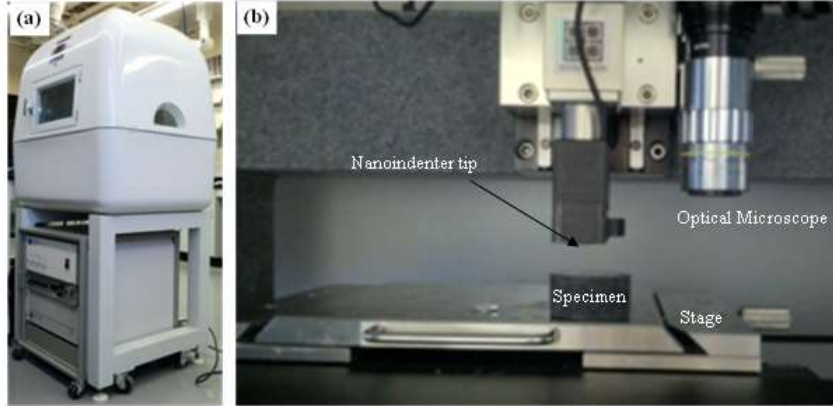


Figure 3.14: (a)Hysitron Triboindenter; (b) Nanoindentation setup[5]

3.4.1.1 Calibrations

Before running tests on Hysitron Triboindenter, 3 types of calibrations are necessary: 1. Air calibration, 2. Optical calibration and 3. Probe calibration. For air calibration, indents are made on air. This is also called an advanced Z axis calibration.

For optical calibration, 7 indents are made in an “H” pattern on Aluminum sample. After the indents are made, the cursor needs to be moved on the center of the “H”. The zoom factor used in this process is 5X and this needs to be maintained throughout the tests.

For probe calibration, 100 indents are made on a fused quartz sample since the microstructure of quartz is uniform throughout the entire surface. After the indents are made, the area function is calculated and saved. This calibration is good for next 200 indents before performing another calibration.

Since the transducer was repaired before running the tests, a machine compliance calibration was performed to adjust with new transducer constants. Machine compliance calibration has been performed with 14×14 grid size.

The compliance is given by,

$$C_c = \frac{\sqrt{\pi}}{2} \frac{1}{\sqrt{A}} \frac{1}{E_r} \quad (3.1)$$

Where E_r is the reduced modulus.

For the machine compliance calibration, 196 indents were made on the fused quartz sample. The starting load was chosen to be 5000 μN and the end load was 10000 μN . The space between two consecutive indents was 5 μm in both X and Y direction.

Following the instruction from the most recent manual, a chart is created from the indentation data and X-Y scatter graph is created where

$$X = 1/\sqrt{F_{\max}}$$

And Y = Compliance

After several trial and error, the latest compliance chart found was:

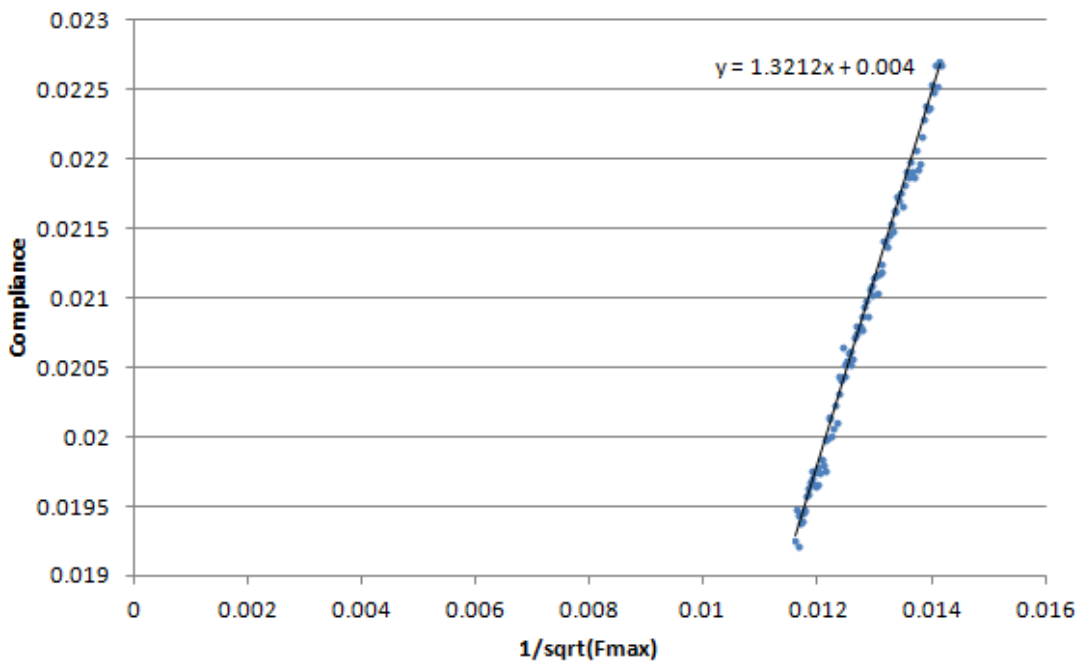


Figure 3.15: Machine Compliance chart

The value of Y intercept is the machine compliance.

So, $C_c = 0.004 \mu\text{m}/\text{mN} = 4.0 \text{ nm}/\text{mN}$

To verify the value, the calibration data were sent to Hysitron. The value was re-calculated there and it was found to be 4.3 nm/mN which is close to what we found. Either value could be used. Other transducer constants were set according to the data sheet provided by the company.

To eliminate any possible contamination, the fused quartz sample and the tip were cleaned. Then air calibration, optical calibration and probe calibration were performed keeping the value of compliance as 4.3 nm/mN.

3.4.1.2 Nanoindentation tests

After all the calibration process is done, actual tests were run for 4×4 grid size. The distance between indents was 5µm in both X and Y direction. After the indents are made, the load-displacement curves are plotted and the Young's modulus and hardness can be obtained from there. The Young's modulus obtained directly from the machine is reduced Young's modulus which is caused by the deformation of the tip itself. The actual modulus is calculated using an equation provided by the manufacturer which is discussed in Chapter 4. Data were taken at least three locations on a sample so that the average can be calculated.

3.4.2 Nanoindenter G200

Due to some issues in Triboindenter after testing Y plane samples, tests on Z plane samples were switched to the Agilent Technologies Nano Indenter G200. This machine is more convenient than the previous one since tests for multiple locations on multiple samples can be programmed and run at a time. The tip used in this machine was a Berkovich tip of 20 nm diameter. The probe needs to be calibrated for 200 indents for this machine as well.



Figure 3.16: Nano indenter G200

3.5 Finite Element Analysis: Nanoindentation

Different studies have been performed to combine numerical simulation technique with the nanoindentation experiment. Antunes et al. [21] introduced a reverse approach to obtain plastic properties using Vickers indenter and numerical simulation. Ogasawara et al. [22] proposed a technique to determine plastic properties of a bulk material from one conical indentation test. Fang et al. [23] obtained elastoplastic properties of welding joint material by inverse nanoindentation analysis using finite element method. The simulation results differ from experimental results by almost 13%. In this study, a simulation approach has been performed to compare with experimental results.

Finite element model has been developed both in 2D and 3D using ABAQUS. The plastic properties given in ABAQUS simulation are Yield Stress, σ and Plastic Strain, ϵ_p .

For $\sigma > \sigma_y$,

$$\sigma = \sigma_y \left(1 + \frac{E}{\sigma_y} \epsilon_p \right)^n \quad (3.2)$$

where, σ_y is Yield Strength, E is Young's modulus, and n is Strain hardening exponent [25].

For 2D simulation, the model was considered to be axisymmetric. Part size was taken as $3000\text{nm} \times 3000\text{ nm}$ and it is considered to be deformable. A partition of $600\text{nm} \times 600\text{ nm}$ was created near the indentation to obtain finer mesh. The tip is considered to be analytical rigid. Tip diameter was taken as 100 nm and contact surface was assumed to be frictionless[24].

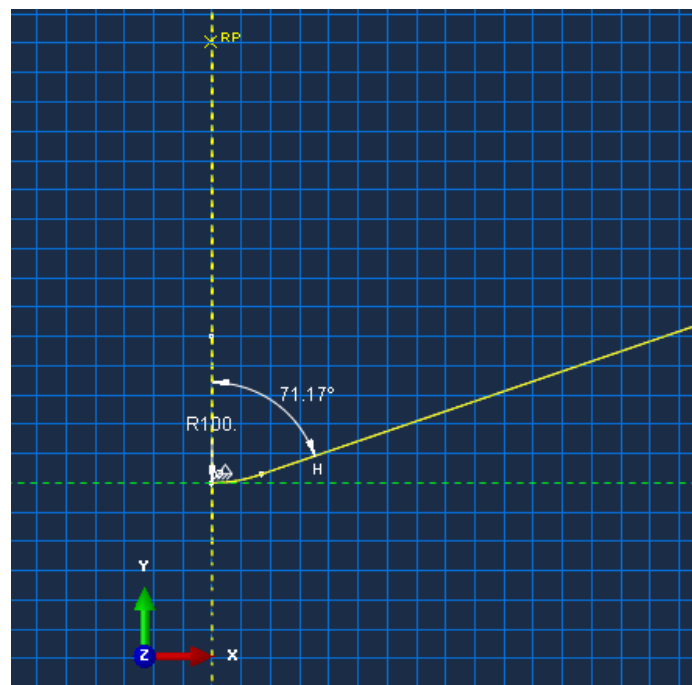


Figure 3.17: Berkovich tip in 2D analysis

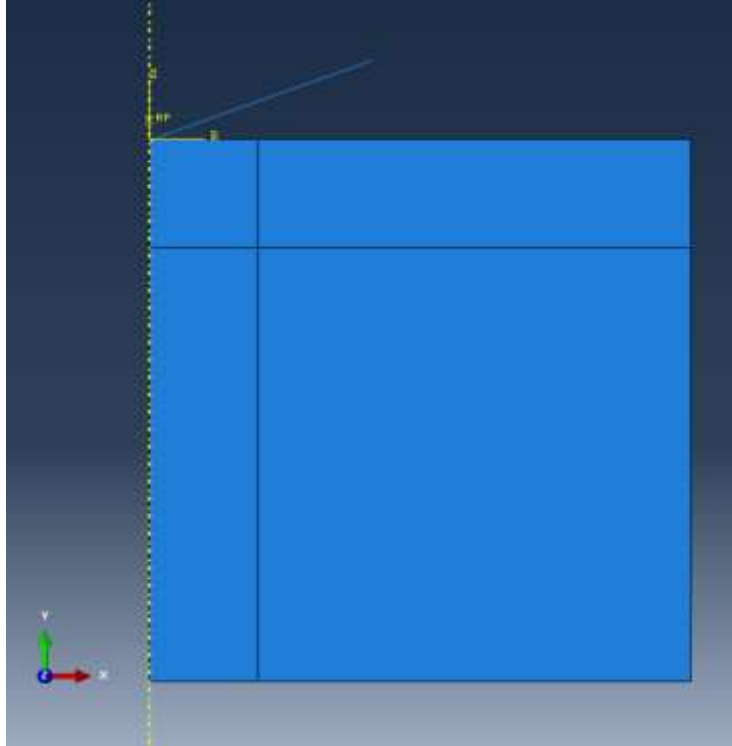


Figure 3.18: Tip – sample assembly in 2D analysis

For meshing, number of elements was chosen to be 80 with a bias ratio of 5 near the tip. On the area far from the tip, number of elements is 30 with the same bias ratio. Total number of nodes is 12321 and the number of elements is 12100.

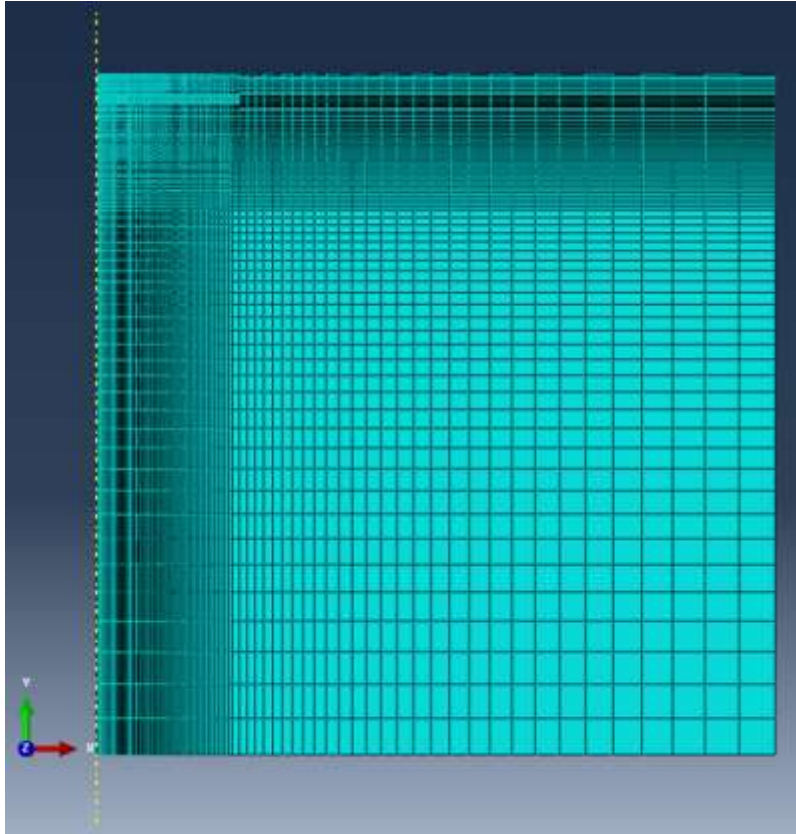


Figure 3.19: Meshing in 2D analysis

For most of the trials if not all, the Young's modulus is considered to be 206 GPa for Inconel 718 as found in [5]. Maximum displacement of the tip-sample contact point was specified as one of the boundary conditions according to the nanoindentation results obtained in [5]. Force cannot be specified in this set up. So obtaining the expected force was the actual challenge.

To validate the model, simulation was performed to duplicate some results from literature [23]. The simulation was run by varying Yield strength and strain hardening exponent since these two inputs seemed to affect the results most. The results were almost duplicated as shown in the force-displacement diagrams in figure 3.20.

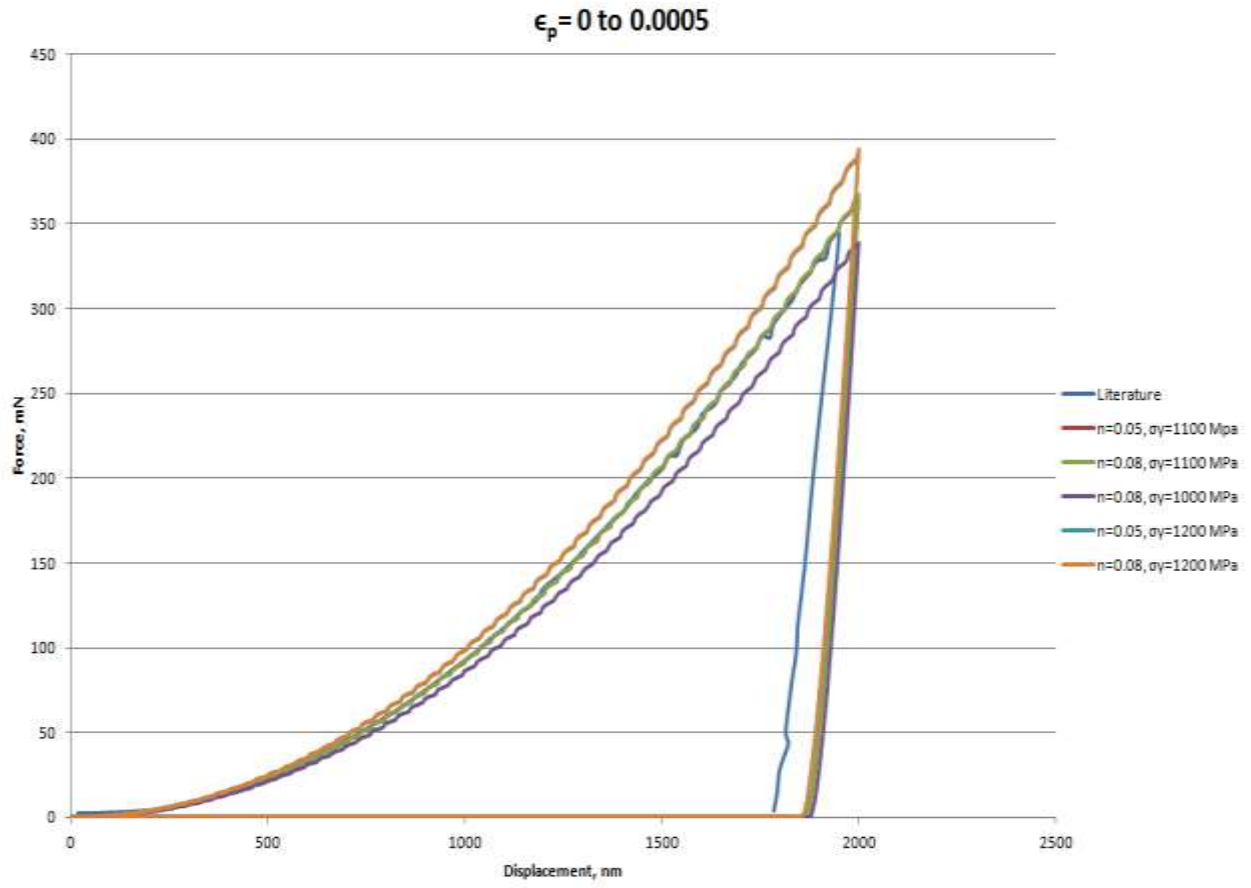


Figure 3.20: Force-displacement diagrams obtained from finite element analysis in literature

CHAPTER 4: RESULTS AND DISCUSSION

4.1 Microstructure

4.1.1 Y plane: General Features

The microstructure of Y plane is revealed by etching the polished surface and then observed using optical microscopy. Several magnifications have been used to achieve a better understanding of the features and detect whether there is any difference between various samples taken from various locations of the part. An example of microstructural features is shown in figure 4.1. The figures are taken from the sample 2.1Y1 which is located at the second major step of the as deposited part. The microstructure consists of columns of arc shaped features which indicate cut sections of molten pools created by the laser. The scanning strategy and the highly localized heat play vital role in creating this type of microstructure which is induced by Gauss energy distribution of the laser. The depth of the arcs is not constant. There are some deeper pools visible surrounded by the fairly similar shallow pools. The deeper features can be characterized by the starting and ending of a scan since the melt pool is supposed to have a rounded front and prominent tail along the direction of motion [1] which can be described as a 'keyhole'. The shallower arcs represent somewhere in the middle of laser melted tracks. The overlap between two adjacent layers forms the metallurgical bonding. At higher magnification, fine dendritic structure growing almost parallel to build direction is visible which are caused by high cooling rate as shown in figure 4.1(b). The columnar microstructure which grows in a perpendicular direction with the powder layers is caused by the vertical heat flux towards the substrate. The grains align towards the steepest thermal gradient during the manufacturing

process [2]. The average layer thickness is found to be $\sim 50 \mu\text{m}$ whereas the average width of melt pool is $\sim 150\text{-}200 \mu\text{m}$.

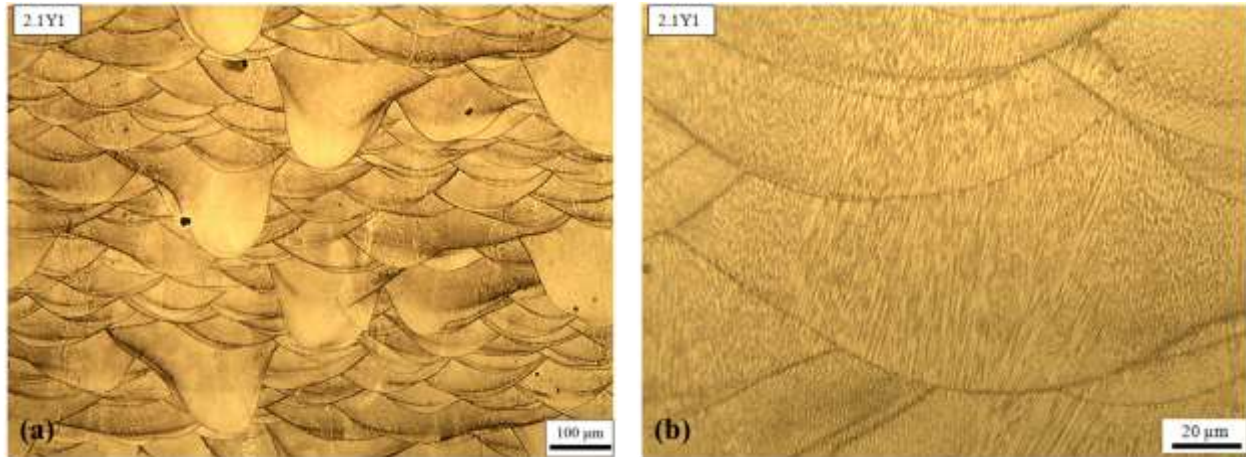


Figure 4.1 Microstructure of Y plane

4.1.2 Y plane: Effect of Thermal Cycle

One of the major objectives of this research is to study the effect of number of thermal cycles in different heights of the part. To observe that, a comparison between samples taken from different heights, but same horizontal position has been shown in figure 4.2. The very bottom sample 1.2Y1 is closest to the substrate, therefore experiences highest cooling rate. Also being at the bottom, 1.2Y1 was subjected to repeated thermal cycle of solidification and re-melting. On the other hand, 1.0Y3 is near the top of the part and has been through less number of thermal cycles compared to 1.1Y1 and 1.2Y1. Despite of experiencing different thermal history, the microstructure images taken in optical microscope reveals very slight difference in different build heights. The grains grow epitaxially from one layer to another. Due to heat conduction towards the previous layers and substrate in the Z direction, the grains grow in elongated shape. The number of deeper melt pools seems to be higher near the bottom due to higher heat accumulation caused by continuous re-melting. Also the bottom area has the higher cooling rate since it is closest to the substrate. Besides the depth of melt pools, effect of etching varies in

different locations. The arcs look more defined in the middle section than top and bottom. The melt pool boundaries are visible since the boundaries are preferentially etched even though the grains grow epitaxially. This indicates presence of intermetallic phases along the melt pool boundary which causes the dark band [3].

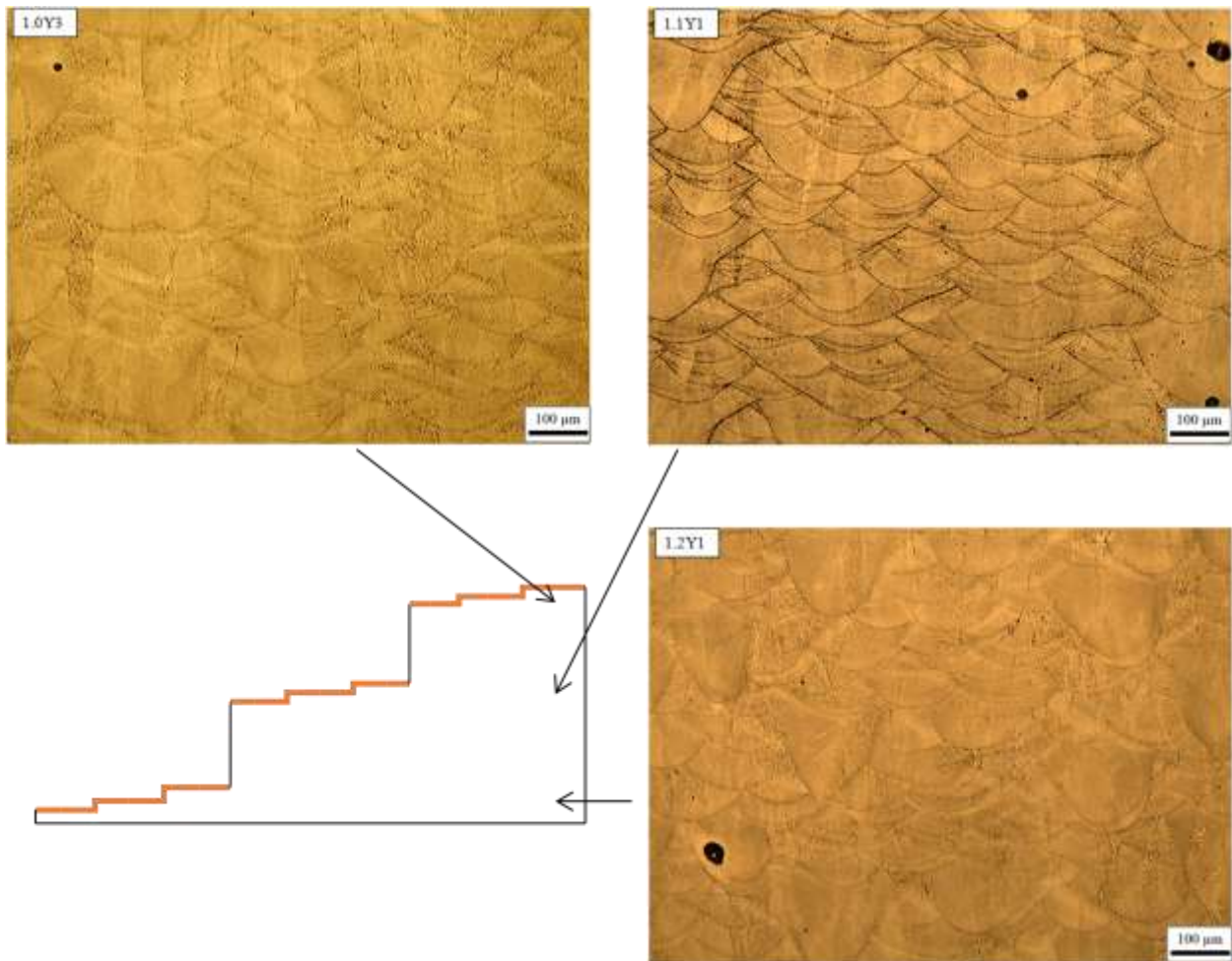


Figure 4.2: Effect of thermal cycle on Y plane

4.1.3 Y plane: External and Internal Surface

A comparative study between ‘external’ and ‘internal’ surface has also been performed. The top surface of each step is considered to be the ‘external’ surface while the surfaces inside the steps are considered to be ‘internal’ surfaces. The thermal history is considerably different for an external and corresponding internal surface at same height. The external surface does not

go through repeated thermal cycles since there is no more melting above the top surface, but the internal surfaces experience continuous solidification and re-melting. Figure 4.3 shows an example of external and internal surface microstructure comparison taking the middle step into account. 2.1Y1 represents the microstructure of external surface while 2.1Y2 represents the internal one. In figure 4.3(a), the rows of narrow arcs are repetitive. The rows of deeper arcs start where the rows of narrow arcs end. The distribution of arcs is more regular than that in figure 4.3(b). Also the shape and depths of shallow and deep molten pools are more or less same throughout. In figure 4.3(b), there is mixture of shallow and deep molten pools and the shape and depths are not very repetitive. The location inside a part continues to survive thermal cycles of re-melting and solidification whereas the location close to top gets solidified in its final shape quickly and in a more organized manner. So the cut sections of the irregular microstructure inside the part appear as figure 4.3(b).

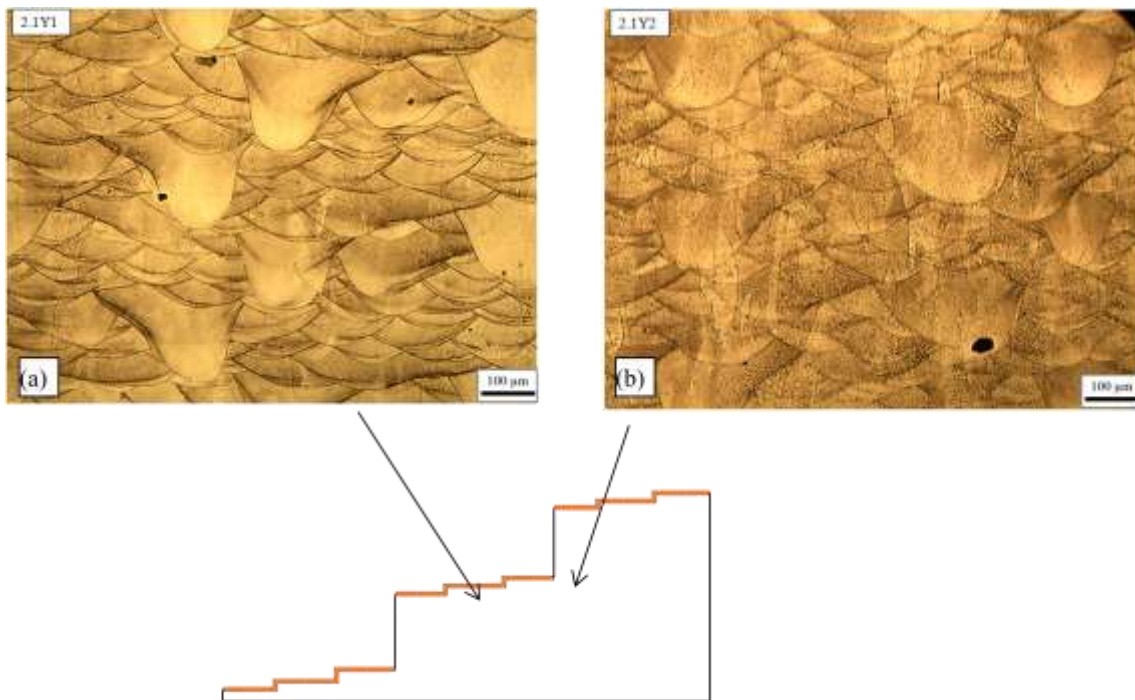


Figure 4.3: Comparison between Y plane microstructure from (a)external and (b)internal location of the part

4.1.4 Y plane: Build Height Effect

Another set of samples taken from three different steps was subjected to comparison to study build height effect. Here the horizontal position is different and each sample was taken from each major step namely 1.0Y1, 2.1Y1 and 3.1Y1. All the images shown in figure 4.4 were taken near the top surface where the powder layers do not go through too many repetitive thermal cycles. Here again the bottom sample 3.1Y1 is closest to the substrate, thus has the higher cooling rate. All the images reveal the rows of arc shaped features having different depths. Sometimes there is regular distribution of arcs of same depth, sometimes there is mixture of different depths. Usually the locations which are close to top where there is no more melting reveal more regular microstructure, but the locations inside the part can have mixed and irregular microstructure due to the fact that when a layer starts to solidify, it re-melts again. So the layers inside a part can never get solidified completely into a more defined shape. Then the cut section of that layer reveals arcs of different depths and widths. Also a deeper and larger melt pool indicates higher energy accumulation in that area. From figure 4.4, it can also be inferred that the arcs are wider in top surfaces whereas these are deeper near the bottom surface.

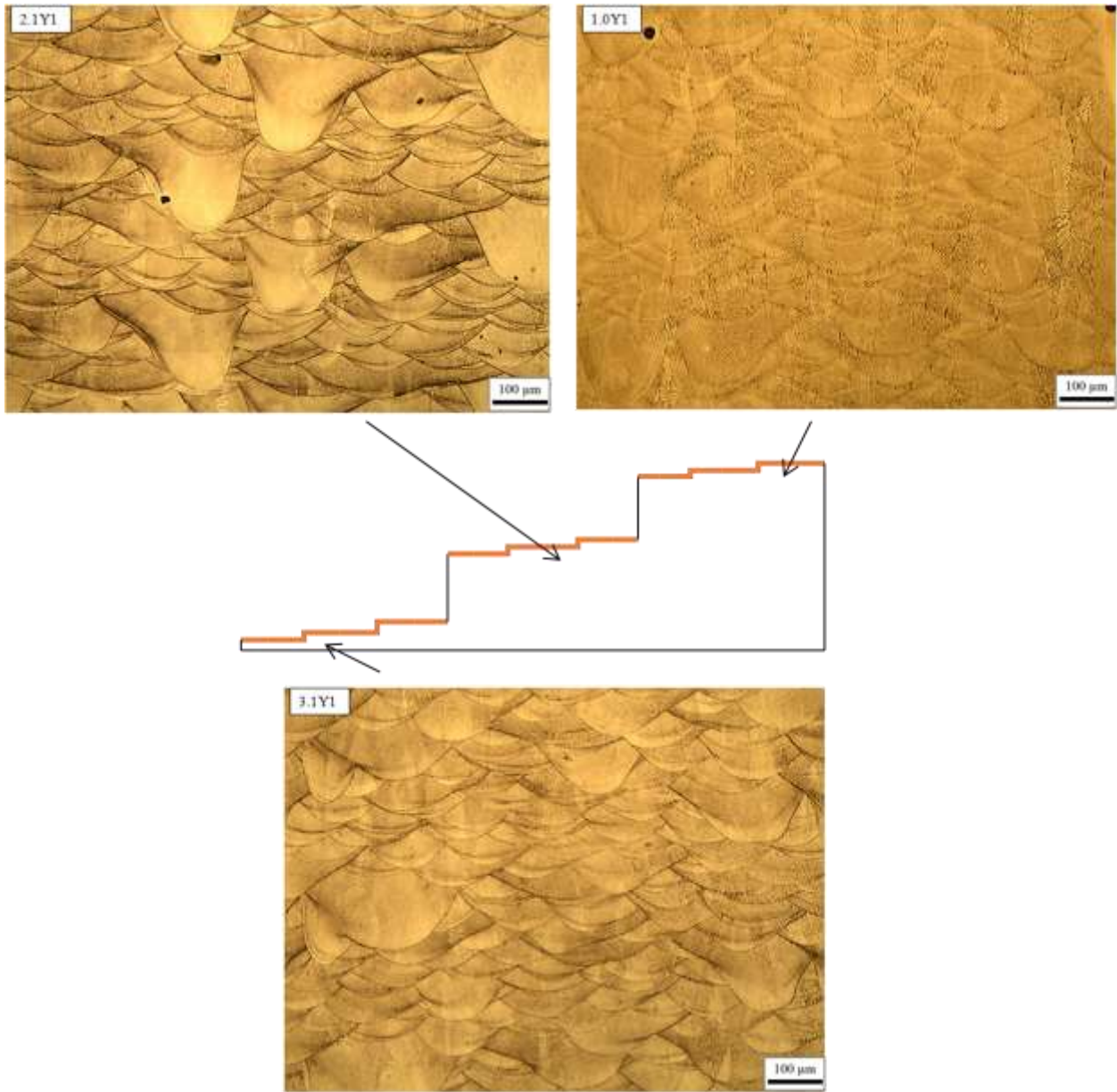


Figure 4.4: Build height effect on Y plane

4.1.5 Y plane: Bottom Surfaces

A final set of comparison shows the optical microscope images taken at same height but different horizontal positions. Since the part has staircase feature, so despite being at same height, the thermal history can be different for the samples 3.1Y1, 3.1Y3 and 1.2Y1 as shown in figure 4.5. The samples 3.1Y1 survived least number of thermal cycles since there is no more

layers after 3 mm height. The samples 3.1Y3 have similar thermal effects from re-melting and solidification. 1.2Y1 went through highest number of thermal cycles since these sample lie at the bottom of 60 mm height. From the optical microscope images, 3.1Y1 reveals shallower melt pools whereas 1.2Y1 has deeper melt pools. This gradually increasing depth can be caused by the downward heat flux. Also 3.1Y1 being near the external surface, it has more defined and regular patterns of microstructure whereas the other two samples show less regular shape and depth distribution as discussed in 4.1.3.

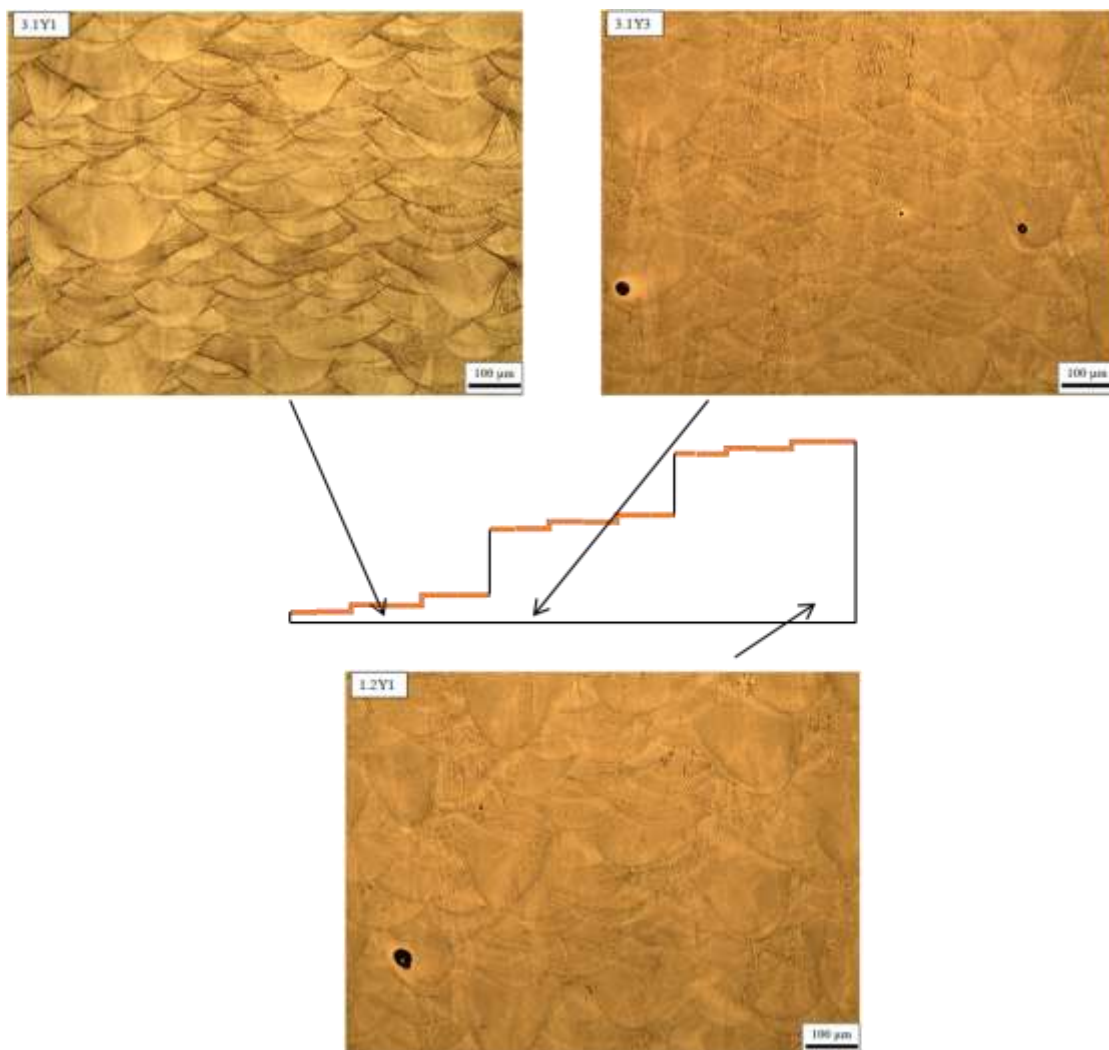


Figure 4.5 : Comparison between microstructures at the bottom of the part

4.1.6 Z Plane: General Features

Unlike the X or Y plane, Z plane reveals line by line structure instead of layer by layer structure. On the Z plane, laser melted tracks are visible caused by the scanning pattern and the individual melt pool boundaries can be observed where two adjacent tracks meet. The part was built using alternating scan vectors, so two different directions of tracks are found aligned at 90° with each other. In general, the scan vectors are aligned at 45° angle with either X or Y axis. There are overlaps between the tracks which are considered to be the higher stress concentration region, because the overlap regions face rapidly reheating and solidification process. The edge of a melted track is arc shaped which produces a deep molten pool named keyhole that is marked in figure 4.6(c). Inside the keyhole, the microstructure has dendrites which grow in random directions. Fine dendritic grain, cellular and columnar grains are present in various proportions in various locations of the specimens. These indicate rapid solidification process during SLM process. Columnar structure growing perpendicular to the melted track border can be found in the middle of the tracks as seen in figure 4.6(d).

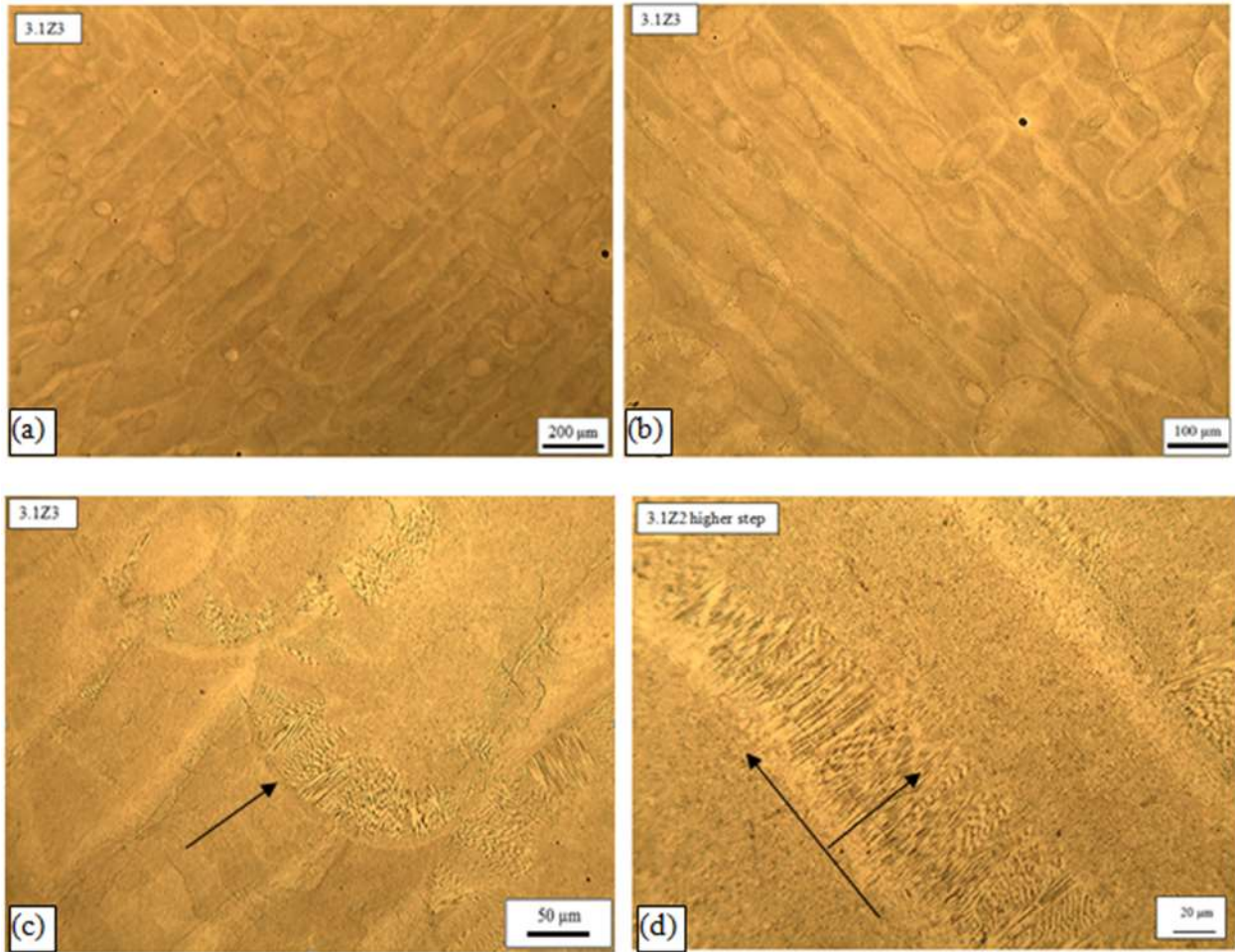


Figure 4.6: Microstructure of Z plane; (a)X50, (b)X100, (c)X200 and (d)X500

4.1.7 Z plane: Effect of Thermal Cycle

Similar to Y plane, effect of the number of thermal cycles on microstructure for Z plane has also been studied. Microstructure from different heights at same horizontal distance has been illustrated in figure 4.7. The microstructure on the very top surface in 1.0Z2 shows completely solidified rows of melted tracks as expected. There is no shifting of laser beam visible on top surface, but shifting and incomplete solidification is quite noticeable on 2.1Z3 and 2.2Z2. Also on 2.2Z2, there are areas where two melted tracks at 90° angle overlap each other (indicated by arrow). This type of feature basically shows the adjacent layers where one lies on top of another. 2.2Z2 is closer to the substrate than 2.1Z3, so the cooling rate is higher in 2.2Z2. Incomplete

solidification of track is more visible on 2.1Z3 than on 2.2Z2. The arrow on 2.1Z3 shows a track which is resulted from incomplete solidification into a continuous shape. Since the cooling rate is lower here, so this feature is expected at the middle of the part.

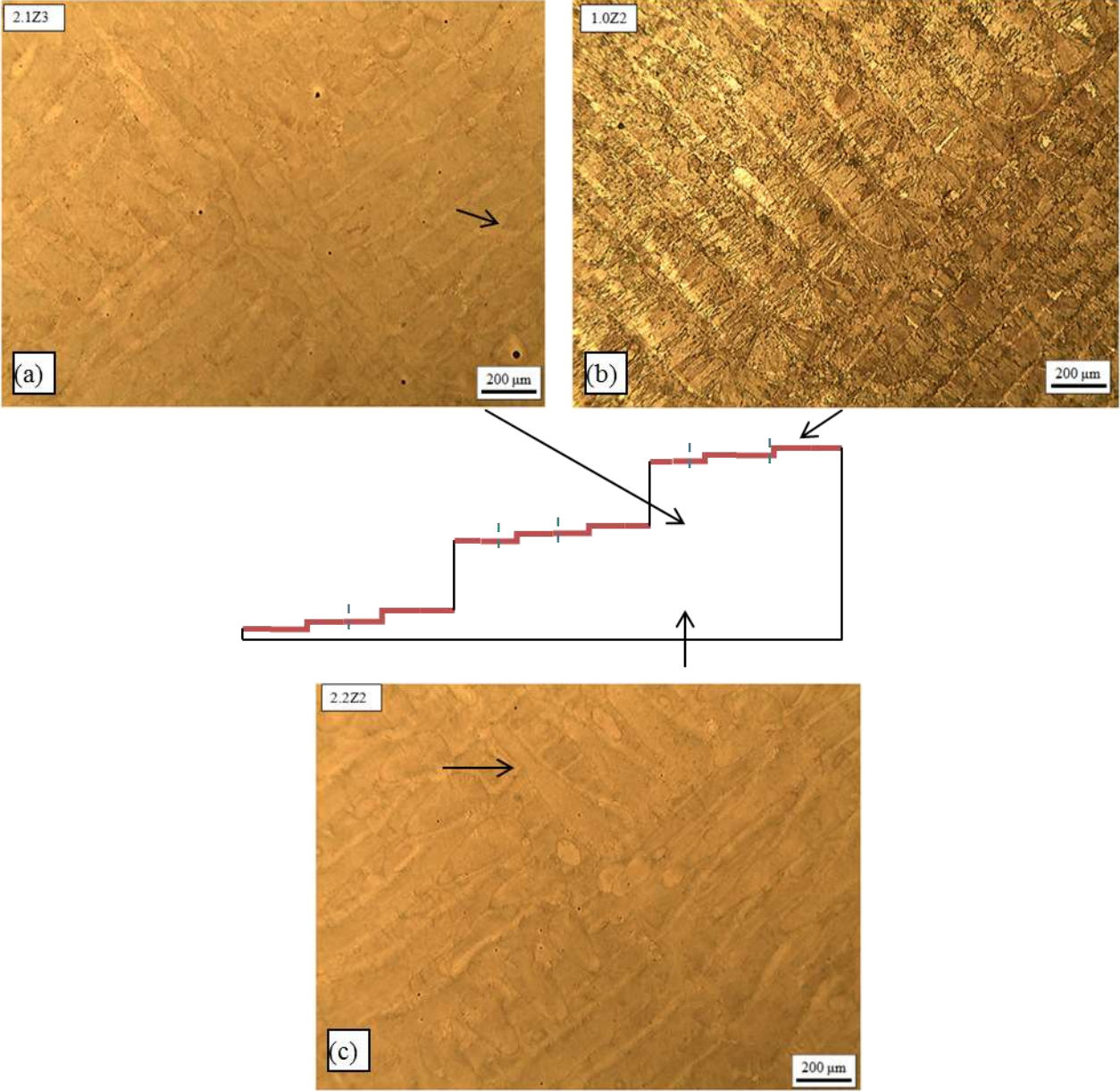


Figure 4.7: Effect of thermal Cycle on Z plane

4.1.8 Z plane: External and Internal Surfaces

The difference between microstructure in external and internal surfaces should be more detectable on Z plane considering the fact that there is no more layers on the top of external surface. The comparison between two specimens from external and internal surface of Z plane of the part has been shown in figure 4.8. Figure 4.8(a) is the microstructure of a specimen taken from the top surface of a step and figure 4.8(b) is showing the microstructure of a specimen which lies inside the part. As expected, it is more obvious in Z plane that the microstructures are different in those two locations due to different thermal phenomena. In the microstructure of the top surface, the border between two groups of tracks of different directions is quite visible. The edge of each track is also clear and the pattern is repetitive. In the specimen inside the part which has been through repetitive thermal cycle of reheating and solidification, the melted tracks do not show clear border and are not exactly same. There are keyhole features here and there which may indicate the cross section of a melt pool. The rows of keyholes on the inner surface indicate shifting of the laser beam along that line.

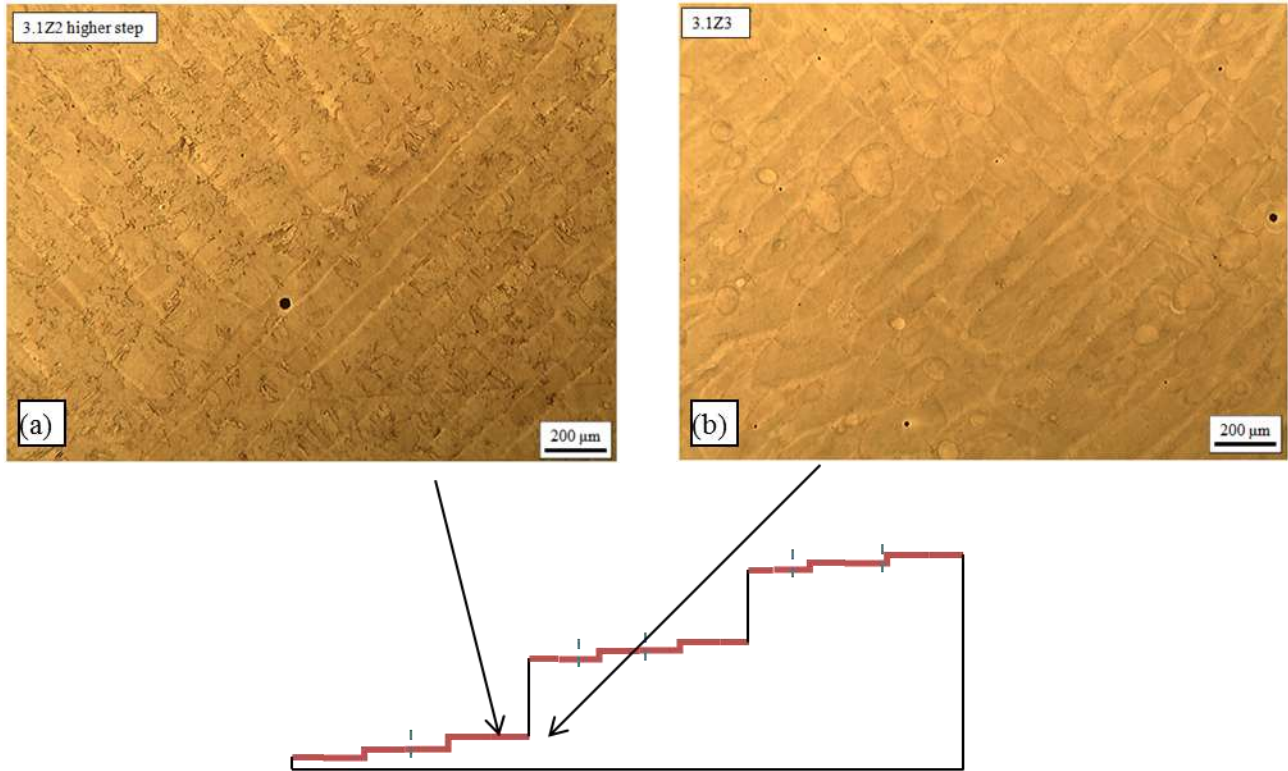


Figure 4.8: Microstructure of 2 specimens at (a) external and (b) internal surface

To have a better understanding of the microstructure, scanning electron microscopy has been used to get images in even larger magnification. Figure 4.9 presents different SEM images of Z plane microstructure taken from top surface and inside surface. All of the images were taken where two melted tracks meet. The top surface shows much defined overlap position whereas the surface inside does not have any strong presence of a border. The white area is much likely to be Laves phase which makes the material brittle, hence undesirable. The Laves phase on inner surface seems irregularly shaped and higher in concentration which might cause decrease in mechanical properties compared to external surface.

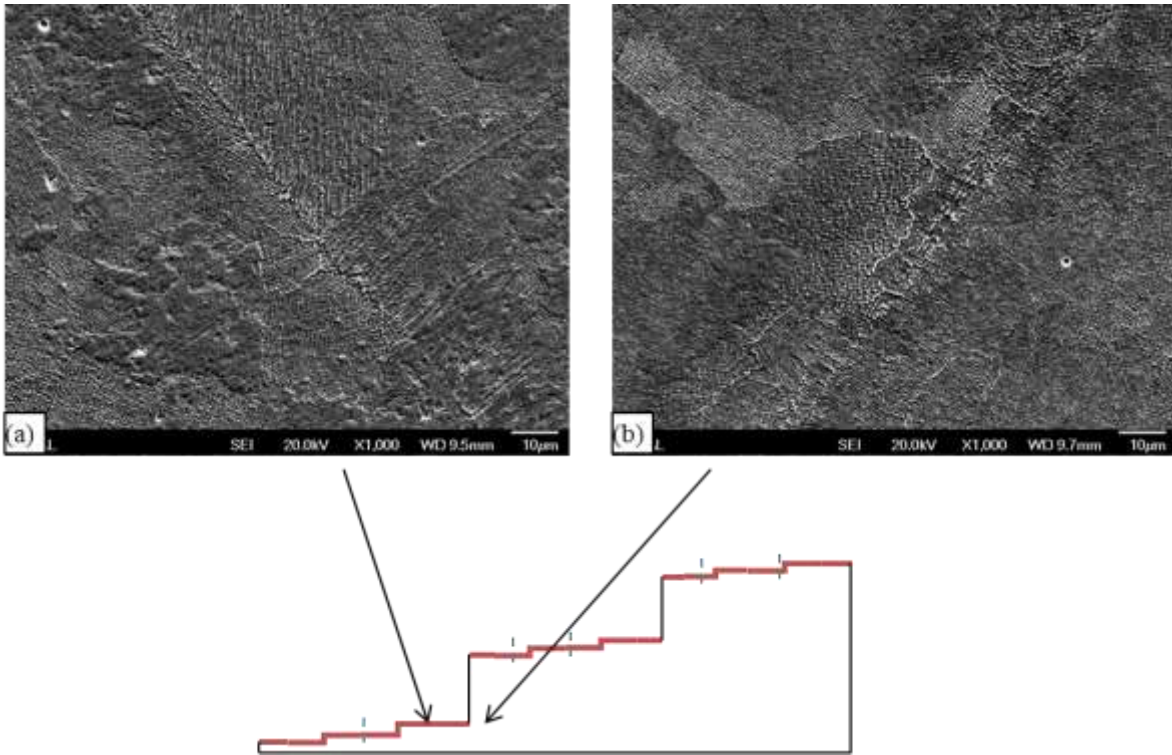


Figure 4.9: Comparison between SEM images taken at (a)external and (b)internal surfaces

To see the scanning patterns more clearly, a comparison between images of microstructures taken using stereoscope in internal and external surface has been illustrated in figure 4.10. 2.1Z2 shows the microstructure at the very top of a major step where the polishing removed less than $60\ \mu\text{m}$ height worth material. So, it indicates the very last layers of powders which were solidified completely and the microstructure clearly reveal $5\text{mm}\times 5\ \text{mm}$ island scanning. But 2.1Z3 which is inside the part and have been through repeated melting and solidification, does not show the scanning pattern very clearly. The microstructure consists of smaller squares of $\sim 1.15\text{mm}$ length. This can be indicative to the shifting of the laser beam on each layer.

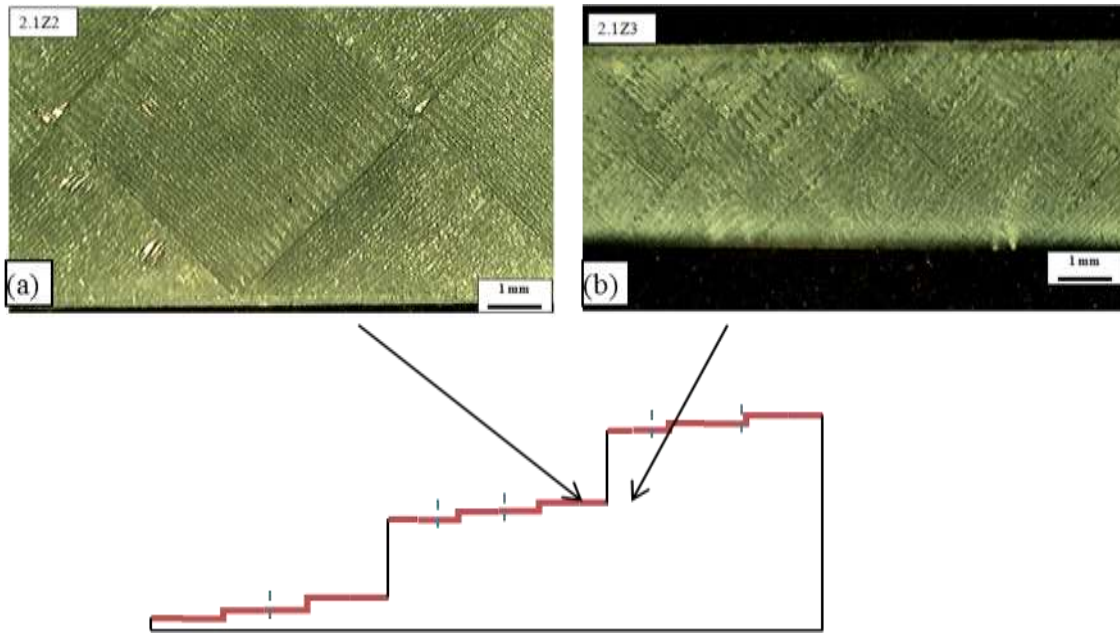


Figure 4.10: Comparison of (a) external and (b) internal surfaces at 10X magnification

4.1.9 Z plane: Build Height Effect

Figure 4.11 shows the microstructure of different specimens taken from three different heights of the part. All the images were taken at the top of the part and these reveal very clear features. The melted tracks are defined and have an average width of $\sim 100\text{-}150\ \mu\text{m}$. Sample 3.1Z2 is closest to bottom and hence the substrate. Despite having different cooling rate, the average width of melted tracks is more or less equal at different heights. The tracks are aligned at 45° angle with X and Y directions. At the edge of each track, the width is higher ($\sim 250\ \mu\text{m}$ at keyhole), then gradually it gets thinner towards the center.

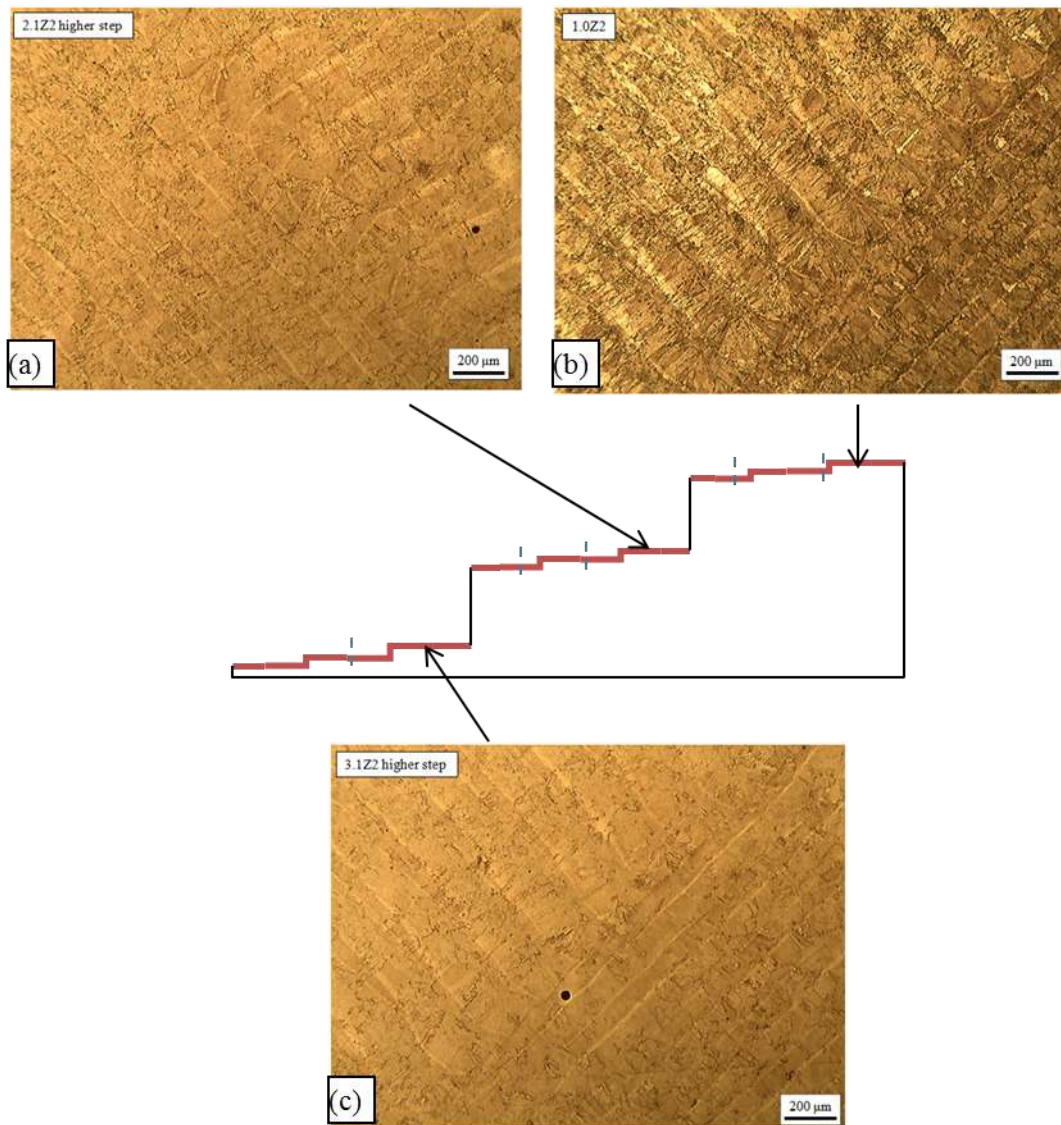


Figure 4.11: Microstructure of top surfaces at different build heights

A comparison between microstructures taken from different build heights has been shown in figure 4.12. All the images were taken at overlap positions. In all 3 different heights, the border of an overlap is quite defined. There are dendritic grains which grow perpendicularly with the border of a track. But the amount of the grains and precipitates seems to be different in different build heights which may contribute to the difference in metallurgical bonding, thus mechanical properties. The number of voids in figure 4.12(a) seems higher than the other two which can cause ductile failure. The distribution of laves phase and γ dendrites are also not the

same in three different build heights. Laves phase reduces mechanical properties since it is an intermetallic, brittle phase, hence is undesirable [4].

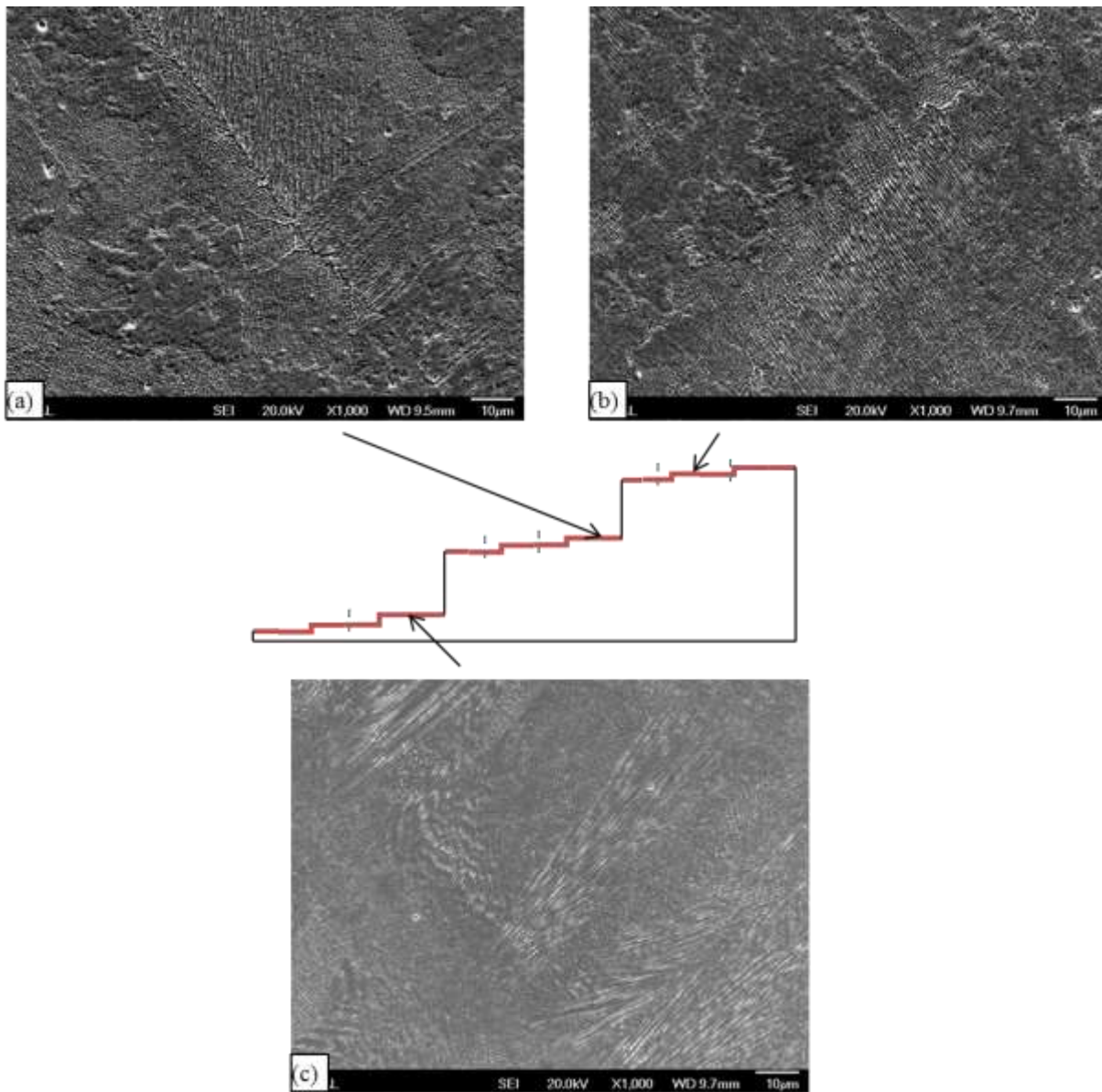


Figure 4.12: Comparison between SEM images taken at different build heights

4.1.10 Z plane: Bottom Surfaces

A comparison between microstructures in the bottom of the part has been shown in figure 4.13. The microstructures are in the same height, but different horizontal distance. 3.1Z2 is on the top of a staircase, so it has very clear and defined microstructure due to complete

solidification. 3.1Z3 and 2.2Z2 are inside the part, so there is space between two adjacent melted tracks and rows of rounded keyholes. The rows of keyholes usually indicate a shifting of the laser beam (indicated by arrow). The microstructures of 3.1Z3 and 2.2Z2 are quite similar since both of these have similar thermal history. Both of the samples were subjected to repeated melting and solidification due to the layers above them. All three samples are close to the substrate, thus have higher cooling rate compared to areas higher than these.

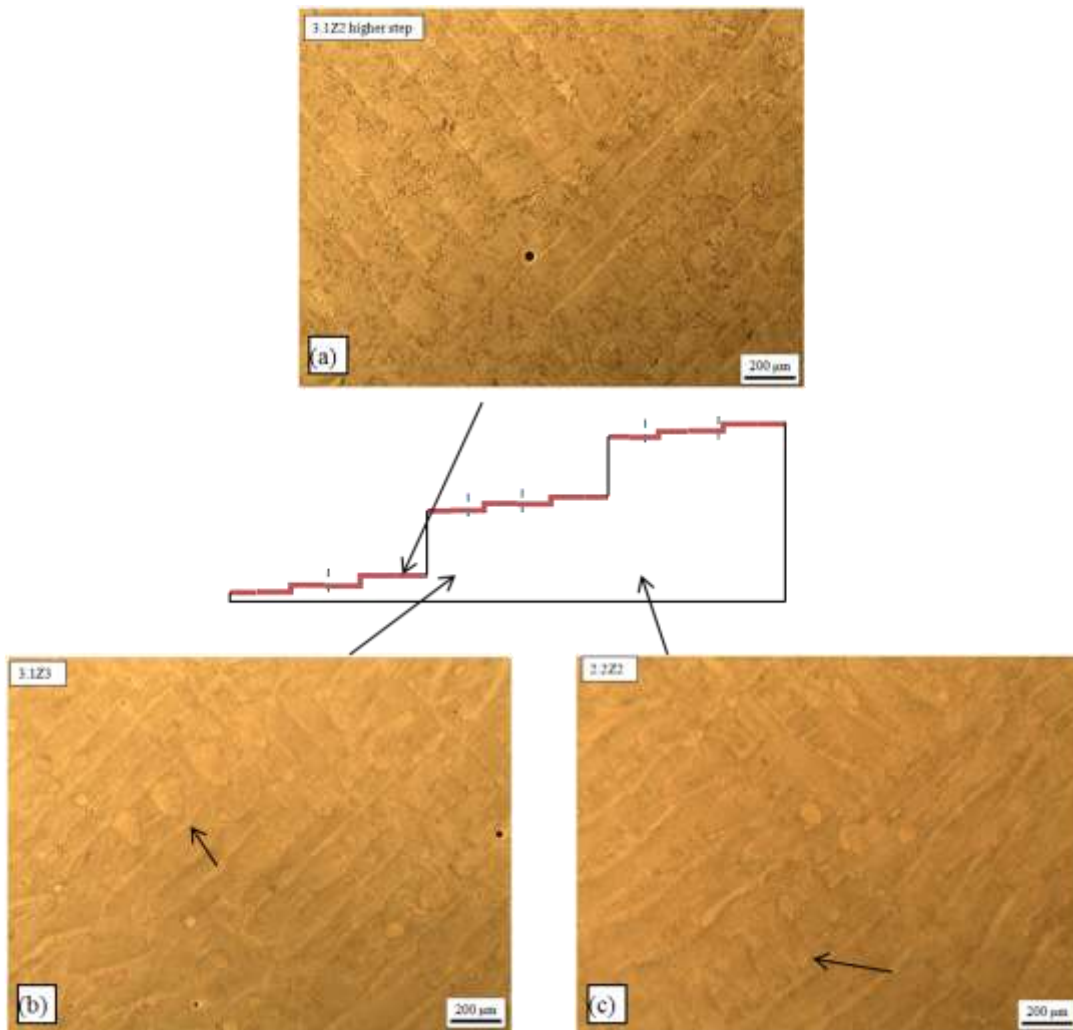


Figure 4.13: Comparison of microstructure at the bottom of the part

4.1.11 X plane

X plane and Y plane both can be considered as side or front surface. Because of the scanning strategy, it is generally assumed that the microstructure is more or less identical in both of the surfaces. To prove that hypothesis, a brief analysis has also been performed on X plane as well. So, similar procedure has been followed to reveal and observe the microstructure of X plane sample to compare with Y plane microstructure. It was found that the results are quite same for both X and Y plane as shown in figure 4.14. X plane also reveals the arc shaped cut sections of melt pools of different depths. The slight difference of microstructure between Y and X plane is caused by the different location of the samples in the part. 2.1Y1 represents the front of the part while 2.1X1 represents the side surface. In both of the samples, it can be observed that there are several columns of shallow melt pools. Where the shallow melt pool columns end, the columns of deeper melt pools begin. In higher magnification, both of the samples show columnar grains growing towards build direction in figure 4.14 (e) and (f). Also the dark band of intermetallic phase is very prominent at the border of every melt pool at both of the planes.

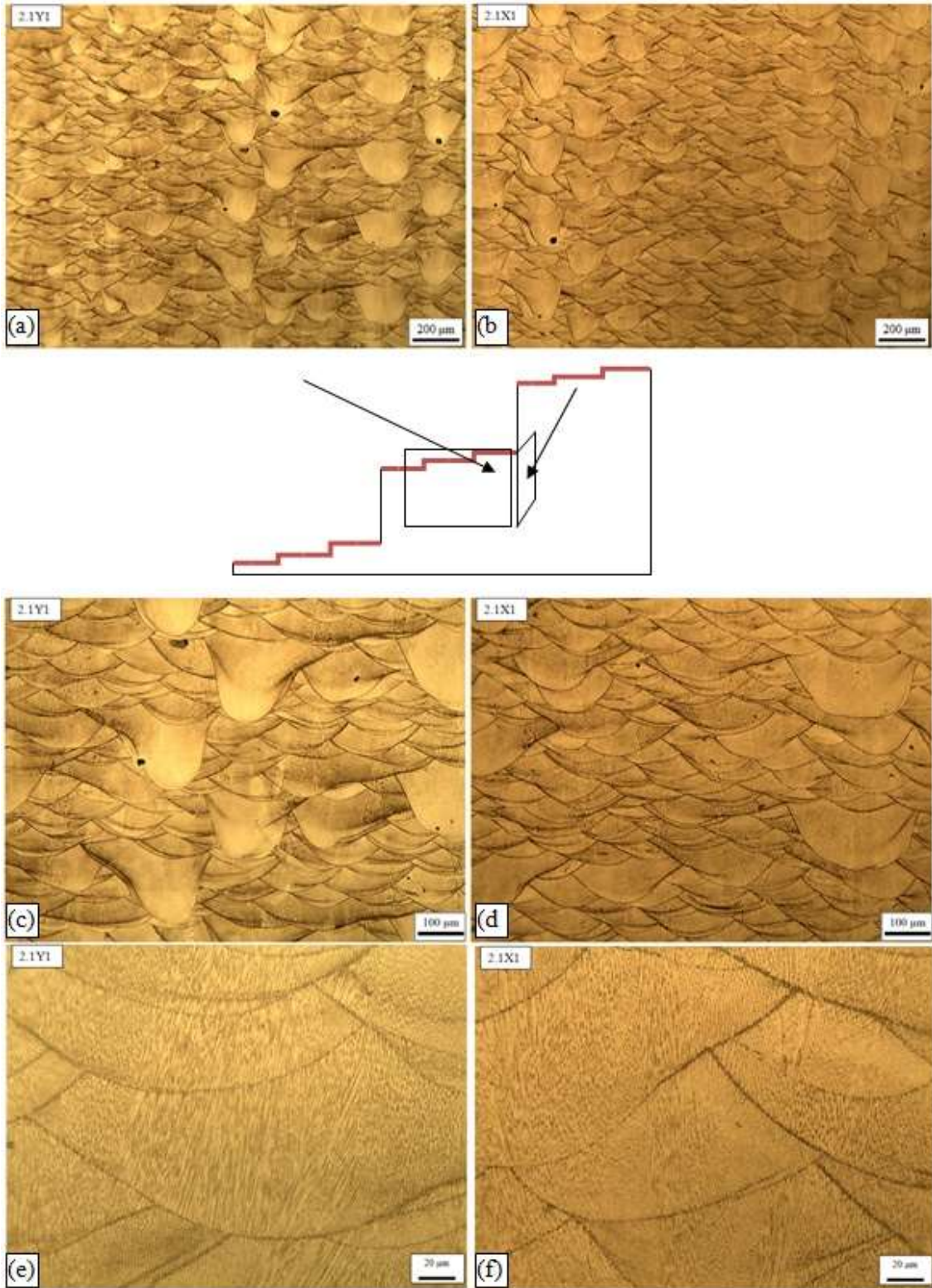


Figure 4.14: Comparison between Y and X plane at different magnifications

Since the main objective of this study is to observe build height effect, so a comparison between microstructures from different build heights for X plane has also been shown in figure 4.15. As seen for Y plane, there is no significant variation in the microstructure with build height. There is mixture of arcs of different depth in top samples, whereas in middle and bottom area, the distribution of narrow and deep arc is more organized. The top sample 1.0X2 seems have lesser amount of dark intermetallic compound at the borders of melt pools even though these were etched with the same solution for same amount of time at same temperature.

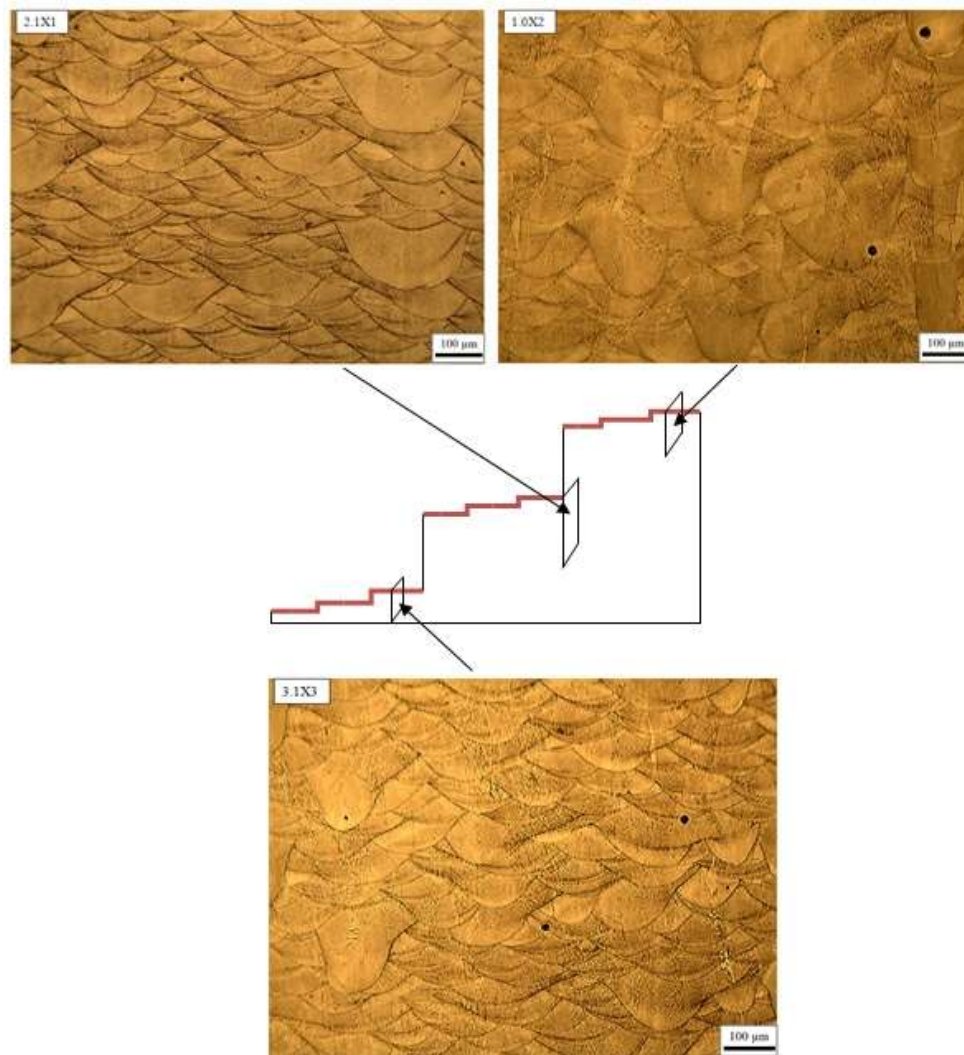


Figure 4.15: Comparison between X plane microstructure from different build heights

The microstructure of X plane was further observed for higher magnification using Scanning Electron Microscopy (SEM). SEM images reveal the columnar grains as shown in figure 4.16. The growth direction of the fine γ dendrites is almost parallel to the build direction. At higher magnification, the primary dendrite arm spacing is found to be $\sim 1 \mu\text{m}$. Since the cutting plane is not completely parallel to Z axis, so some cut sections of dendrites are also visible which grow in slightly tilted directions. The columnar grains growing through several melt pools cause the metallurgical bonding between the layers.

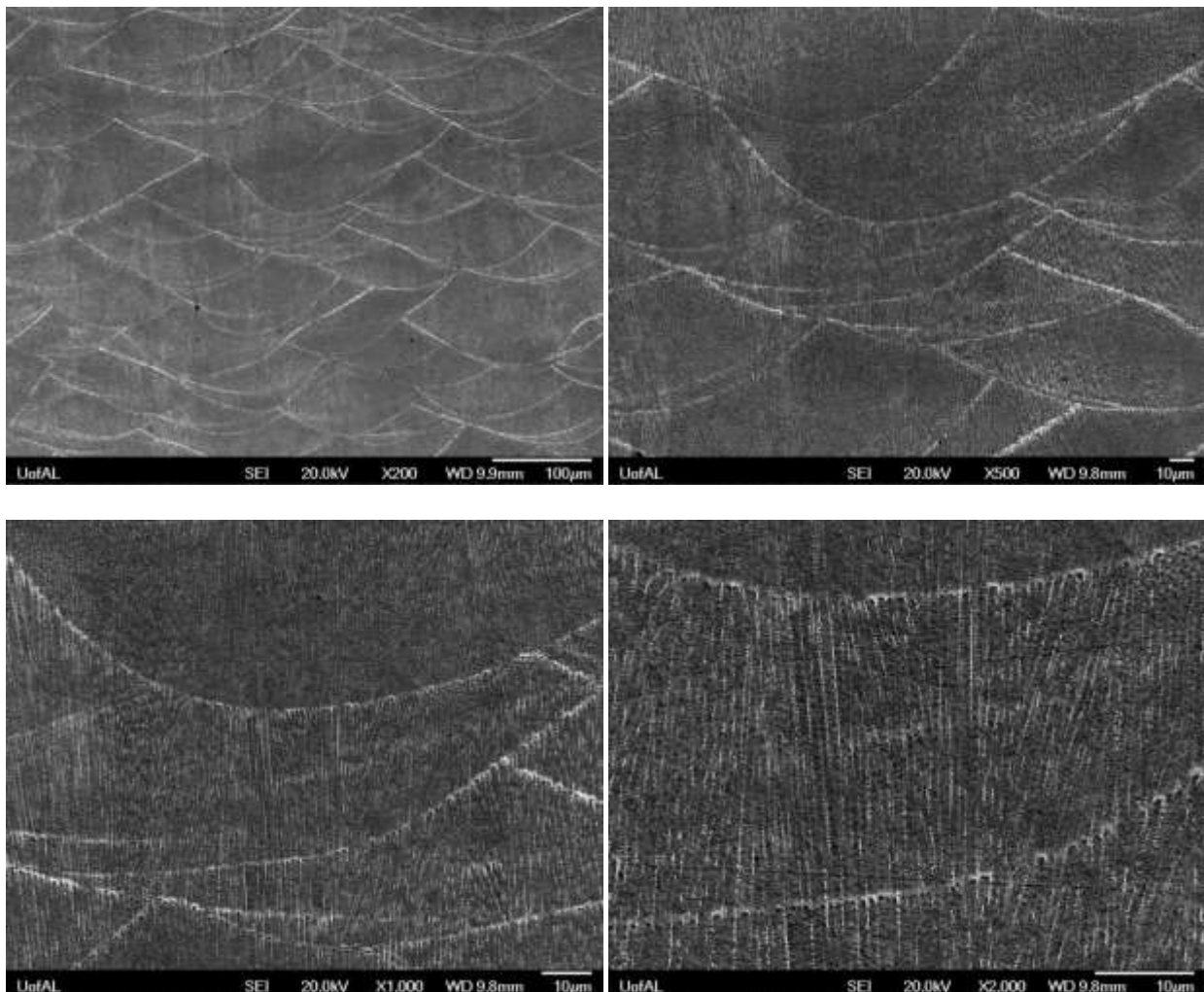


Figure 4.16: SEM images for X plane sample

4.1.12 Summary: Comparison between X, Y and Z planes

The microstructure generated in all three planes of the part is greatly influenced by the scanning pattern and strategy. The top surface at Z plane reveals the laser melted tracks whereas the side surface at X plane and the front surface at Y plane reveal cut sections of those melted tracks. A comparative illustration of microstructures of all three planes has been presented in figure 4.17. The observations can be summarized as follows:

- The front surface (2.1Y1) and side surface (2.1X1) are quite similar in terms grain shape, size and orientation. Both consist of columns of shallow and deep arcs which indicate the layers of laser melted tracks.
- The top surface at 2.1Z2 reveals the scanning pattern. The edges of laser melted tracks are rounded and larger in diameter which is called 'keyhole'. The keyhole feature reflects in the deeper arcs in X and Y plane. The diameter of the keyholes are $\sim 200 \mu\text{m}$ and the width of the deeper arcs are also $\sim 200 \mu\text{m}$.
- Similarly, the shallower arcs are the cross sectional borders of the middle of the tracks on Z plane. The depth of the shallow arcs and the width of melted tracks are $\sim 150 \mu\text{m}$.

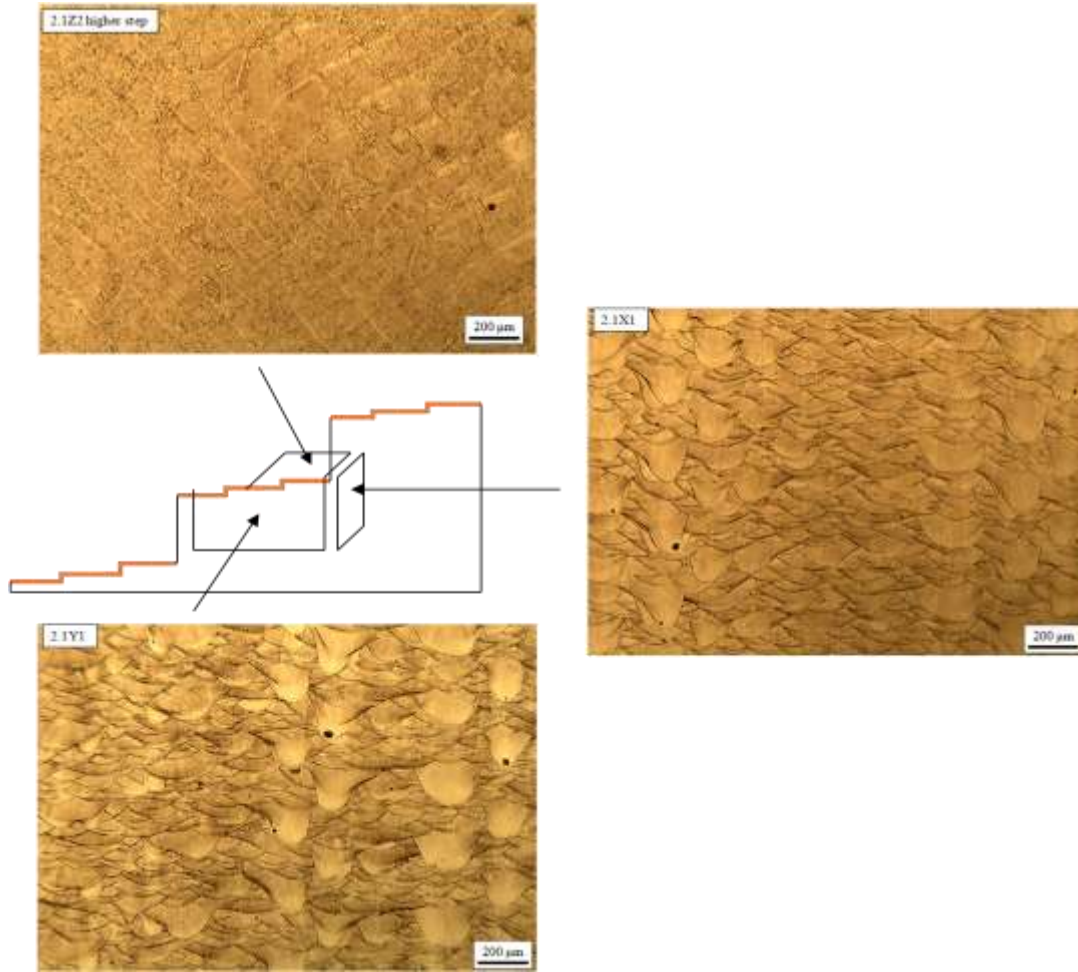


Figure 4.17: Comparison between X, Y and Z plane

The microstructure of Y and Z plane was studied in 4 different comparison groups. For Y plane, the microstructure was observed using optical microscope and the observations can be summarized as follows:

- The microstructure consists of columns of concave arcs of various depth which are induced by the heat transfer direction towards the bottom. The arcs represent the cut sections of melt pools. Each laser melted track has a rounded front and prominent tail which have a cross section in the form deeper arc. The shallower arcs represent cross section of somewhere at middle of the melted tracks. So the microstructure of Y plane is helpful to determine the depth of the melt pools.

- OM images of microstructure taken at different build heights at same horizontal distance reveal very slight difference in terms of depth of melt pools. The number of deeper melt pools seems to be higher near the bottom surface due to continuous re-melting and downward heat flux. Also, the border of each melt pool gets preferentially etched revealing the presence of dark intermetallic particles. The dark bands seem to be more intense at the middle of the part.
- The external and internal surface of a stair at the same height were compared since there is no more melting at the top of the external surface. Even though the difference is more noticeable on Z plane, Y plane reveals that the distribution of melt pool arcs are regular and defined on external surface than internal surface.
- Microstructure near the top surface of each step was also observed and compared. The middle step contains higher amount of dark intermetallic phase at the border of the melt pools which get preferentially etched. Also, it has deeper arcs compared to the top and bottom step.
- The surfaces near the bottom under each step were compared due to the fact that they went through different number of thermal cycles. The depth of melt pool increases from left to right as it goes from surface under lowest step to surface under highest step. It can be caused by continuous downward heat flux near the bottom of the part under 1st (highest) step.

Microstructure of Z plane was studied using both OM and SEM for the same comparison groups. The key points from this study are listed below:

- OM images of Z plane microstructure reveal the scanning pattern. There are laser melted tracks in two different directions at 90° due to island scanning strategy. There is also overlap

between two adjacent tracks and round edge at the front and tail of each melt pool. Large amount of heat gets accumulated in the round 'keyhole' feature and creates deeper melt pool.

- No difference is observed between the surfaces under 1st step, but the top surface is different compared to the surfaces under that. The laser melted tracks are defined on the top of the part since there is no more melting after that layer. But the edges of the tracks are not defined at the middle and bottom of the part due to incomplete solidification. Broken tracks and overlapping of two tracks at right angle are visible at the middle and bottom of the part. Also the cooling rate is higher near the bottom due to the solid substrate.
- Difference between external and internal surface is very clear on Z plane compared to Y plane. The external surface is defined and organized due to the absence of re-melting, but internal surface contains broken tracks, cut sections of keyholes from upper layers and lack of definition of the laser melted tracks. SEM images also reveal the clear line where two tracks meet on external surface. Stereoscope images at lower magnification showed shifting of laser beam on internal surface.
- The top surface of each major step was studied and compared using OM and SEM. No specific difference can be found between these surfaces due to the fact that all of them are essentially parts of the top surface of the entire part. All of the surfaces consist of very defined and clear melted tracks with keyholes at the edge. The width of the tracks look more or less similar on all the steps. SEM images showed the overlap of two tracks very clearly. Dendrites grow at a perpendicular direction to the border of the tracks. The top surface of the lowest step contains dendrites and cellular structure growing in different directions which is caused by higher cooling rate.

- Surfaces near the bottom at the same height were observed using OM. The surface from lowest step is taken from the top of the step, so it looks different being an external surface than the surfaces under other two steps. The surfaces under middle and highest step contains less defined melted tracks, keyholes from upper layers and shifting of laser beams. These two surfaces do not reveal any difference since both of them have been through similar thermal history. The height of the steps and thus the number of layers of each step are different, but the melting of the surface which is at a height over 30 mm, does not affect the surface under 1st step which is close to bottom.

Samples were taken and observed from X plane to compare with Y plane. The microstructure on X plane looks same as Y plane. SEM images have also been taken which revealed possible presence of Laves phase or δ precipitate along the border of melt pool. Also, γ dendrites grow along the build direction which is caused by downward heat transfer.

4.2 Mechanical Properties

4.2.1 Nanoindentation test: General Discussion

Mechanical properties were measured using nanoindentation process with Hysitron Triboindenter and Agilent technologies Nanoindenter G200. Nanoindentation with 100 nm (Triboindenter) and 20 nm (Nanoindenter G200) Berkovich tip provides Young's modulus and hardness. Also, it shows the force-displacement curves using which the properties are calculated. An example of a set of nanoindentation tests performed in Triboindenter is shown in figure 4.18. The plot consists of 16 overlapping curves obtained from 16 nanoindentations made on a specific area of a sample. The 16 points were 5 μm apart from each other forming a 4 \times 4 square grid pattern. As discussed in section 3.4, the force gradually goes from 0 to 5000 μN in 5 seconds which makes the upward segment of each force-displacement curve, then stays there for 2

seconds which makes the horizontal segment of each curve and then goes back to 0 μN in another 5 seconds which makes the remainder of the curve. According to the example shown in the figure 4.18, the average maximum indentation depth was ~ 179 nm at ~ 5000 μN force.

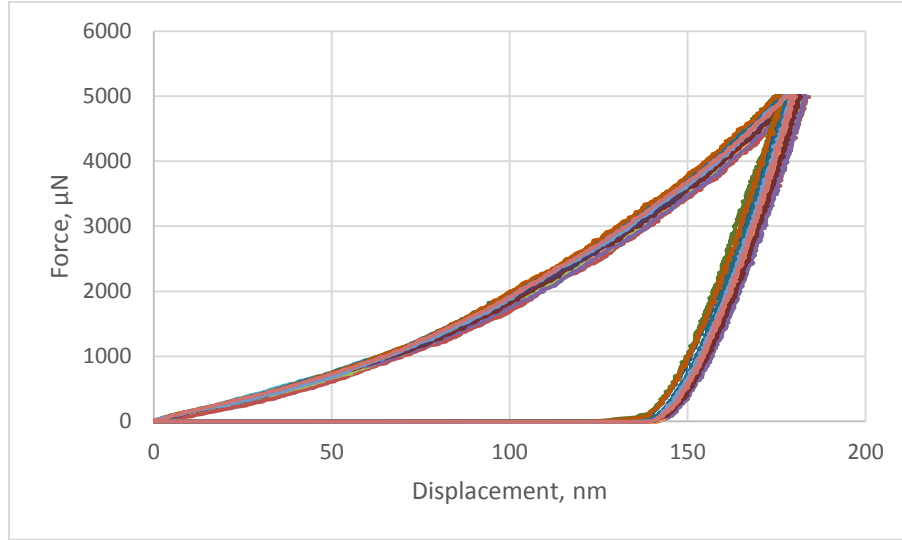


Figure 4.18: Force-displacement curves from Triboindenter

The nanoindentation results give the reduced Young's modulus, E_r . The reduced modulus, E_r accounts for the fact that the measured displacement includes contribution from both the specimen and the indenter. E_r is given by [5],

$$\frac{1}{E_r} = \frac{1-\nu_i^2}{E_i} + \frac{1-\nu_s^2}{E_s} \quad (4.1)$$

where ν_i is the Poisson's ratio of indenter, 0.07, E_i is the Young's modulus of the indenter, 1140 GPa, ν_s is the Poisson's ratio of Inconel 718 samples, 0.294 and E_r is the Young's modulus of the Inconel 718 samples directly obtained from the tests.

The hardness is calculated by following equation:

$$H = \frac{P_{max}}{A_r} \quad (4.2)$$

where P_{max} is the maximum load applied and A_r is the residual area left by the indenter which is evaluated from the shape function of the indenter and the maximum indent displacement.

The results shown in figure 4.18 were obtained from nanoindentation tests on 3.1Y1 and the mechanical properties were as follows:

Table 4.1: Example output of Triboindenter

	Reduced Young Modulus, E_r (GPa)	Hardness, H (GPa)
Mean	166.42	5.41
Standard Deviation	8.11	0.1700

The actual Young's modulus for Inconel 718 calculated from the given value by the Triboindenter is 177.8747 GPa which is obtained using equation (4.1).

An example of nanoindentation tests performed in Nanoindenter G200 is shown in figure 4.19. The calculation is same as Triboindenter. There are slight differences in the curves compared to Triboindenter results.

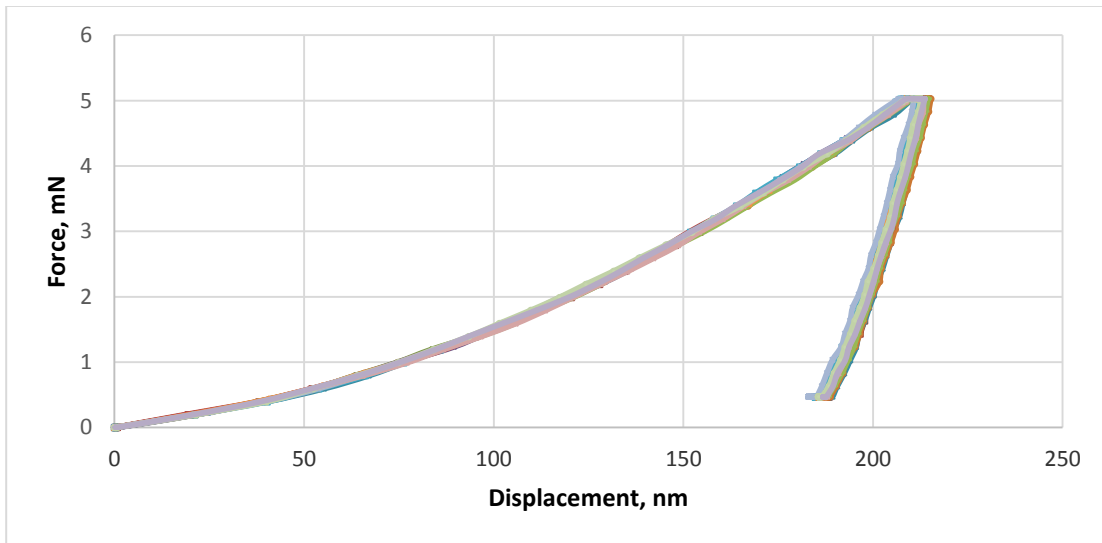


Figure 4.19: Force-displacement curves from Nanoindenter G200

A comparison between force-displacement curves obtained from both of the equipments is shown in figure 4.20. The displacement is much higher in Nanoindenter G200 where a Berkovich tip 20 nm was used. There can be several factors affecting the results:

1. Different tip diameter: The material has some porosity. A larger tip captures higher number of pores than a finer tip. So, the larger tip can give lower Young's modulus than finer one. If a material with porosity P has Young's modulus E , then

$$E = E_0(1 - aP)^n \quad (4.3)$$

Where E_0 is the Young's modulus with 100% density, a and n are material constants which depend on the grain morphology and pore geometry of porous material [26].

2. Different equipment: Two different machines have different compliance and different transducer constants which affect the results greatly.

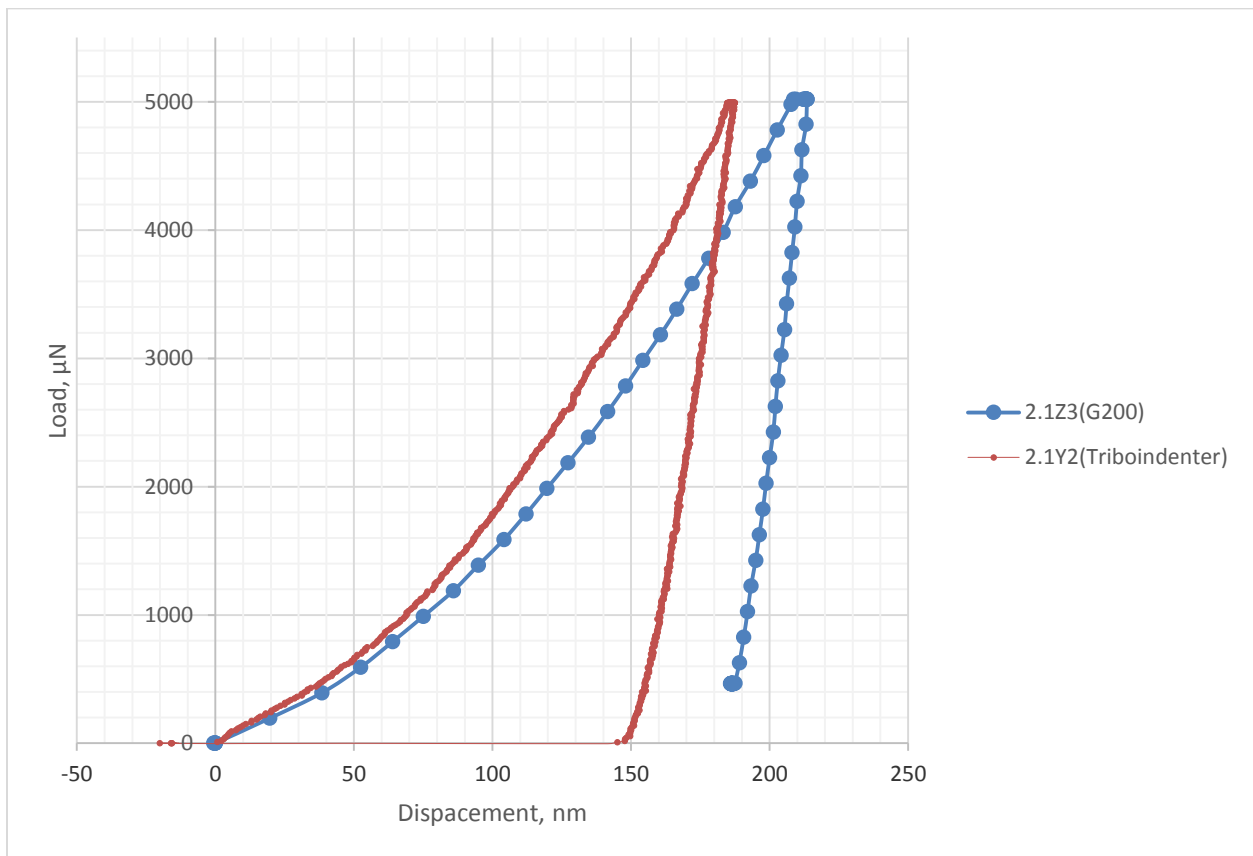


Figure 4.20: Comparison between curves obtained from two nanoindenters

4.2.2 Y plane: Effect of Thermal Cycle

Similar to microstructure study, several sets of comparison in mechanical properties have been studied for different locations of the part. The first set of comparison is shown in figure 4.21 and 4.22. The plots show mechanical properties in different heights but in same horizontal distance. From the plot, the bottom sample 1.2Y1 has a Young's modulus of 188.78 GPa and hardness of 5.8875 GPa which is the highest among all 3 locations. The topmost sample 1.0Y1 has the lowest Young's modulus of 165.35 GPa and hardness of 5.05 GPa. The sample 1.1Y1 lies in the middle of the part and has mechanical properties lower, but close to that of the bottom sample. The sample which is close to the bottom is close to the substrate as well. The lower temperature on the substrate helps to speed the cooling process up and causes faster solidification. This thermal phenomena result in finer dendrites in the microstructure, thus higher mechanical properties.

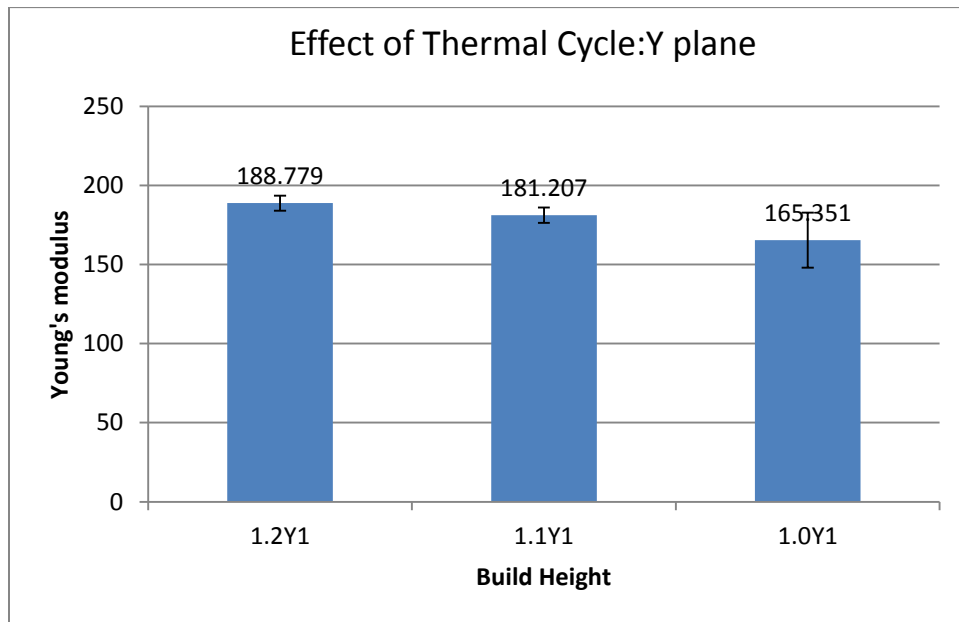


Figure 4.21: Comparison between Young's moduli for different thermal cycles

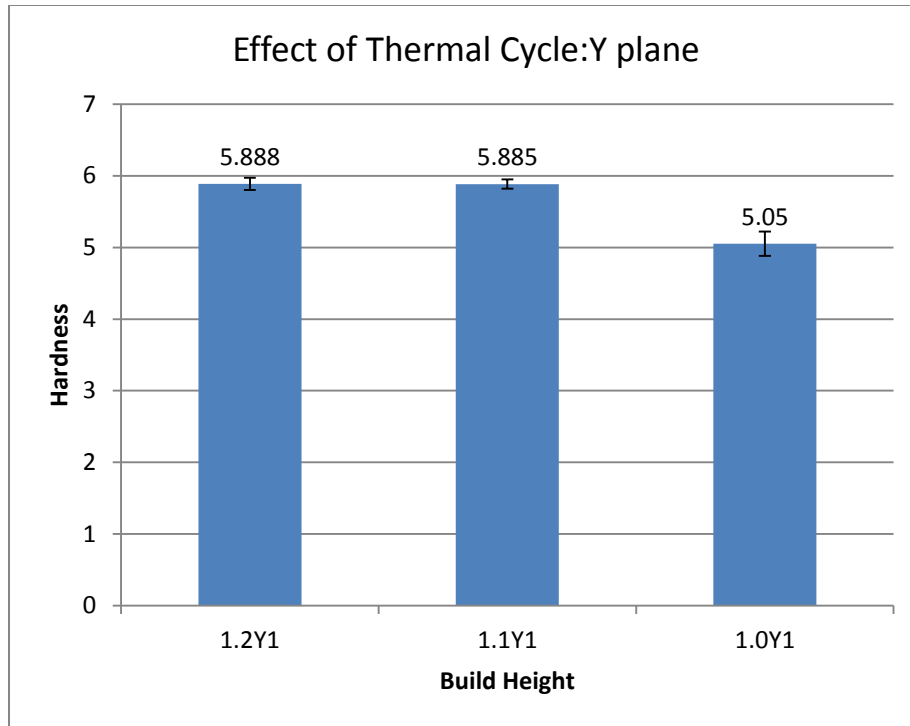


Figure 4.22: Comparison between hardness for different thermal cycles

4.2.3 Y Plane: External and Internal Surface

Since the microstructure significantly varies between external and internal surfaces, it can be expected that mechanical properties will also follow the same trend. From figure 4.23, it can be observed that the Young's modulus is slightly higher in internal surface while it is lower on external surface even though it has higher standard deviation. As far as the hardness is concerned, it is noticeably higher on internal surface and lower on external surface. The optical images revealed larger amount of dark bands on the borders of melt pools in external surface as shown in figure 4.3. The dark bands consist of intermetallic particles which make the part mechanically weaker. That justifies the higher Young's modulus and hardness on the internal surface than the external surface.

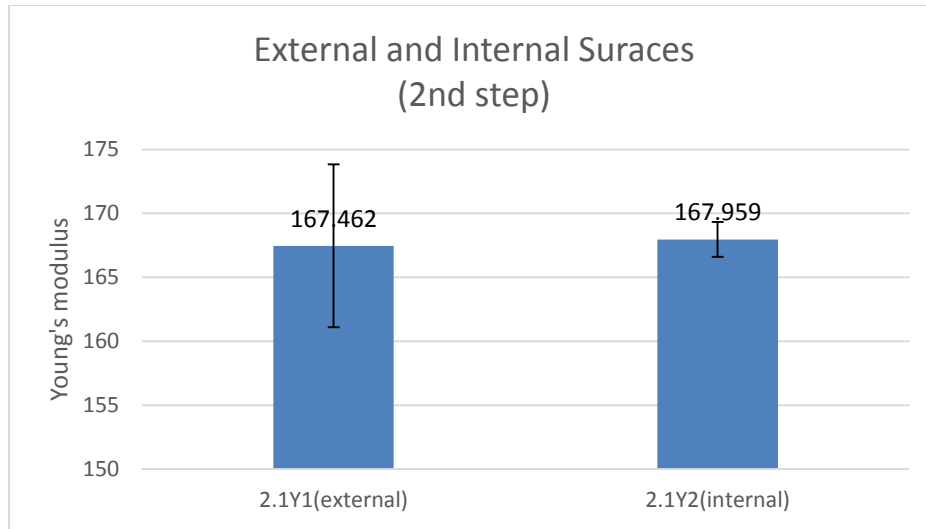


Figure 4.23: Comparison between Young's moduli of external and internal surface

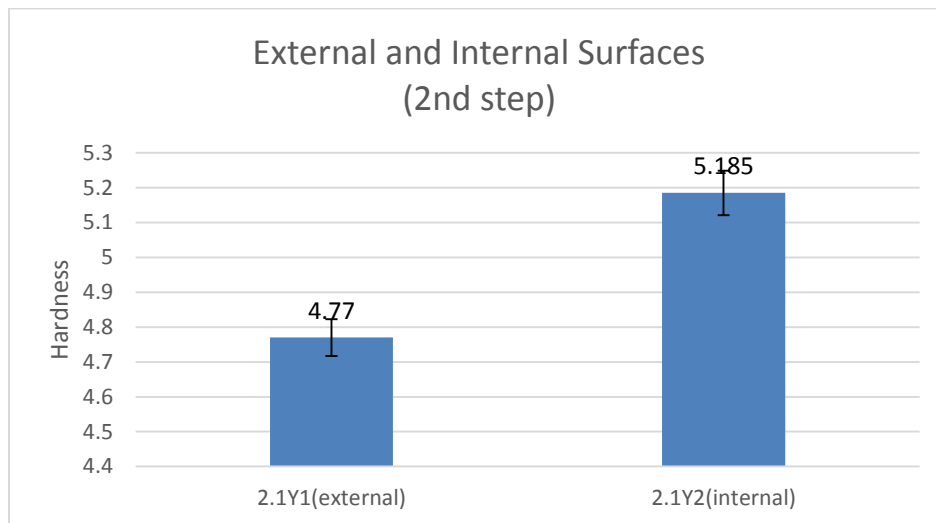


Figure 4.24: Comparison between hardness of external and internal surface

Same comparison was made for 3rd step too. Figure 4.25 and 4.26 show the mechanical properties of top surface of 3rd step which is the external surface and another surface inside the 2nd step which is at the same height of the external surface. Here the trend is opposite to what we observed in 2nd step. This can be explained from a different point of view. The external surface is exposed to relatively colder powder particles where no more melting occurs on top of the surface

and it causes higher cooling rate, thus finer grain size. This might contribute to the higher mechanical properties in the external surface.

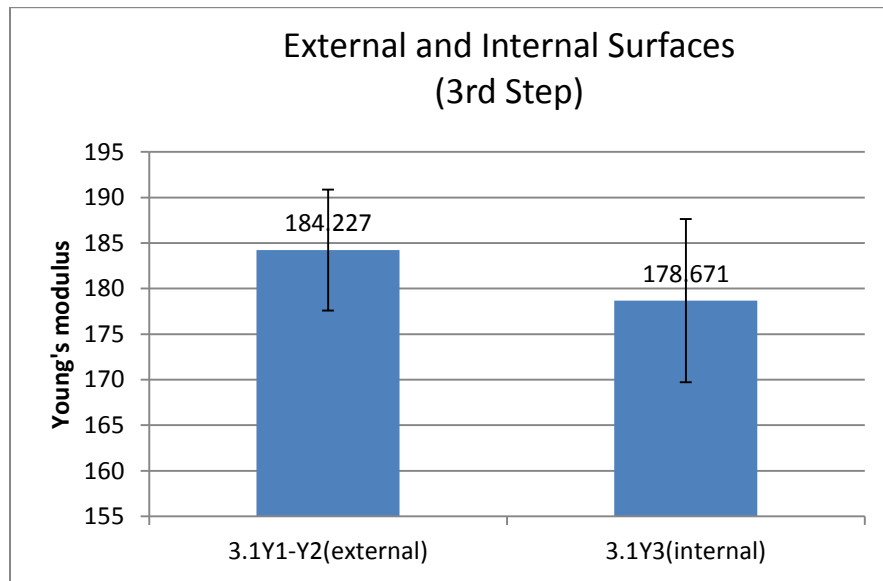


Figure 4.25: Comparison between Young's modulus of external and internal surface

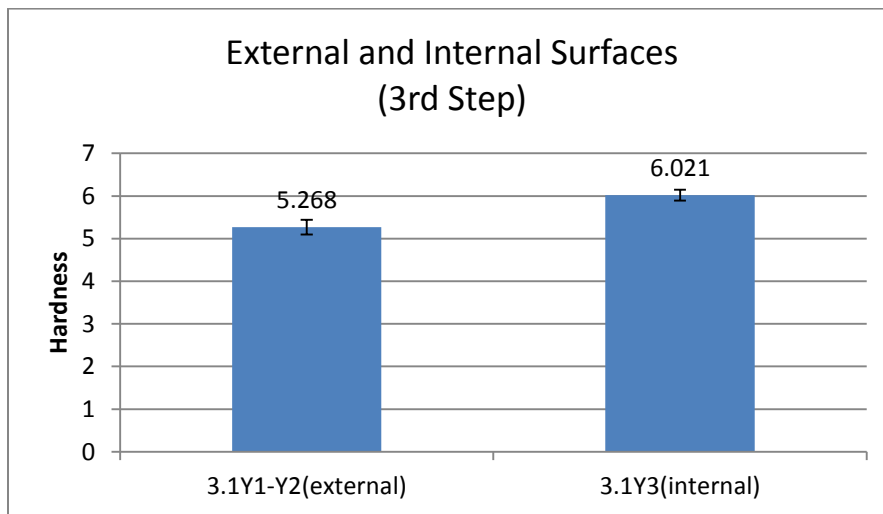


Figure 4.26: Comparison between hardness of external and internal surface

4.2.4 Y plane: Build Height Effect

Top surfaces of the 3 major steps have been compared for mechanical properties too. Figure 4.27 represents the Young's modulus and figure 4.28 represents the hardness values for 3 samples taken from 3 different heights. 3rd step sample has the highest Young's modulus and

hardness and 1st step has the lowest. Since 3rd step is closest to substrate, the resulting higher cooling rate causes finer dendritic structure and higher mechanical properties. From the optical images for microstructure shown in figure 4.4, the 2nd step sample has larger amount of dark bands on the borders of melt pool which causes lower Young's modulus and hardness.

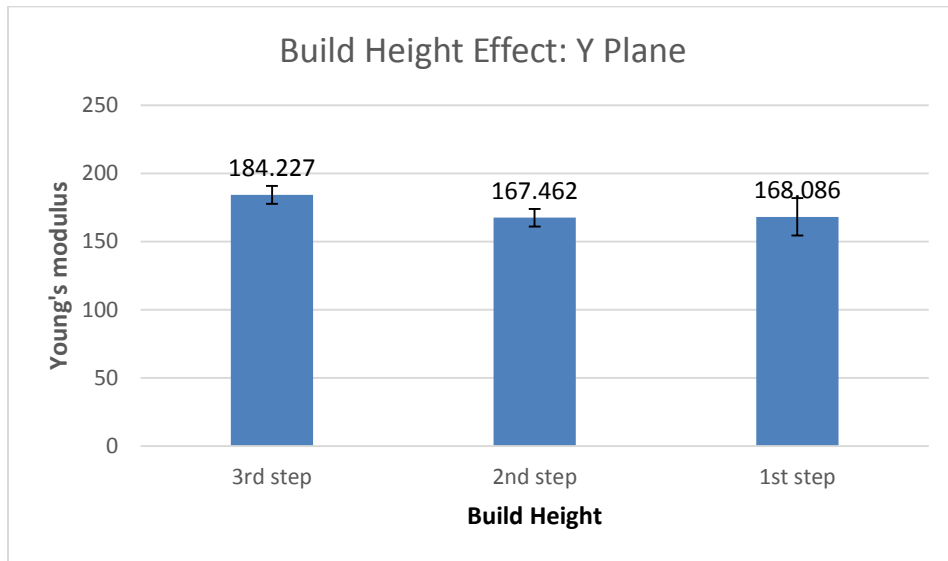


Figure 4.27: Comparison between Young's moduli of different build heights

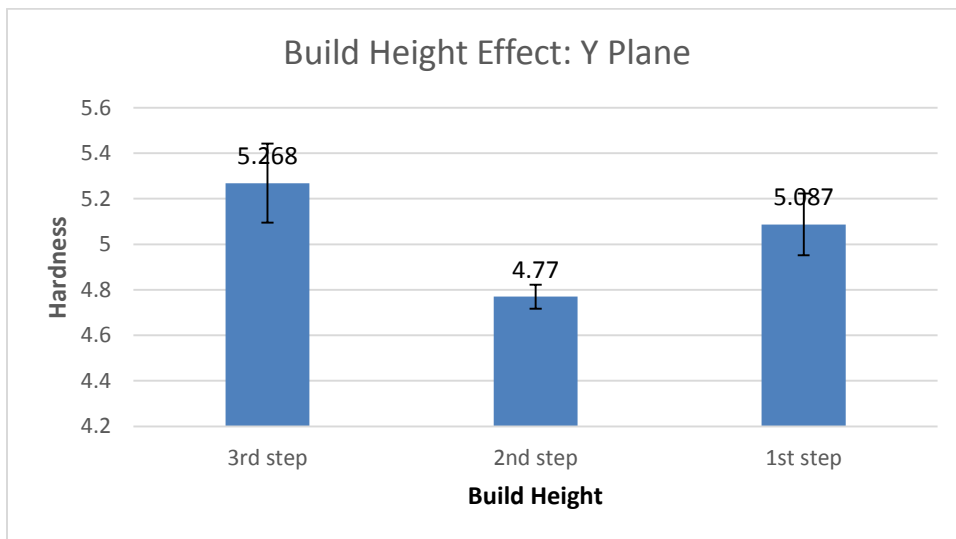


Figure 4.28: Comparison between hardness of different build heights

4.2.5: Y plane: Bottom Surfaces

The bottom surfaces under each step go through different thermal history. The surface under 3rd step was subjected to lowest number of thermal cycles since the height of that step is lowest. On the other hand, the step under the 1st and 2nd step has been through more thermal cycles. A comparison of mechanical properties between these bottom surfaces is illustrated in figures 4.29 and 4.30. All the surfaces have fairly high Young's modulus (over 180 GPa) and hardness (over 5 GPa) compared to other locations of the part since all of these were close to the substrate, therefore had higher cooling rate and finer grain size. Clearly, the surface under 2nd step has lowest Young's modulus which is expected due to the fact that it is subjected to continuous re-melting. The surfaces under 3rd and 1st step are closer to the un-melted powder, so those had even higher cooling rate than the surface under 2nd step. The hardness values do not necessarily agree with Young's modulus values. However, it is not expected, but not uncommon that sometimes these follow different trend. Hardness is a measure of a material's relative resistance to deform due to a force applied by a harder material whereas Young's modulus depicts a material's resistance to elastic deformation for per unit pressure applied. Though the surface under the 1st step showed highest hardness, the surface under the 3rd step had the lowest.

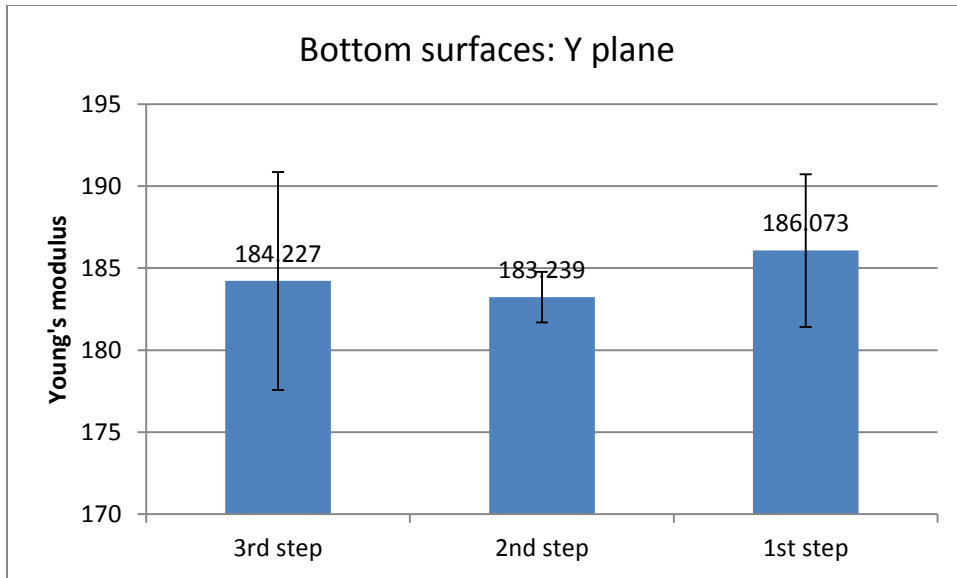


Figure 4.29: Comparison between Young's moduli of bottom surfaces

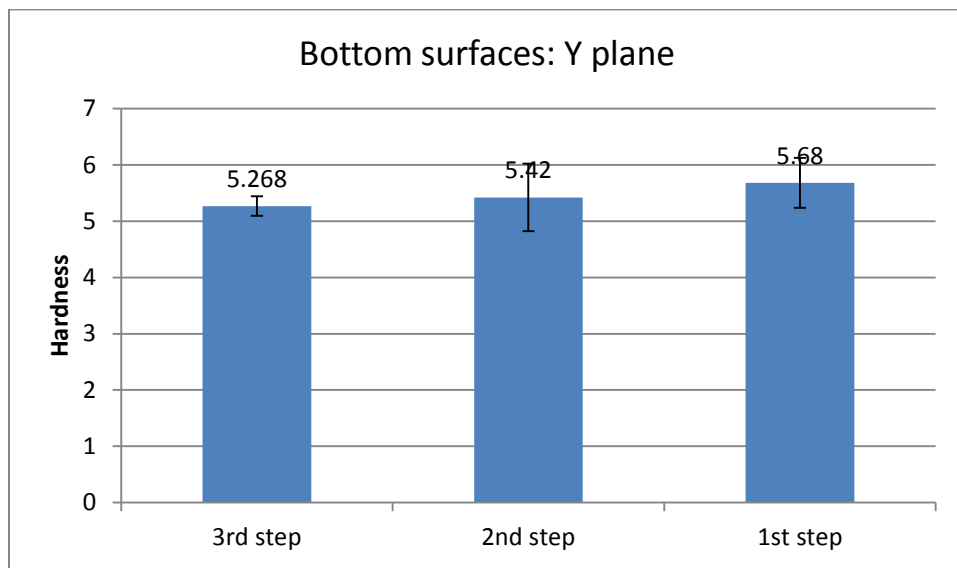


Figure 4.30: Comparison between hardness of bottom surfaces

4.2.6 Z plane: Effect of Thermal Cycles

All the Z plane samples were tested using Agilent technologies nanoindenter G 200, so the results are not comparable to those obtained for Y plane that used Hysitron Triboindenter. Figure 4.31 and 4.32 show effect of number of thermal cycles on Young's modulus and hardness for Z plane. 2.2ZZ2 has highest Young's modulus and hardness which is located closest to the

relatively cooler substrate and had higher cooling rate. On the other hand, 1.0Z1 has lowest Young's modulus and hardness. Even though the range of the values is quite different from Y plane values, but these follow the same trend on both of the planes.

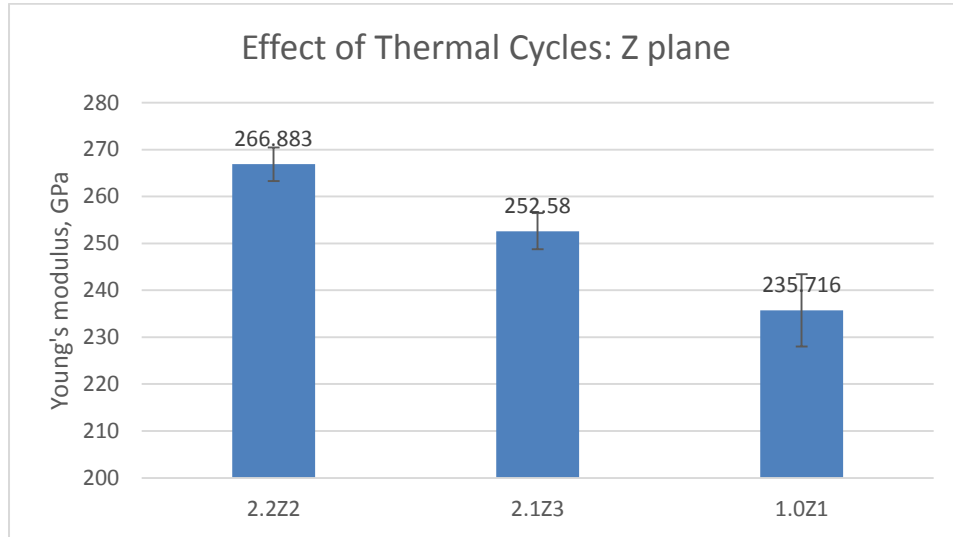


Figure 4.31: Effect of thermal cycle on Young's modulus of Z plane

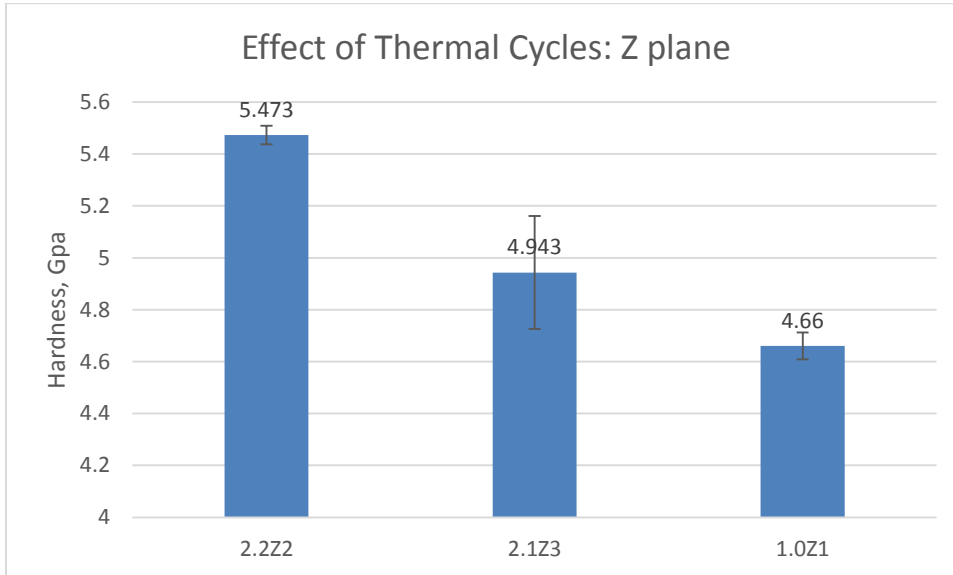


Figure 4.32: Effect of thermal cycles on hardness of Z plane

4.2.7 Z plane: External and Internal surface

The comparison between mechanical properties of internal and external surfaces for Z plane is showed in figure 4.33 and 4.34. The data is taken on 2nd step. As can be seen from the images, the internal surface has higher mechanical properties than the external one which is valid for Y plane too.

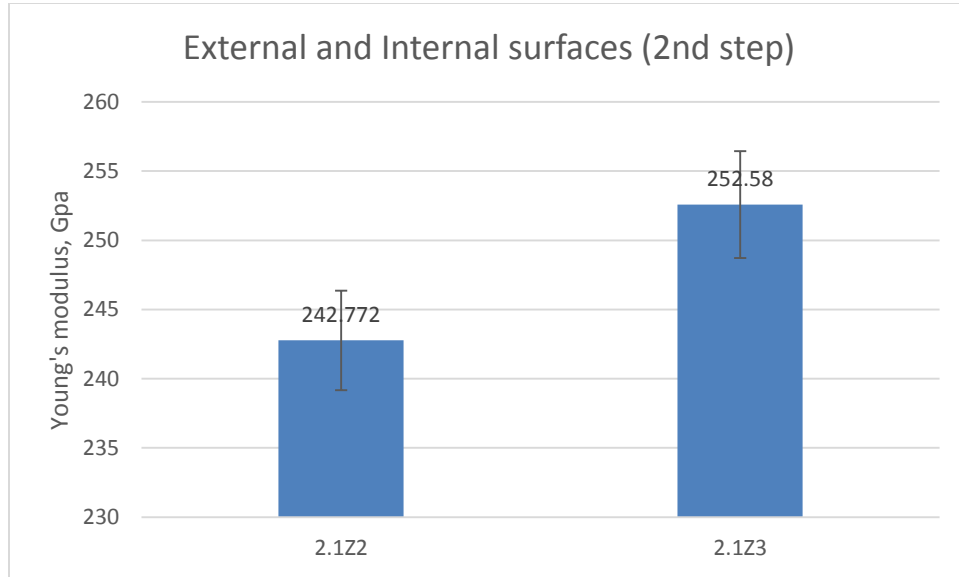


Figure 4.33: Comparison between Young's modulus of external and internal surfaces

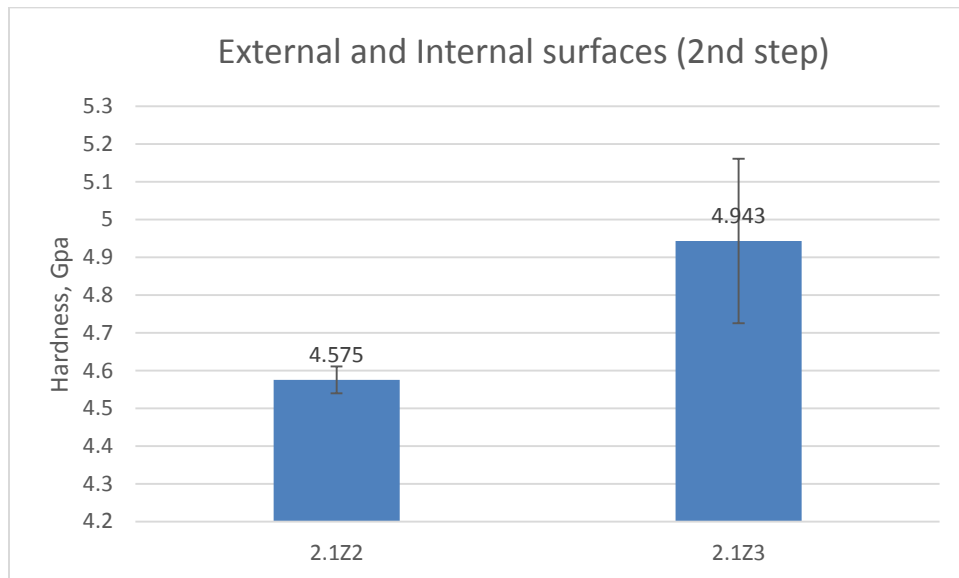


Figure 4.34: Comparison between hardness of external and internal surfaces

For 3rd step, the trend is different as we have also seen for Y plane. It can be caused by the higher cooling rate in the external surface since it is exposed to unmelted powder. Higher cooling rate causes finer grain size, thus higher mechanical properties.

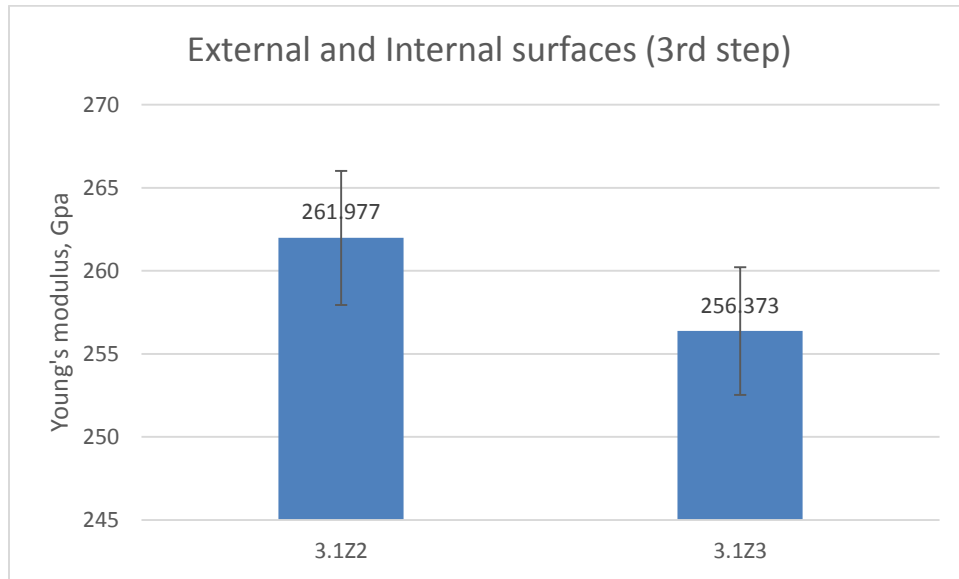


Figure 4.35: Comparison between Young's modulus of external and internal surfaces

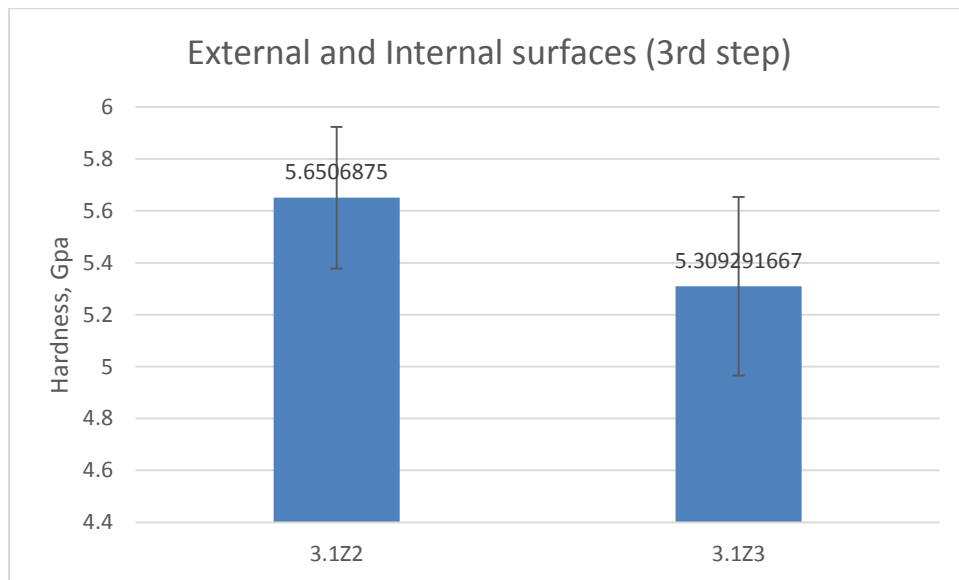


Figure 4.36: Comparison between hardness of external and internal surfaces

4.2.8 Z plane: Build Height Effect

On the Z plane, Young's modulus on top surfaces showed a different trend that can be seen on Y plane. As showed in figure 4.37, the Young's modulus is highest on 3rd step which is same for hardness too. On Y plane also, 3rd step had highest mechanical properties which is explainable. But the 1st step of Z plane has lowest Young's modulus which is not the same case for hardness and Y plane values. Since the tip is much finer in these cases, there is always a chance of indenting on a single phase which may not refer to the entire material itself.

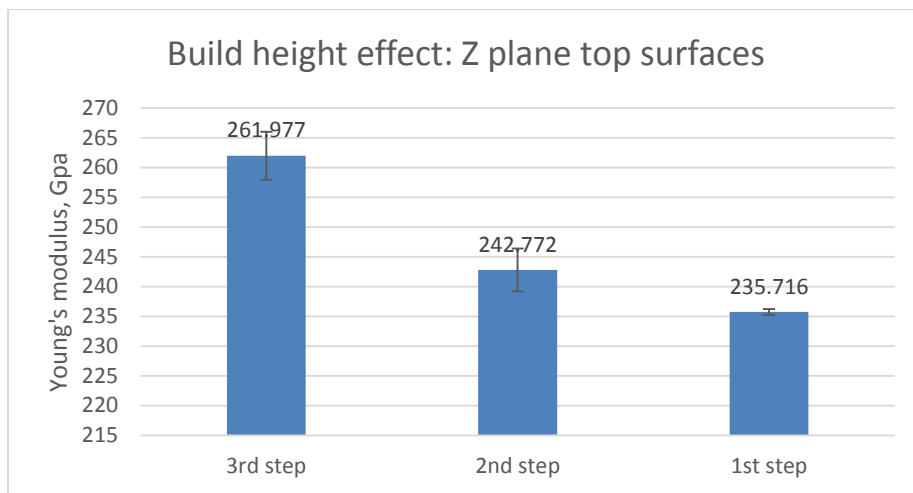


Figure 4.37: Comparison between Young's modulus of top surfaces

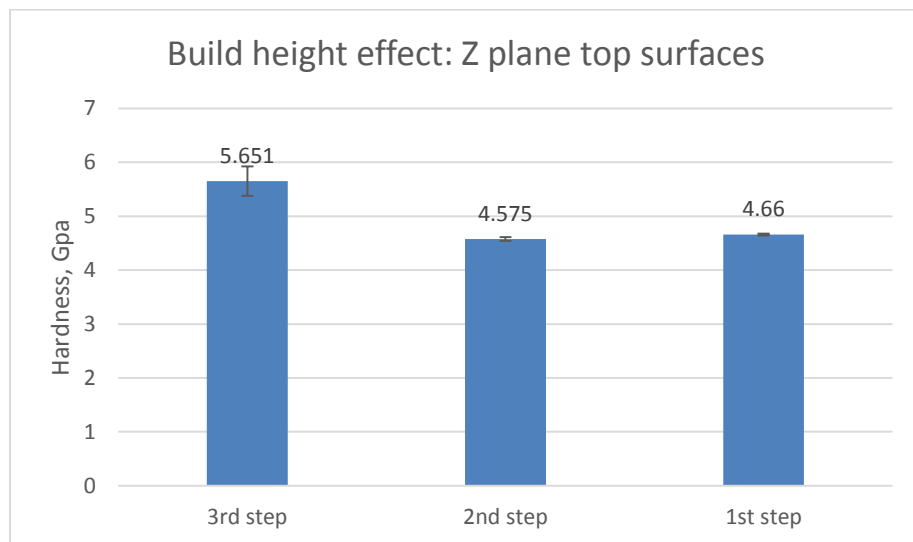


Figure 4.38: Comparison between hardness of top surfaces

4.2.9 Z plane: Bottom surfaces

The Z plane surface under than 1st step has the highest Young's modulus as illustrated in figure 4.39. Same trend was observed on Y plane too as long as the Young's modulus is concerned. However, even though the hardness under 2nd step is lowest, the highest is observed under 3rd step unlike Young's modulus. Also, the trend is different compared to Y plane results.

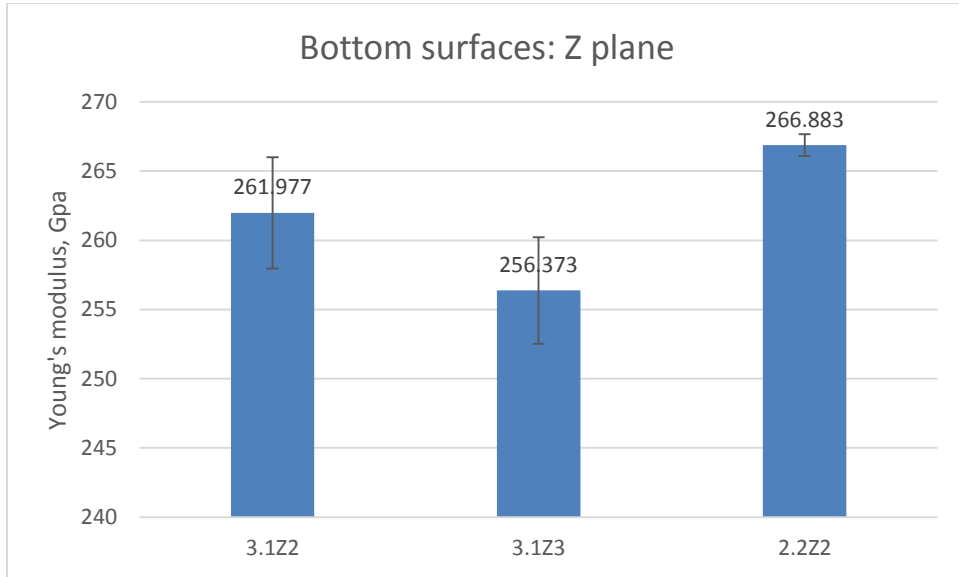


Figure 4.39: Comparison between Young's modulus of bottom surfaces

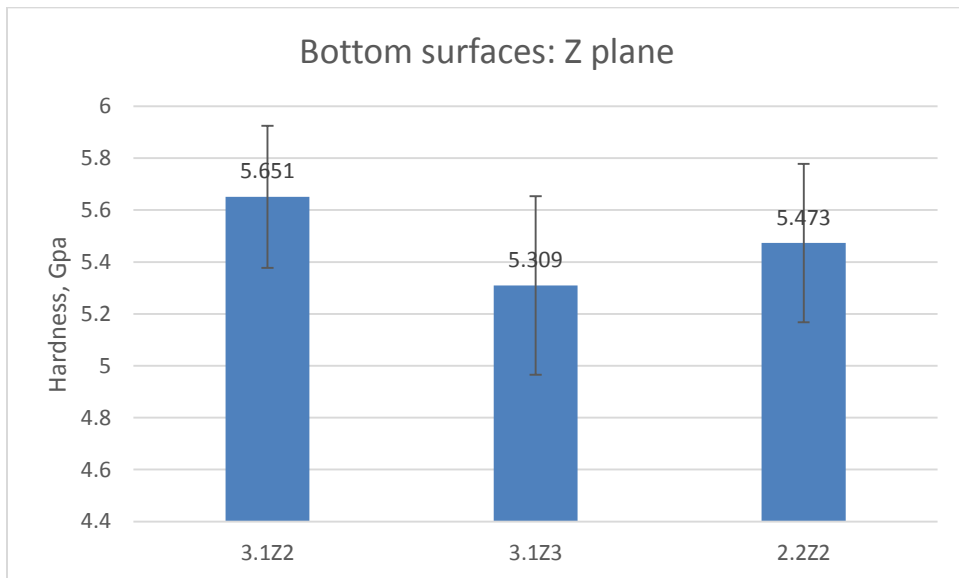


Figure 4.40: Comparison between hardness of bottom surfaces

4.3 Finite Element Analysis of Nanoindentation

The main objective of FEM analysis of nanoindentation is to compare the results with experimental results and then obtain plastic properties namely strain hardening exponent and yield strength. After validating the model by replicating literature results (discussed in section 3.5), simulations were run for different values of yield strength, plastic strain and strain hardening component. The yield strength was kept at mainly around 1100 MPa as found in literature for traditionally manufactured Inconel 718, but for the sake of study, simulations were run for 860-1300 MPa. The value of strain hardening exponent was taken as 0.08 and results are shown in figure 4.41 for two different range of plastic strain. It has been observed that these values do not give the expected force which is 5000 μN . Also, it is pretty obvious from the figure that range of plastic strain also does not affect results at all.

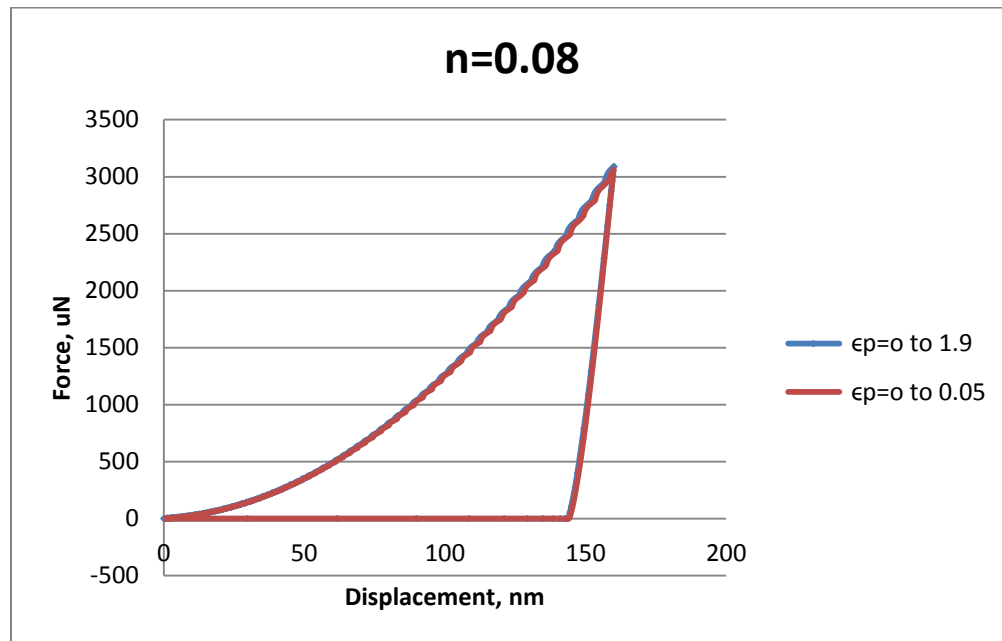


Figure 4.41: 2D simulation results for $n=0.08$

FEM analyses were performed by varying several inputs like tip radius, meshing, yield strength, plastic strain and so on even to an unreal extent. Tip radius or meshing do not seem to

have noticeable effect on result. Finer meshing lengthens the run time, but does not contribute to change in the value of force. Increase in yield strength definitely increases the force, but not over 3500 μN for 1300 MPa which is fairly high yield strength. Also change in a variable to an unreal extent causes termination of the simulation without completion. The most significant change was observed by varying strain hardening exponent, n . For the sake of study, the value of n was taken as 0.5 which literally produces identical results as found in experiment as shown in figure 4.42. Change in none of the other variables gives results close to experiment. The experiments were run on a sample located near the top of an SLM processed Inconel 718 part. More on the experiments can be found in reference [5]. The value of Young's modulus was taken as 200 GPa as found for this particular nanoindentation test. The highest displacement considered here was 160 nm which was caused by 5144 μN force that overshoot the experimental force by a slight margin. During the experiment, 5000 μN force caused 159.89 nm displacement. Since the simulation was more like a reverse procedure of the experiment due to the fact that displacement was given as an input for the calculation, slight difference in result is expected.

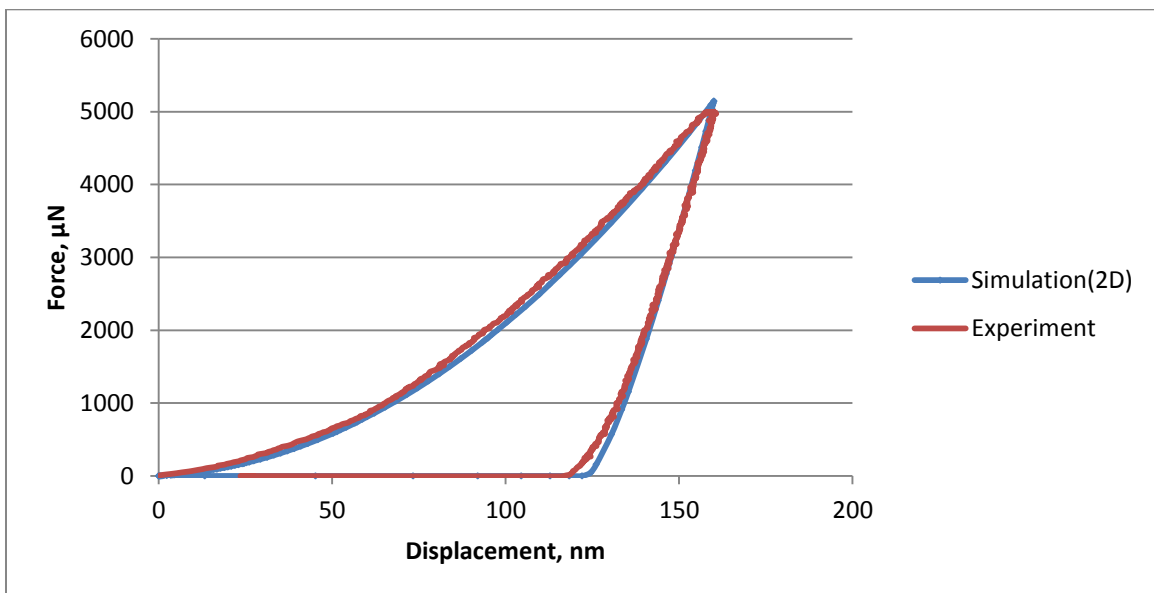


Figure 4.42: FEM results and experimental results found for SLM Inconel718 [5]

Results vary depending on the location of the sample as well since Young's modulus, thus displacement also changes. On the basis of figure 4.42, the value of yield strength is 1300 MPa and strain hardening exponent is 0.5. The value of yield strength is still reasonable, but in most of the studies carried out for traditionally manufactured Inconel 718 suggest the value of strain hardening exponent to be around 0.08. Recommendations to improve the results are discussed in chapter 5.

CHAPTER 5: CONCLUSIONS AND RECOMMENDATIONS

5.1 Conclusions

This research work mainly focuses on the SLM fabricated Inconel 718 part which has staircase feature and due to this feature, difference in microstructure and mechanical characteristics is expected. To compare between locations, four groups were considered to get a better understanding. Even though the microstructure did not reveal a lot of difference, mechanical properties showed some trends for specific groups of locations.

5.1.1 Microstructure: Y plane

The microstructure of Y plane was revealed by etching the surface and observed using OM. Few surfaces from X plane have also been taken to compare with Y plane. The observations can be summarized as follows:

1. The microstructure on Y plane consists of columns of melt pool cut sections. These cut sections are represented by arcs with dark bands defining their borders. The columnar grains growing towards build directions is induced by the direction of heat flux from top layers to bottom layers. The dark band indicates intermetallic phase which makes material mechanically weaker.
2. The arcs on Y plane have different depth and width. The arcs of deeper and wider melt pool indicate the edges of laser melted tracks known as ‘keyhole’ whereas the shallower arcs indicate the cut sections of somewhere in the middle of melted tracks.
3. The amount of dark intermetallic phase appears to be higher in the middle of the part compared to top and bottom at the same horizontal distance.

4. The arcs look slightly shallower close to the external surface which is at the top of a step than the internal surface which is inside the part at the same height. The internal surface has deeper arcs since the layers are subjected to repeated melting.
5. The locations close to the top of each step seem to be more or less similar. All the top surfaces are exposed to un-melted powder, but the bottom step is also closer to the solid substrate, that can cause the arcs to be slightly shallower there.
6. The bottom surfaces at the same height also do not show significant difference. The one under 3rd step has more defined microstructure due to the fact that it is close to top and bottom surface, so had highest cooling rate than the surfaces under 2nd or 1st step.
7. Microstructure on X plane appears to be similar to Y plane.

5.1.2 Microstructure: Z plane

The top surface was studied the same way. But SEM images have also been included to take a closer look at the microstructure. The important findings are:

1. The microstructure of Z plane consists of laser melted tracks. It resembles the scanning pattern too. The average width of the melted tracks is ~ 100-150 μm .
2. The surfaces under same step from top to bottom do not show any noticeable difference. The top surface looks different than the surfaces inside which is observed and discussed in another comparison group.
3. As mentioned earlier, the surface on top of the surface has different microstructure than the inside a step at same height. The external surface is more defined and free of any incomplete track or interference of any other layer on top of it since there is no more remelting unlike the surface inside a step. The inner surface reveals a shift of ~ 1.15 mm of the laser beam.

4. OM images of top surfaces on each step are similar since all of these are exposed to relatedly cooler un-melted powder layers, but SEM images show difference between 3rd step and other two steps. 3rd step is not only exposed to powder layers, but also close to substrate, so the boundary of each melted track is not as clear as it is on 2nd and 1st step. In other words, the white phase which can be δ precipitate is not present in between two tracks on 3rd step which can be clearly observed on 2nd and 1st step.
5. Bottom surfaces of part on Z plane are not much different too. Only the surface on 3rd step is different due to the fact that it is on the top of a step.

5.1.3 Mechanical Properties

Mechanical properties were measured using nanoindentation techniques and compared in same groups. The findings for both of the planes are listed below:

1. For both Y and Z plane, the Young's modulus and hardness decreases as it goes from top to bottom.
2. For 2nd step on both planes, the inner surfaces have higher mechanical properties whereas the trend is opposite for 3rd step.
3. On Y plane, the Young's modulus and hardness are lowest on 2nd step and highest on 3rd step. On the other hand, on Z plane, even though hardness follows the same trend as Y plane, Young's modulus appeared to decrease from bottom to top.
4. Among the bottom surfaces, the surface under 1st step has highest Young's modulus and the surface under 2nd step has the lowest. As long as the hardness goes, it increases from left to right on Y plane whereas on Z plane, the surface under 3rd step has highest value and the surface under 2nd step has the lowest.

5.2 Contribution of the Study

With the increasing demand of and expectations from additively manufactured parts in various industries that deal with sophisticated and intricate design, it has become very crucial to do extensive research from different aspects including part geometry keeping the way of manufacturing in mind. The contribution of this study towards research AM technology can be summarized as follows:

- Numerous research works have been performed on process parameters, effect of heat treatment, microstructure and properties of different AM processed parts. But since SLM is a layer-by-layer building process, build height plays an important role in determining microstructure and mechanical properties unlike traditional manufacturing processes. This research reveals important information about build height effect.
- Part geometry also can make a specific part different from the other in terms of structure and property. Previously, build height effect on SLM processed Inconel 718 part has been studied [5] and the part was rectangular. Only build height was considered in that research since the part is uniform along the height and width. But when staircase comes into play, number of layers increases from left to right.
- Four different groups were considered in this research to compare microstructure and mechanical properties. The study reveals that there is significant difference in mechanical properties along the build height. So, difference in microstructure is expected if observed in higher magnification and using EBSD or XRD technology. OM and SEM images revealed difference between microstructure on external and internal surfaces of a stair at the same height. Mechanical properties were also proven to be different, but the trend will be clearer if number of samples and tests are increased.

- This research also shows the possible ways to proceed further to reach a reasonable conclusion which will contribute a lot to improve design considerations while producing a part.

So, an approach has been made through this research to reveal effect of build height on a part having specific feature and it can be claimed that staircase makes a part different from parts with other geometry in terms of microstructure and mechanical properties. Further recommendations and possible improvements are suggested in next section.

5.3 Recommendations and Future Work

The study on SLM processed Inconel 718 part with staircase feature revealed quite a lot of information, but improvements and additions can be made in this topic. Some possibilities are discussed below:

5.3.1 Microstructure

Possible improvements for microstructure study are suggested below:

1. Even though sufficient amount of samples were prepared for Y plane, number of samples in Z plane was less than that of Y plane due to time constraint. The number of samples was still enough for required comparisons, but more samples could be made from more locations to have better observations and more data.
2. Two etching solutions were tried for different amounts of time. More recommendations can be found in literatures to try and get improved result.
3. OM and SEM is used to study microstructure. Further research like EBSD, XRD analysis can be done to detect composition and phases in certain locations. That will provide better explanations for mechanical properties too.

5.3.2 Mechanical Properties

There were some limitations in the study of mechanical properties which caused some confusions in the results. Ways to eliminate them are discussed below:

1. Major drawback in nanoindentation was using two different nanoindenters due to unavoidable circumstances. Same equipment will provide a space for comparing values between Y and Z plane which could not be done in this research.
2. More data can be collected from each sample to study mechanical properties. Since the tips used in both equipment are so fine (100 nm and 20 nm diameter), it can create indent on a specific phase which can be misleading to consider it as the entire material's property. Also microindentations can be done to obtain hardness for the same reason.

5.3.3 FEM Analysis

In FEM analysis of nanoindentation, distance was given as input while defining boundary conditions, but the force cannot be given. In Triboindenter, the force is given as input. So, one of the challenges in the FEM analysis was to obtain the same amount of force as given for experiment. In Nanoindenter G 200, distance can be provided as input. FEM analysis can be performed based on the experiments done on Nanoindenter G 200 where distance is given. That will be more straight forward and effective way of comparing FEM results with experimental results. Also, values can be different for different nanoindenters, so that also should be kept in mind while doing FEM analysis.

REFERENCES

1. Gong, H., Gu, H., Zeng, K., Dilip, J., Pal, D., Stucker, B., Christiansen, D., Beuth, J., Lewandowski, J., *Melt Pool Characterization for Selective Laser Melting of Ti-6Al-4V Pre-alloyed Powder*
2. Gong, X., Wang, X., Cole, V., Jones, Z., Cooper, K., and Chou, K., *Characterization of Microstructure and Mechanical Property of Inconel 718 From Selective Laser Melting*, Proc. ASME 2015 International Manufacturing Science and Engineering Conference, American Society of Mechanical Engineers, pp. V001T002A061-V001T002A061.
3. Thijs, L., Verhaeghe, F., Craeghs, T., Humbeeck, J. V., Kruth, J. P., *A study of the microstructural evolution during selective laser melting of Ti-6Al-4V*, Acta Materialia, Volume 58, Issue 9, May 2010, Pages 3303–3312
4. Popovich, V.A., Borisov, E.V., Popovich, A.A. , Sufiiarov, V.S. , Masaylo, D.V., Alzina, L., *Functionally graded Inconel 718 processed by additivemanufacturing: Crystallographic texture, anisotropy of microstructure and mechanical properties*, Materials & Design, Volume 114, 15 January 2017, Pages 441–449
5. Wang, X., Keya, T., Chou, K., *Build Height Effect on the Inconel 718 Parts Fabricated by Selective Laser Melting*, Procedia Manufacturing, Volume 5, 2016, Pages 1006–1017
6. Gibson, I., Rosen, D., *Additive Manufacturing Technologies: 3D Printing, Rapid Prototyping, Direct Digital Manufacturing*, 2nd edition
7. "A third industrial revolution". The Economist. 2012-04-21. Retrieved 2016-01-04.
8. <http://3dprintingforbeginners.com/an-introduction-to-3d-printing-services/>
9. Williams JD, Deckard CR (1998) *Advances in modeling the effects of selected parameters on the PLS process*. Rapid Prototyp J 4(2):90–100
10. Jia, Q., Gu, D., *Selective laser melting additive manufacturing of Inconel 718 superalloy parts: Densification, microstructure and properties*, Journal of Alloys and Compounds, Volume 585, 5 February 2014, Pages 713–721
11. http://www.nickel-alloys.net/nickel_and_nickel_alloys.html
12. ASM Specialty Handbook: Nickel, Cobalt, and Their Alloys

13. www.specialmetals.com
14. Zhang, D., Niu, W., Cao, X., Liu, Z., *Effect of standard heat treatment on the microstructure and mechanical properties of selective laser melting manufactured Inconel 718 superalloy*, Materials Science and Engineering:A, Volume 644, 17 September 2015, Pages 32–40
15. <http://www.conceptlaserinc.com/machines/m2-cusing/>
16. <http://www.smathaudhu.com/equipment.php>
17. Hussain, A., Hao, L., Yan, C., Everson, R., Young, P., *Advanced lattice support structures for metal additive manufacturing*, Journal of Materials Processing Technology 213 (2013) 1019–1026
18. Strano, G., Hao, L., Everson, R. M., Evans, K. E., *A new approach to the design and optimisation of support structures in additive manufacturing*, Int J Adv Manuf Technol (2013) 66:1247–1254
19. Cloots, M., Spierings, A. B., Wegener, K., *Assessing new support minimizing strategies for the additive manufacturing technology SLM*, International Solid Freeform Fabrication symposium An Additive Manufacturing Conference, Austin, August 12-14, 2013. The University of Texas.
20. Cheng, B., Chou, K., *Geometric consideration of support structures in part overhang fabrications by electron beam additive manufacturing*, Computer-Aided Design, Volume 69, December 2015, Pages 102–111
21. Antunes, J M, Fernandes, J. V., Menezes, L. F., Chaparro, B M, *A new approach for reverse analyses in depth-sensing indentation using numerical simulation*, Acta Materialia, 55(1), pp. 69-81
22. Ogasawara, Nagahisha, Chiba, Norimasa, Chen Xi, *Measuring the plastic properties of bulk materials by single indentation test*, Scripta Materialia, 54(1), pp. 65-70
23. Fang, Jie, Yuan, Huang, *The local concept to assess weldment with help of nano-indentation and FEM simulation*, 13th International Conference on Fracture, 2013
24. N. Yu, A.A. Polycarpou, and T.F. Conry, *Tip-radius effect in finite element modeling of sub-50 nm shallow nanoindentation*. Thin Solid Films, 2004. 450(2): p. 295.
25. Cao, Yamping, Huber, Norbert, *Further Investigation on the definition of the representative strain in conical indentation*, Journal of Materials Research 06/2006; 21(07):1810 – 1821
26. Phani, K., Niyogi, S., *Young's modulus of porous brittle solids*, J. Mater. Sci., 22 (1987), pp. 257–263

27. <https://en.wikipedia.org/wiki/Inconel>
28. Baufeld, B., Van der Biest, O., Gault, R., *Additive manufacturing of Ti–6Al–4V components by shaped metal deposition: Microstructure and mechanical properties*, Materials & Design, Volume 31, Supplement 1, June 2010, Pages S106–S111
29. Facchini, L., Magalini, E., Robotti, P., Molinari, A., *Microstructure and mechanical properties of Ti-6Al-4V produced by electron beam melting of pre-alloyed powders*, Rapid Prototyping Journal, Vol. 15 Issue: 3, pp.171-178 (2009)
30. Amato, K. N., Gaytan, S. M., Murr, L. E., Martinez, E., Shindo, P. W., Hernandez, J., Collins, S., Medina, F., *Microstructures and mechanical behavior of Inconel 718 fabricated by selective laser melting*, Acta Materialia, Volume 60, Issue 5, March 2012, Pages 2229–2239
31. Zhang, D., Niu, W., Cao, X., Liu, Z., *Effect of standard heat treatment on the microstructure and mechanical properties of selective laser melting manufactured Inconel 718 superalloy*, Materials Science and Engineering: A, Volume 644, 17 September 2015, Pages 32–40
32. Wang, Z., Guana, K., Gao, M., Li, M., Chen, X., Zeng, X., *The microstructure and mechanical properties of deposited-IN718 by selective laser melting*, Journal of Alloys and Compounds, Volume 513, 5 February 2012, Pages 518–523
33. Chlebus, E., Gruber, K., Kuźnicka, B., Kurzac, J., Kurzynowski, T., *Effect of heat treatment on the microstructure and mechanical properties of Inconel 718 processed by selective laser melting*, Materials Science and Engineering: A, Volume 639, 15 July 2015, Pages 647–655